Doctoral Thesis

Chemical Vapor Deposition of High Quality Graphene Films On Cu/Ni(111) Alloy Foils

Ming Huang

Department of Materials Science and Engineering

Graduate School of UNIST

2018

Chemical Vapor Deposition of High Quality Graphene Films On Cu/Ni(111) Alloy Foils

Ming Huang

Department of Materials Science and Engineering

Graduate School of UNIST

Chemical Vapor Deposition of High Quality Graphene Films On Cu/Ni(111) Alloy Foils

A thesis/dissertation
submitted to the Graduate School of UNIST
in partial fulfillment of the
requirements for the degree of
Doctor of Philosophy

Ming Huang

06/12/2018 of submission

Approved by

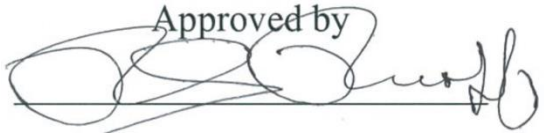

Advisor
Rodney S. Ruoff

Chemical Vapor Deposition of High Quality Graphene Films On Cu/Ni(111) Alloy Foils

Ming Huang

This certifies that the thesis/dissertation of Ming Huang is approved.

06/12/2018 of submission

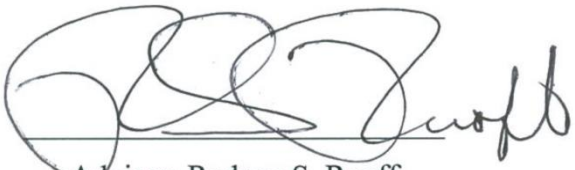

Advisor: Rodney S. Ruoff

Jong-Beom Baek: Thesis Committee Member #1

Zonghoon Lee: Thesis Committee Member #2

Hyung-Joon Shin: Thesis Committee Member #3

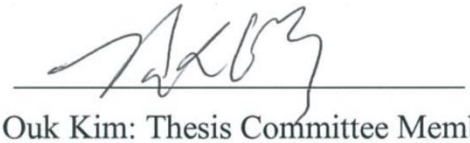

Sang Ouk Kim: Thesis Committee Member #4;

Abstract

Graphene, a monolayer of sp^2-bonded carbon atoms or one monolayer of graphite, has attracted intense attention in recent times due to its fascinating properties, such as excellent carrier mobility, good thermal conductivity, high mechanical strength and high optical transmittance. To date, chemical vapor deposition (CVD) has been verified to be the most promising method to synthesize large area graphene with high quality and low cost. Despite the remarkably rapid progress that has been achieved in this field during the past 10 years, there are still many problems or issues related to the fast growth of large area single-crystalline graphene and the controlled synthesis of bilayer and/or trilayer graphene that need to be addressed.

In this work, fast-growth of single crystal monolayer graphene by CVD has been achieved on 'home-made' single crystal Cu/Ni(111) alloy foils over large area. Full coverage was achieved in 5 min or less for a particular range of composition (1.3 at.% to 8.6 at.% Ni), as compared to 60 min for a pure Cu(111) foil under identical growth conditions. These are the bulk atomic percentages of Ni, as a superstructure at the surface of these foils with stoichiometry Cu6Ni1 (for 1.3 to 7.8 bulk at.% Ni in the Cu/Ni(111) foil) was discovered by low energy electron diffraction (LEED). Complete large area monolayer graphene films so obtained, are either single crystal or close to single crystal, and include folded regions that are essentially parallel with each other and could originate from wrinkles that 'fell over' to bind to the surface; these folds are separated by large, wrinkle free regions. The folds occur due to the buildup of interfacial compressive stress (and its release) during cooling of the foils from 1075 ℃ to room temperature. Joining of well-aligned graphene islands (obtained by arresting the growth prior to full film coverage) was investigated with high magnification SEM and aberration-corrected high-resolution TEM as well as AFM, STM, and optical microscopy. Results show that many of the 'junction regions' have folds and these arise from interfacial adhesion mechanics (the folds may originate from the buildup of compressive stress during cool-down, but these folds are different than those observed on the continuous graphene films—these folds in the joined islands occur due to 'weak links' in terms of the interface mechanics).

In addition, we have synthesized very large-area, high quality bilayer and tri-layer graphene films by chemical vapor deposition; these films are almost entirely 'AB-stacked'. The number of layers of the graphene films was controlled by finely tuning the Ni concentration in the alloy foil. As a result, 95% area coverage of bilayer that is essentially 100% AB-stacked was achieved for samples of size 1.0 cm × 1.5 cm; and 60% area coverage of trilayer that is essentially 100% 'ABA-stacked' over the same sample size. We have studied the stacking sequence of the as-prepared bilayer and multilayer graphene. Time-of-flight secondary ion mass spectrometry mapping, hydrogen etching with *in situ* scanning electron microscopy, and cross-sectional high-resolution transmission electron microscopy imaging show that the second-layer (the 'adlayer'; and thus, also the 3rd layer and so on) grows underneath the first layer, forming an 'inverted wedding cake' structure.

Our work demonstrates that single crystal Cu/Ni(111) alloy foils can be made and used to prepare large-scale single crystal monolayer graphene and AB-stacked layer-tunable graphene films where all (or almost all) the AB-stacked regions have the same (single) crystal orientation. Graphene quality has been demonstrated through a combination of characterization methods and and graphene growth mechanism is discussed.

Keywords: Graphene, Chemical vapor deposition, Cu/Ni(111), Single crystal, Fold, Bilayer, AB-stacked, Layer-tunable, Growth mechanism

Contents

List of figures

Figure 3.10. Effect of Ni concentration on the nucleation density and island size of the as-grown graphene. (a) SEM images of graphene islands on pure Cu(111). (b–f) SEM images of graphene islands grown on Cu/Ni(111) alloy foils with (b) 1.3 at.%, (c) 2.4 at.%, (d) 4.3 at.%, (e) 5.9 at.%, and (f) 8.6 at.% Ni at 1075 ℃. (g) Dependence of the nucleation density on Ni concentration. (h) Dependence of the graphene island size on Ni concentration.

Figure 3.11. Arrhenius plot of island size as a function of inverse temperature for graphene growth on Cu(111) and Cu/Ni(111) (5.9 at.% Ni). Here, 5 sccm of 1% CH_4 (diluted in Ar) was used at different temperatures (1075, 1050, 1025, 1000, 970, and 950 ℃) for graphene growth.

Figure 3.12. Dehydrogenation of a methane molecule on Cu(111) and Cu/Ni(111) surfaces and the associated transition states. Inset shows the transition states of CH_x radicals on the Cu/Ni(111) surface and the removal of H from the surface in the form of an H_2 molecule.

Figure 3.13. Raman mapping of $^{13}C/^{12}C$ labeled graphene (transferred onto 300-nm SiO_2-on-Si substrates) grown on Cu(111) and Cu/Ni(111) foil (5.9 at.% bulk Ni). (a, b) Raman maps of the 2D peak of transferred isotope-labeled graphene grown on Cu(111) foil. (c-f) Raman maps of the 2D peak of transferred isotope-labeled graphene grown on Cu/Ni(111) alloy foil. The color indicates the peak position of the 2D peaks, where purple (2580 cm^{-1}) represents pure ^{13}C- and red (2680 cm^{-1}) represents (almost) pure ^{12}C-labeled graphene.

Figure 3.14. Raman characterization/mapping of the graphene. Raman maps of the I_D/I_G peak height ratio and 2D FWHM of (a and b), hexagonal islands, (d and e) joined islands, and (g and h) a continuous monolayer graphene film. (c, f, i) Raman spectra randomly taken from ~100 locations on the islands and continuous film shown.

Figure 3.15. Raman line spectra collected at the merged regions of different graphene islands. (a-d) Optical images at different merged regions. (e-l) Corresponding Raman line spectra taken at different merged regions of the islands.

Figure 3.16. Characterization of hexagonal graphene islands and joined islands. Raman mapping of different regions shows the high quality of the graphene islands without any D peaks being observed.

Figure 3.17. Evaluating the uniformity of the monolayer graphene film over the whole region of the transferred sample (1 ×1 cm^2). Insets are the histograms of the 2D FWHM of the Raman 2D band.

directions (highlighted by the yellow dashed lines) on different Cu grains are observed (a), and are also observed in different regions on the same Cu grain (b). In addition, one can roughly obtain the grain size of the graphene by comparing the directions of the etching holes (as shown in the marked boxes in (b)).

Figure 3.25. Polarized optical microscopy (POM) imaging of the graphene using liquid-crystal material (5CB). (a) OM image of monolayer graphene islands grown on the Cu/Ni(111) alloy foil transferred onto 300-nm SiO_2-on-Si wafer. (b-f) POM images of the monolayer graphene islands after coating with 4-pentyl-4-cyanobiphenyl (5CB; Sigma Aldrich) liquid crystals. (g) OM image of a continuous monolayer graphene film prepared on the Cu/Ni(111) alloy foil and transferred onto a 300-nm SiO_2-on-Si wafer. (h) POM image of the continuous monolayer graphene in (g). (i) POM image of a monolayer graphene film prepared from a commercial poly-crystalline Cu/Ni alloy.

Figure 3.26. Measurement of electrical transport of the monolayer graphene film grown on Cu/Ni(111) foil. (a) An optical microscopy image of the fabricated device on a 300-nm thick SiO_2/Si substrate. (b) Typical gate-dependent conductance of the device measured at room temperature. The inset shows the linear and symmetric I_d-V_d curve, indicating a good ohmic contact between the Cr/Au contact and the graphene channels.

Figure 3.27. Properties of the monolayer graphene film. (a) Optical transmittance and (b) sheet resistance.

Figure 3.28. Characterization of the folding in continuous graphene film on Cu/Ni(111) foil. (a, b) SEM images of the fold regions in the continuous graphene. (c) AFM topographic image of a fold region. (d) Height profile along the white line indicated in (c). The height change along the white line in (c) is around 0.7 nm, which is consistent with the thickness of two layers graphene (thus, 3 layers of graphene with respect to the substrate—in short, due to a fold).

Figure 3.29. HR-TEM observation across the junction of two adjacent graphene grains show no rotation angle. (a) SEM image of joined islands with the same orientation on TEM grid. (b) TEM image of the area shown in (a). The numbers of the holes (in red) indicate the region where the SAED was obtained. (c) The dashed yellow line is the joined region of two adjacent islands, while the red line is that in which forty high-resolution TEM images were taken across the junction. (d) 6 selected images (frames 1, 5, 10, 20, 30, and 40) from the 40 continuous high-resolution TEM images. The identical orientation of all the FFTs and the absence of a distinct grain boundary in HR-TEM images, indicates the perfect stitching of the two islands with the same orientation. All the scale bars are 5 nm.

Figure 3.30. Analysis of atomic-resolution TEM images of joined graphene islands with a rotation angle between them. (a) SEM image of the two joined islands transferred onto a TEM grid. The highlighted box regions were further analyzed. The TEM images on the right indicate the corresponding area (located at the joined region) under TEM. (b-d) Corresponding TEM images of the regions shown in (a). The numbers indicate the regions for acquisition of SAED. (e) HR-TEM images of the graphene islands suspended over hole 1. Two grains (bottom left highlighted in yellow, top right highlighted in purple, respectively) are joined with a 23.5 °relative rotation. A line of 5-7 defects (pentagon-heptagon pairs) occurs along the boundary between the two grains (see (f) below). The scale bar is 2 nm. (f) Magnified HRTEM image of the high-angle tilted GB of graphene (enlargement of the area highlighted in red in (e)). The heptagons and pentagons are overlaid with green and yellow polygons, respectively. The GB has an array of 5-7 defects.

Figure 3.31. High-resolution TEM observations at the junction (joining region) of two graphene islands with the same orientation. (a) SEM image of the joining area of two graphene islands with the same orientation. (b) TEM image of the area shown in (a). The red line shows the outline (edges) of the two joined islands and the yellow line indicates the boundary. The blue circles and their numbers indicate the regions where SAED and HR-TEM was done. (c) DF-TEM images from hole 5, and hole 6, which are across the boundary between the two joined islands. The two on the right are the corresponding magnified images. The intensity profiles (inset) demonstrate the existence of overlapped bilayer and folded tri-layer. (d) HR-TEM image taken from hole 5 (joining region). “A” marked in the image represents the monolayer nature of the islands with the same orientation. The right-side images are the fast Fourier transforms (FFT) of the regions highlighted in the box region. All three FFTs show one set of hexagonal spots that are essentially identical. The regions highlighted in red and purple are both single-layer regions, while the green region showed A-B stacking (AB), indicating the overlapping of two aligned islands at the joining region. (e) HR-TEM image taken from hole 6 (joining region). The right side FFT images are taken from the region within the highlighted box. The regions marked in red and purple are the single-layer regions (one set of FFT, essentially identical) while the green region shows two sets of FFTs (with a rotation angle), indicating folding at the joining region.

Figure 3.32. SEM, TEM images and SAED patterns obtained at the merger of two islands with the same orientation. (a) SEM image of two joined graphene islands with the same orientation that had been transferred onto a TEM grid. (b, c) TEM images of the areas highlighted in (a). The red lines indicate the edges (outlines) of the two adjacent islands and the yellow line indicates the hypothetical boundary (junction). The numbers of the holes indicate the regions where SAED patterns were

acquired. (d) A series of SAED patterns taken from the grid holes highlighted in (b) and (c). All areas show the same orientation, indicating that the two joined islands have the same orientation.

Figure 3.33. Atomic-resolution TEM images of the region in the hole 5 where two islands overlap. (a) TEM image of two joined graphene islands. (b, c) HR-TEM images showing the tensile strain and shear strain in the overlap (bilayer) region. The purple and green dashed lines highlight the tensile strain and shear strain at the overlap region, respectively. The left bottom part in each of (b) and (c) is the single-layer region.

Figure 3.34. SEM images of the merging (joining) graphene islands. (a) Joining region shows folding. (b) Joining region shows no folding.

Figure 3.35. Scanning tunneling microscopy (STM) images at the joining region of two adjacent graphene islands (A and B). (a) Low-magnification STM image shows the corner of the joining region. The blue dashed line highlights the edges of the two adjacent graphene islands and the yellow arrow indicates the folding at the joining region. (b) Magnified image of the folding in image (a). (c) Height profile along the red line indicated in (b).

Figure 3.36. Folding in joined graphene islands on Cu/Ni(111) foil. (a) Schematic image of the fold region at the joining region of adjacent islands. (b) SEM image of the fold in the joining region. The yellow circle highlights the joining region. (c) AFM topographic image of the folding. (d) Height profile (white line) indicated in (c). The height is around 0.7 nm, which is consistent with a thickness of 2 layers of graphene (that is, 3 layers with respect to the substrate—a fold).

Figure 3.37. Carrier mobilities across the joining regions of two adjacent islands. (a, b) Optical microscopy image and intra-island and inter-island I_d-V_g curves for joined islands having a fold. (c, d) Optical microscopy image and intra-island and inter-island I_d-V_g curves for joined islands without a fold. (e) Summary of the device mobilities extracted from (b) and (d) for the joined islands with and without a fold.

Figure 3.38. Analyses of SEM and TEM images of the junctions between three graphene islands. (a) SEM image of three adjacent graphene islands. (b, c) HR-TEM image of regions 1 and 2 highlighted in (a). The number of layers in the monolayer region and the adjoining regions are highlighted in different colors. The 3L nature and the inset FFT patterns indicate the folding of both regions. 1L is the monolayer graphene region, 3L is the folded region and the 2L region (etched 3L region) is due to the e-beam irradiation (‘knock-on damage’ of carbon occurs under the high e-beam voltage) of the 3L region.

regions we achieved are almost 100% AB-stacked, for regions over multi-centimeter areas of the Cu/Ni(111) foil.

Figure 4.7. Raman mapping of bilayer graphene prepared from polycrystalline Cu/Ni alloy. (a, d, e) Optical image and Raman mapping of the bilayer graphene from region 1. (b) Typical Raman spectra of monolayer graphene, AB-stacked bilayer and misoriented bilayer graphene. (c, f, g) Optical image and Raman mapping of bilayer graphene from region 2.

Figure 4.8. Optical images of graphene samples grown on the Cu/Ni(111) alloy with different Ni concentration: (a) 10.2 at.% Ni, (b) 12.9 at.% Ni, (c) 15.0 at.% Ni, (d) 16.6 at.% Ni, (e) 18.2 at.% Ni, and (f) 20.3 at.% Ni. The growth conditions were the same for these samples.

Figure 4.9. Raman mapping of $^{13}C/^{12}C$ labeled graphene (transferred onto 300-nm SiO_2-on-Si substrates) grown on Cu/Ni(111) foils (16.6 at.% Ni). (a-c), (d-f), and (g-i) are the optical images, Raman maps (2D peak position), and Raman spectra of graphene island, monolayer film, and bilayer film, respectively.

Figure 4.10. 2D Raman peaks of (a) monolayer, (b) bilayer, and (c) trilayer. The 2D peak of monolayer can be fitted by a single Lorentzian, while the bilayer and trilayer can be fitted by four and six Lorentzians, respectively. The fitting indicates that the bilayer and trilayer graphene are both AB-stacked. (d) Optical image of trilayer graphene. The highlighted region indicates the region where Raman mapping was acquired. (e, f) Raman mapping of trilayer graphene. Negligible D peaks and the uniform contrast indicates high quality, uniform ABA-stacking nature over the entire examined trilayer graphene region.

Figure 4.11. Characterization of hexagonal multilayer graphene islands. (a, b) Optical image and Raman spectra of graphene island with 5 layers. (c, d) Optical image and Raman spectra of graphene island with 10 layers.

Figure 4.12. TEM analysis of the bilayer graphene film. (a) TEM image of the bilayer graphene edge that shows two layers. (b, c) HRTEM images of bilayer graphene. The AB-stacked configuration was highlighted in the magnified TEM image (c). (d) A series of SAED patterns were acquired from different regions across the 3 mm diameter TEM grid. The inset in (d) shows the intensity profile along the indicated diffraction spots.

List of tables

Nomenclature

CVD	Chemical vapor deposition
CMGs	Chemically modified graphenes
HOPG	Highly oriented pyrolytic graphite
GO	Graphite oxide
CCG	Chemically converted graphene
GFET	Graphene field-effect transistor
UHV	Ultra-high vacuum
PMMA	Polymethyl methacrylate
PET	Polyethylene terephthalate
F-SAM	Fluoric self-assembled monolayer
PC	Poly(bisphenol A carbonate)
LEEM	Low energy electron microscopy
SEM	Scanning electron microscopy
HR-TEM	High resolution transmission electron microscopy
SAED	Selected area electron diffraction
AFM	Atomic force microscopy
STM	Scanning tunneling microscopy
OM	Optical miscroscopy
LEED	Low energy electron diffraction
GBs	Grain boundaries
FCC	Face-centered cubic
DFT	Density functional theory
POM	Polarized optical microscopy
NLC	Nematic liquid crystal
XRD	X-ray Diffraction
EBSD	Electron back scattered diffraction
XPS	X-ray photoelectron spectroscopy
FWHM	Full width at half-maximum
FIB	Focus ion beam
ToF-SIMS	Time of flight secondary ion mass spectrometry
IWC	Inverted wedding cake

Chapter 1 Introduction

1.1 Introduction to graphene

Graphene is a monolayer of sp^2-bonded carbon atoms or one monolayer of graphite in which the carbon atoms are closely arranged in a hexagonal crystal lattice and is regarded as the fundamental building unit for other carbon allotropes, for example, it can be wrapped up into fullerene (0D), rolled up into carbon nanotube (1D) and stacked into graphite (3D).Graphene has been a very hot subject of research and application over the last 15 years and several groups have published thorough review articles on this topic regarding the history, development, and future research.[1-4] Especially, Ruoff group published a review article in 2010 detailing the definition, history, modern preparation methods and outlook for graphene (This manuscript was accepted for publication before the announcement of the 2010 Nobel Prize in Physics "*for groundbreaking experiments regarding the two-dimensional material graphene*").[4] In this work, the authors examined the history of graphene and chemically-modified graphenes (CMGs) to provide researchers in this field with a broad appreciation of the foundations of graphene science. In terms of the number of graphene layers, monolayer graphene is a single atomic layer of graphene, bilayer graphene is two layers of graphene stacked on top of each other to form either AB-stacked (Bernal stacked as in graphite) or mis-oriented graphene, and trilayer graphene has three layers stacked with different types of stacking order. Multilayer graphene can be regarded as thin graphite if the stacking order is ABA-stacked as in graphite.

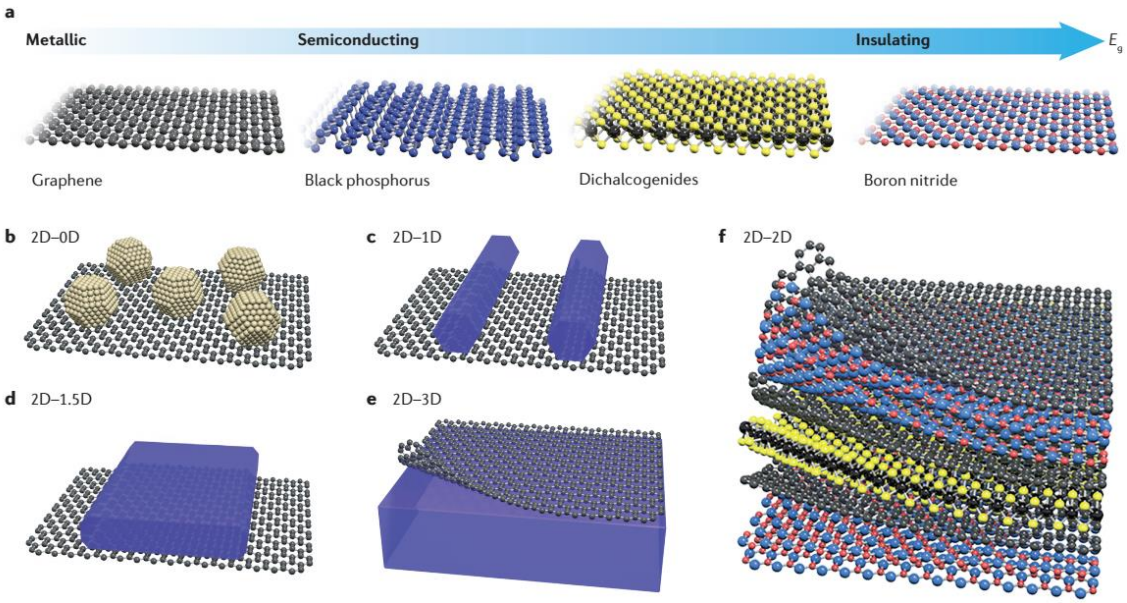

Figure 1.1. Two-dimensional layered materials and van der Waals heterostructures.[5]

Graphene research has not only rapidly developed in the past decade into a mature research area that encompasses solid-state physics, materials science and engineering, but it has also sparked immense

interest in a wide range of two-dimensional layered materials (2DLMs) with diverse electronic properties (see **Figure 1.1**).[5] In addition, many efforts have been devoted to integrate diverse graphene-based van der Waals heterostructures, such as the combination of graphene with 0D quantum dots, 1D nanowires, 3D bulk materials and 2D nanosheets. This extensively heterogeneous integration at the atomic scale would create novel hybrid structures that display totally new physics and enable unique functionality.

Graphene possesses remarkable properties owing to its unique crystal structure. Electrons in a graphene lattice behave as massless Dirac Fermions, resulting in an unusual half-integer quantum Hall effect for both electron and hole carriers in graphene.[6] The room-temperature carrier mobility was found to be over 200,000 $cm^2 V^{-1} s^{-1}$, which is two orders of magnitude higher than that of silicon that is currently used in semiconductor industry.[7] This ultrahigh carrier mobility makes graphene the most promising candidate in high speed electronics, which further stimulates graphene research. In addition, graphene layer has a very high great mechanical strength (Young's modulus could reach 1.0 TPa),[8] a high specific surface area (2630 $m^2 g^{-1}$),[9] good thermal conductivity (5000 W $m^{-1}K^{-1}$),[10] and high optical transmittance (97.7%).[11] These extraordinary properties suggest that the graphene can be used as a multifunctional material in many areas, such as physics, chemistry, nanoelectronics, energy storage, gas/liquid/ion separation, and biotechnology (**Figure 1.2**).[12] Furthermore, the ultrathin (0.34 nm) and chemically inert nature of the graphene film also make it a superlight corrosion barrier for metal protection.

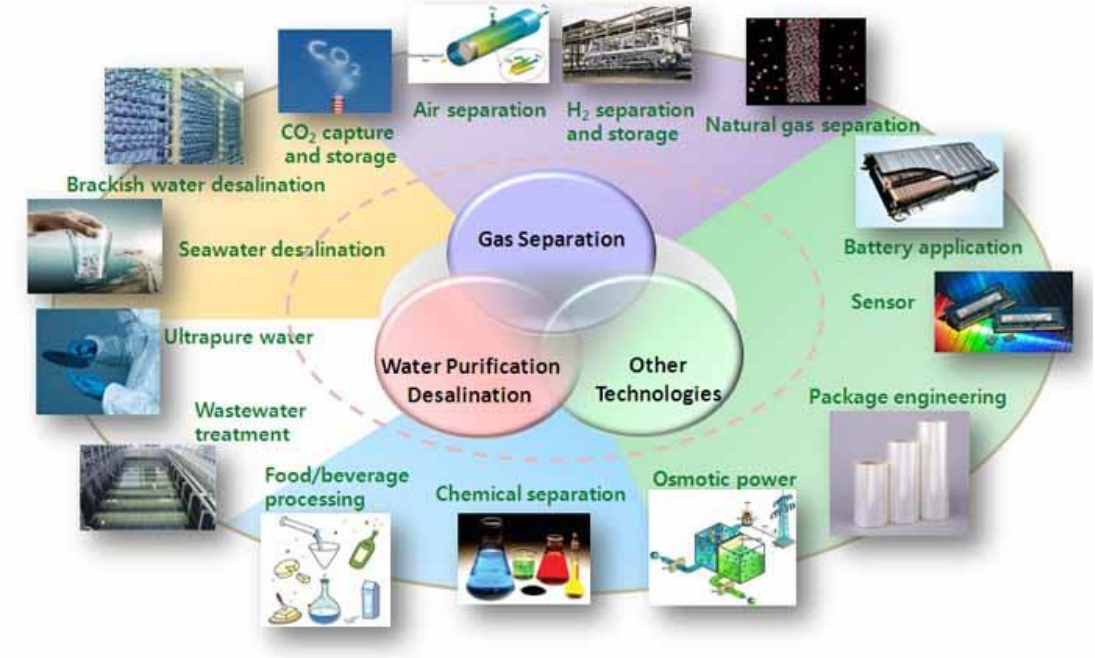

Figure 1.2. An overview of the various applications of graphene.[12]

1.2 Synthesis of graphene

1.2.1 Mechanical exfoliation

In 1999, Ruoff and co-workers micromechanically exfoliated graphite into thin lamellae comprising multiple layers of graphene, where lamellae were not fully exfoliated into monolayer graphene.[13-14] They first used lithographic patterning together with oxygen-plasma treatment to get graphite pillars from HOPG and then converted the pillars into thinner lamellae by a further rubbing process (rubbing the HOPG surface against the surface of other flat substrates). This pioneering work suggested a possible way to exfoliate HOPG to thin graphite layers by a micromechanical approach. In 2004, Geim, Novoselov and colleagues fully realized the potential of this mechanical approach when they first generated thin graphene flakes on a silicon wafer (silicon dioxide on silicon) by a repeated peeling and removing process using an adhesive tape.[15] Such exfoliated graphene flakes are highly visible due to the contrast difference with respect to the 300-nm thick SiO_2 layer on Si wafer and can be easily observed and located by optical microscopy. Geim et al. also determined the thickness of the exfoliated thin graphene layers and characterized their electric-field effects (see details in **Figure 1.3**). This mechanical exfoliation yields graphene that are typically tens of micrometers in size with different thicknesses ranging from monolayer to thick multilayers, suggesting that it is difficult to synthesize graphene on a large scale with well controlled shape, size and number of layers using this method. Exfoliated graphene flakes obtained by this method are now mainly used for basic research and in a few selected applications on a small scale. For large scale production to meet the requirement of industrial applications, new and more effective methods are needed.

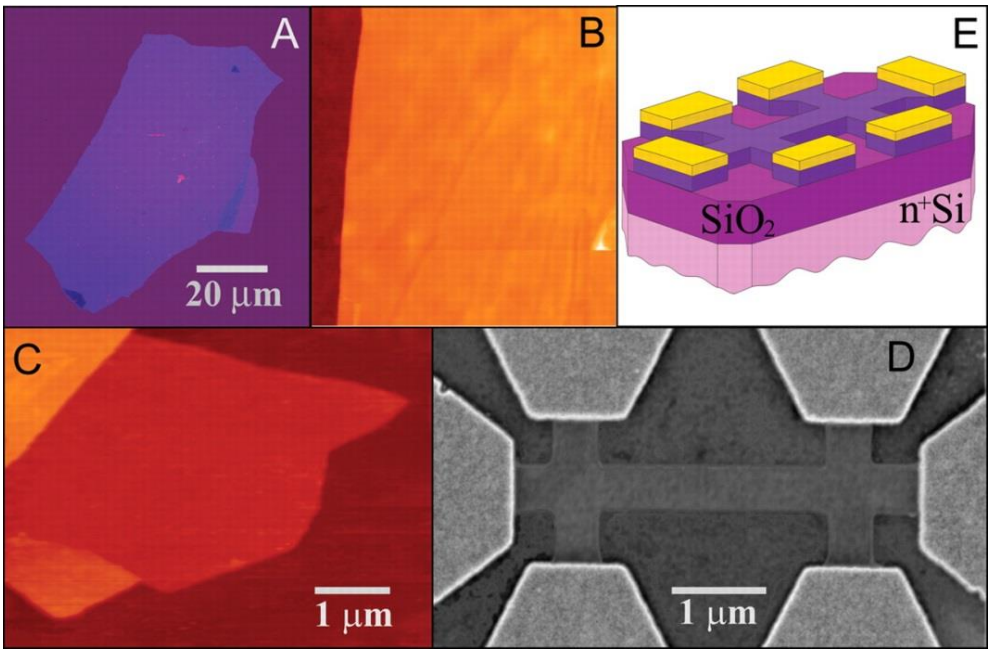

Figure 1.3. Characterization of exfoliated graphene flakes by optical microscopy (OM), atomic force microscopy (AFM) and scanning electron microscopy (SEM).[15]

1.2.2 Liquid phase exfoliation

Apart from dry mechanical exfoliation, liquid phase exfoliation method has also been found to be effective to produce graphene layers on a large scale. The principle behind this method to prepare thin graphene layers is to overcome the van der Waals forces between the adjacent layers of graphite. In the liquid medium, dispersive London interactions (which contribute to a part of the van der Waals forces) are significantly lower than in vacuum, and thus can reduce the strength of the van der Waals forces between adjacent graphene layers.[16] Therefore, the liquid phase exfoliation in an appropriate solvent has been found to be effective to produce thin graphene layers. The liquid-phase exfoliation method typically involves three processes: (1) dispersion of graphite in a solvent, (2) exfoliation using ultrasound/sonication, and (3) further purification of the exfoliated graphene layers. A detailed schematic of the liquid-phase exfoliation method is shown in **Figure 1.4**.[17] This method was first demonstrated by Coleman and coworkers in 2008,[18] who obtained graphene dispersions with concentrations up to ~0.01 mg mL^{-1} by dispersion and exfoliation of graphite in N-methyl-pyrrolidone. The overall yield of monolayer graphene was ~1 wt%, which could be potentially improved to 7–12 wt% with further processing. However, the lack of control of shape, sizes and number of layers still hinder the use of this method to produce large area graphene films for device applications.

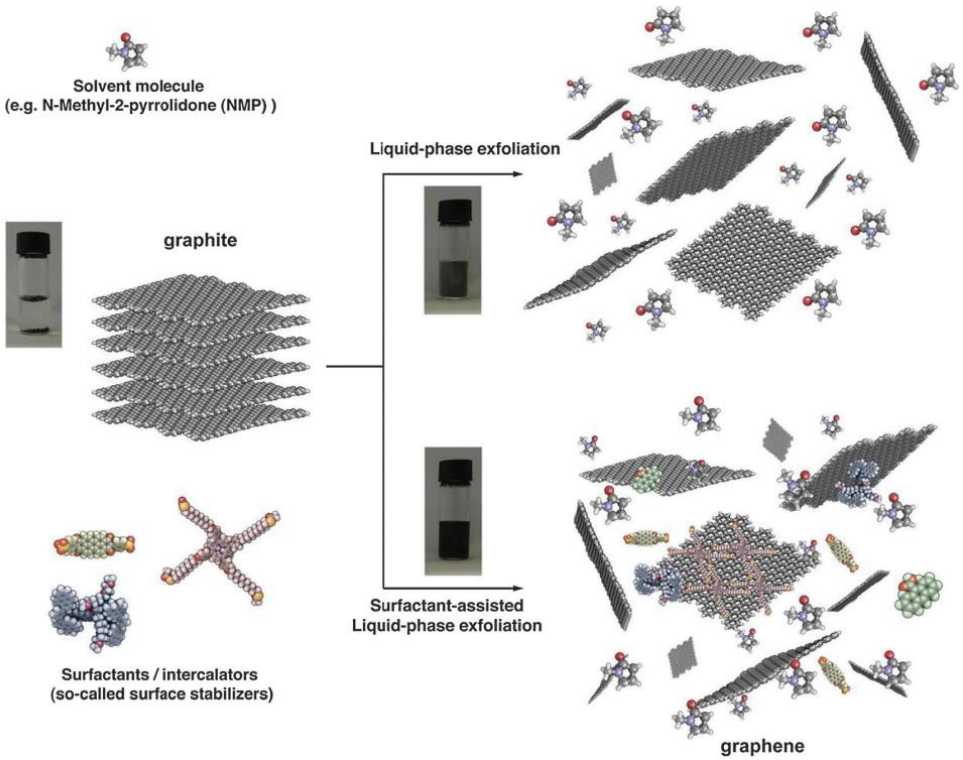

Figure 1.4. Schematic of the liquid phase exfoliation process of graphite in the absence (top-right) and presence (bottom-right) of surfactant molecules.[17]

1.2.3 Electrochemical exfoliation

Electrochemical exfoliation is also a wet-chemical exfoliation method using graphite as an electrode and applying a voltage between the negative and positive electrodes.[19-21] The electrochemical exfoliation method takes advantage of graphite's conductive properties to intercalate molecules and or ions between graphene layers. These molecules/ions induce expansion of the interlayer space in graphite and thus facilitate the exfoliation process. The setup for electrochemical exfoliation consists of graphite working electrode, counter electrode, electrolyte, and power supply (a typical setup is shown in **Figure 1.5**).[22] Typically, highly orientated pyrolytic graphite (HOPG), graphite rods, graphite foil, or graphite flakes are used as the working electrode. There are essentially two approaches to electrochemical exfoliation, namely, the cathodic and the anodic approach, depending upon whether a positive or a negative voltage is applied to the graphite working electrode.[23] The electrochemical approach is a more effective method for the mass production of graphene at lower cost when compared to the mechanical exfoliation method. However, similar to other liquid-phase exfoliation methods, the electrochemical exfoliation process may also cause irreversible functionalization (slight oxidation) and graphene sheets with non-uniform thickness are obtained, thereby lowering the electronic properties of graphene.

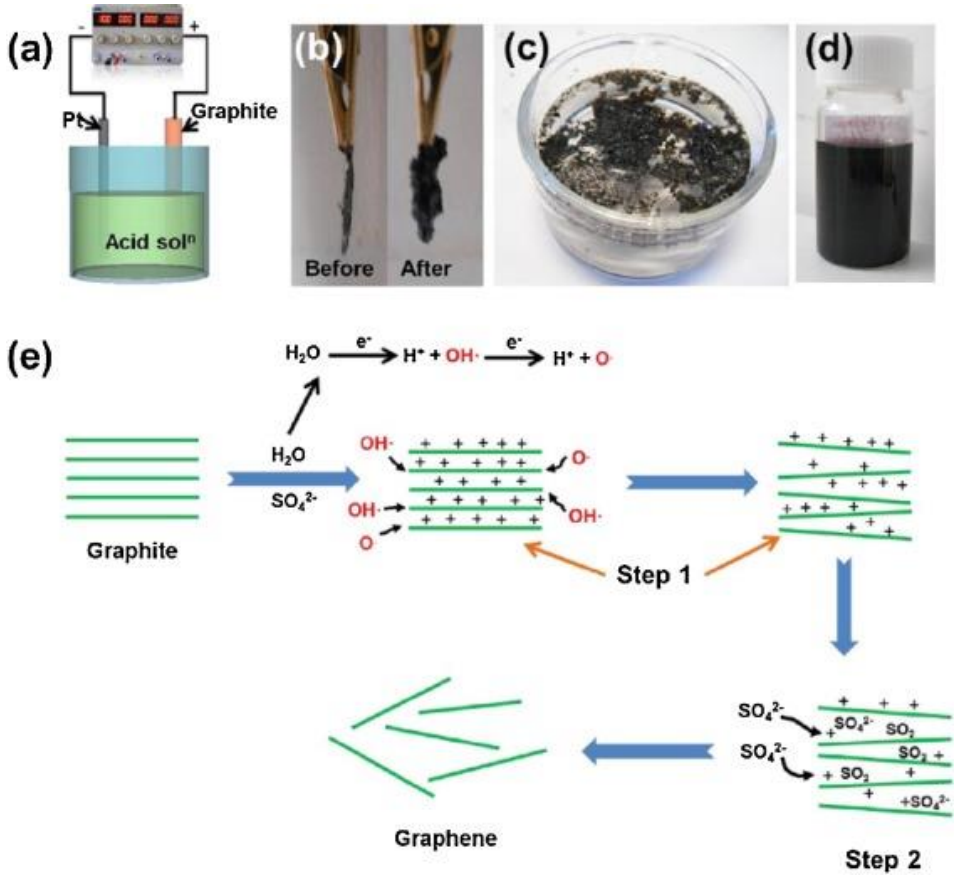

Figure 1.5. Schematic illustration of the electrochemical exfoliation setup and the characterization of the exfoliated graphene flakes.[22]

1.2.4 Reduction of graphene oxide

A widely used method for the synthesis of graphene is by chemical reduction of graphene oxide; the process is shown in **Figure 1.6**.[24] This method includes three steps: (1) oxidization of graphite, (2) exfoliation of graphite oxide by mechanical/chemical treatment, and (3) reduction of the exfoliated graphene oxide to get graphene. In the first step, the natural graphite powder is always used as the precursor to synthesize graphite oxide. The typical method of synthesizing GO was developed by Hummers and co-workers.[25] Graphite was oxidized by treatment with $KMnO_4$ and $NaNO_3$ in concentrated H_2SO_4 followed by mechanical/chemical or thermal exfoliation of graphite oxide to form graphene oxide sheets. The graphene oxide sheets can then be chemically or thermally reduced to graphene sheets.[26-30] This method of graphene oxide reduction exhibits high yield, high dispersability and high processability, all of which are crucial for large scale production. However, chemically-obtained graphene contains large amounts of functional groups and abundant defects, which hinder its applications in areas of quantum physics, electronic devices and in surface protection.

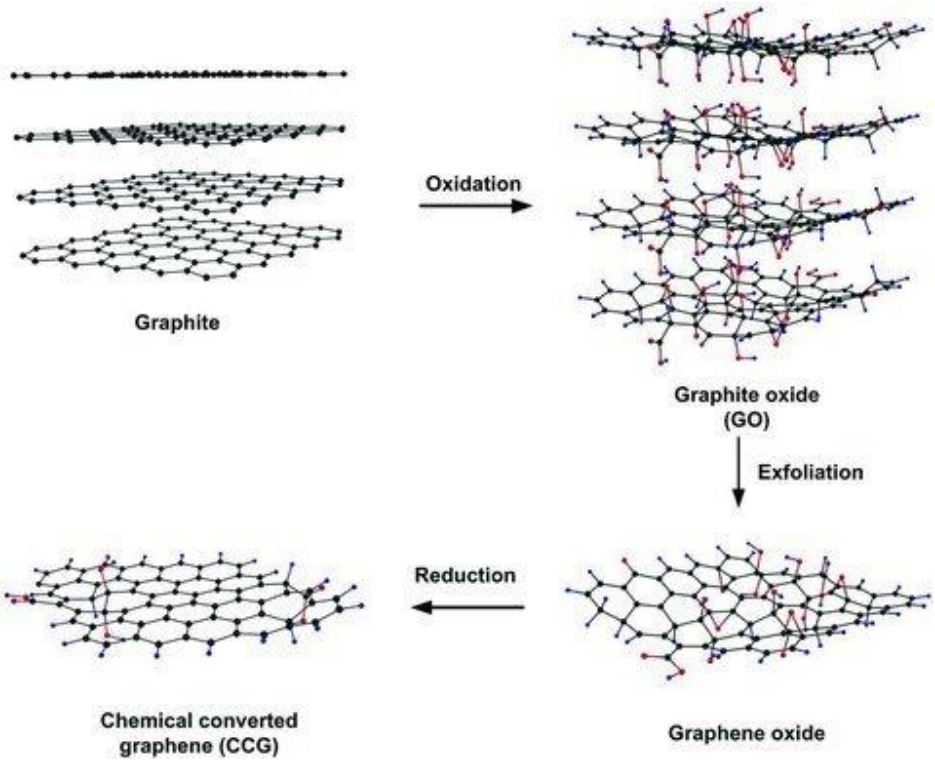

Figure 1.6. Preparation of chemically converted graphene (CCG) by reduction of graphene oxide.[24]

1.2.5 Epitaxial growth

Epitaxial growth refers to the deposition of a crystalline overlayer onto a crystalline substrate, where the overlayer, also called an epitaxial film or epitaxial layer, aligns itself to the structure of the underlying substrate. Badami and coworkers first demonstrated the graphitization of the surface of a SiC single crystal in 1965.[31] They found that when SiC crystals were heated in an induction furnace

for one hour to ~2280 ℃ the *c*-axis of graphite was aligned along the c-axis of the hexagonal SiC crystal. This method is based on the depletion of Si on the SiC surface by high temperature treatment. In the next several decades following Badami's findings, epitaxial graphene growth on SiC has progressed further, and currently, homogeneous monolayer, bilayer, and further graphene layers on SiC(0001) can be obtained.[32-35] The typical process for the growth of epitaxial graphene on SiC substrates by surface Si depletion is illustrated in **Figure 1.7**.[36]

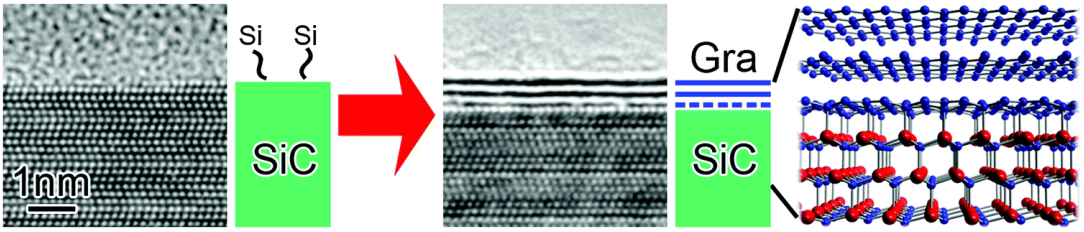

Figure 1.7. Basics of graphene growth by thermal decomposition of SiC, together with the structural model of bilayer graphene on SiC.[36]

There are several advantages to growing graphene epitaxially on SiC: (a) the obtained graphene shows high quality with less defects due to the epitaxial growth from the underlying high quality SiC crystal; (b) the number of graphene layers can be roughly controlled by tuning the heating temperature; (c) graphene grown on SiC substrate can be directly fabricated for electronic devices without the need for transfer. However, the high cost of SiC crystals and the limited size of the as-prepared graphene flakes still hinder the wide use of this method for large-scale graphene production.

1.2.6 Chemical Vapor Deposition (CVD)

Although many methods have been explored and used in the preparation of graphene, none of these can achieve high quality graphene films on a large scale with controlled layer thickness, grain size, stacking order, and defects density. Early works (late 1960s) have indicated that the high temperature treatment of certain transition metals in hydrocarbon atmosphere could produce thin graphite films.[37-38] By referring to these previous works, CVD growth of graphene was established and has been extensively studied since then.[39-41] Specially, the work published in *Science* by Ruoff and co-workers showed a promising future for the use of CVD method for the synthesis of large-area monolayer graphene (see detailed result in **Figure 1.8**). In this work, they achieved large-area graphene films with cm^2 area on commercial copper substrates by CVD using methane as the carbon precursor in less than half an hour. The size of the graphene film in this method is only limited by the size of the CVD chamber and/or the copper substrate, and the growth time can be extremely short (a few minutes) by tuning the growth temperature and methane gas flow rate. Consequently, the CVD method using Cu foil as a growth substrate has been widely used for graphene growth for both research and industry

production. Thus, the focus of this thesis is the further exploration or optimization of this CVD method for the high quality graphene growth.

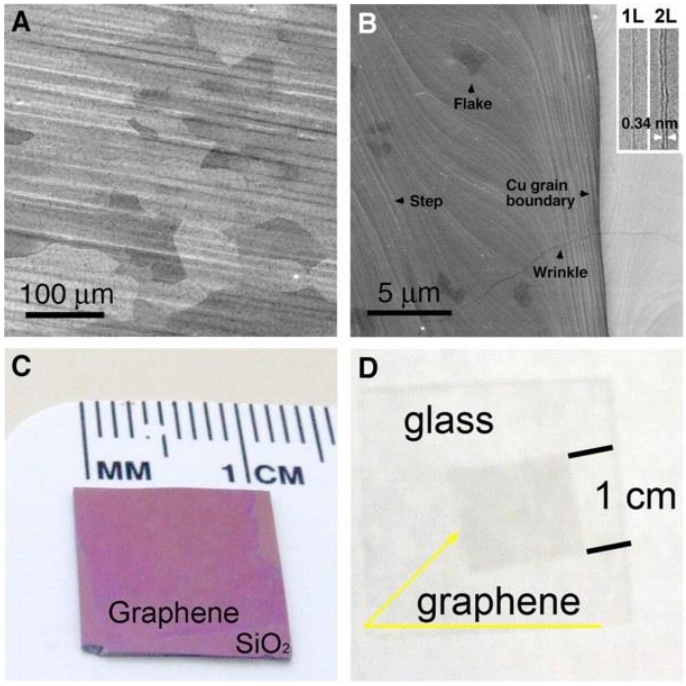

Figure 1.8. (A) SEM image of graphene on a copper foil with a growth time of 30 min. (B) High-resolution SEM image of the graphene on Cu. (C and D) Graphene films transferred onto a SiO_2/Si substrate and a glass plate, respectively.[41]

In addition, the high quality graphene film achieved on copper substrates in recent years has shown electrical properties close or even equal to that of graphene obtained by the exfoliation of HOPG.[42-44] Nevertheless, despite the obvious advantages of the CVD method, an in-depth understanding of the growth mechanism, as well as a control of the crystallinity and layer number of the graphene films still remains a great challenge.

1.3 Metal substrates for CVD growth of graphene

CVD growth process of graphene on metal mainly includes four elementary steps (a schematic is shown in **Figure 1.9**)[45]: (1) adsorption and catalytic decomposition of carbon precursor; (2) the diffusion and/or dissolution of the decomposed carbon precursor radicals on and/or into the metal substrate, (3) segregation of dissolved carbon on the metal surface (this depends on the type of metal substrate used for growth, such as Ni, which has high carbon solubility); (4) surface nucleation and carbon segments attachment to form graphene. All these steps are highly dependent on the properties of the metal substrate used in the CVD growth process and hence the size, thickness and quality of the graphene are determined and affected. Therefore, it's crucial to choose or design an appropriate substrate for high quality graphene film growth.

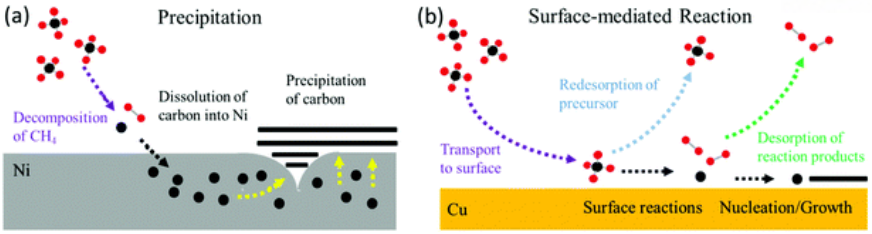

Figure 1.9. Schematic of the graphene growth mechanism *via* (a) precipitation and (b) surface-mediated reaction on different metal substrates.[45]

1.3.1 Nickel

Before 2009, the most frequently used substrate for CVD growth of graphene was Ni. Referring to the systematic statistics of the solubility of carbon in various metals,[46] the solubility of C in Ni at a temperature of 1000 ℃ could reach more than 1.3 at.%. When using Ni as a substrate for graphene growth, the obtained graphene always suffers from non-uniform thickness and homogeneity. This is because the carbon species/atoms can diffuse into the bulk Ni substrate to form a solid solution at the growth temperature and precipitate out to form non-uniform adlayers during the cooling process due to the decreased carbon solubility with decreasing temperature. In light of this disadvantage, many strategies such as controlling the cooling rate, using a thin Ni film instead of a Ni foil, applying low pressure growth and decreasing the growth temperature, have been used to control the dissolved carbon in the Ni to get a more uniform graphene film.[47-50] In addition, the microstructure/crystallinity of the Ni substrate was also indicated to have an important role in the formation of graphene films. Zhou and co-workers reported a comparative study of graphene growth on single crystal Ni(111) and polycrystalline Ni substrates (**Figure 1.10**).[51]

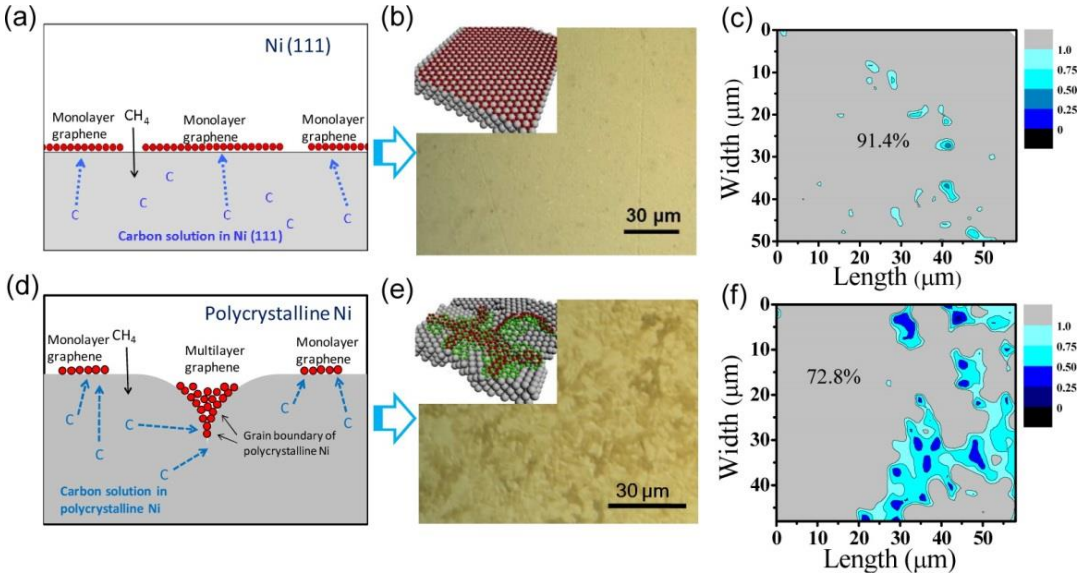

Figure 1.10. A comparison of graphene growth on single crystal Ni(111) and polycrystalline Ni substrate.[51]

They found that the graphene thickness on Ni(111) substrate is much smaller than that on polycrystalline Ni and the coverage of monolayer and bilayer graphene are much higher. They attributed this result to the smooth surface and less grain boundaries in the single crystal Ni(111) substrate. In contrast, the abundant grain boundaries on polycrystalline Ni served as nucleation sites for non-uniform multilayer graphene growth.

1.3.2 Copper

Inspired by the pioneering work on high quality single layer graphene growth on commercial Cu foil reported by Ruoff group,[41] researchers have paid a lot attention to using Cu as the substrate due to its low carbon solubility. Carbon solubility in Cu at 1000 ℃ is around 0.04 at.%,[46] which results in negligible carbon dissolution during the CVD growth process. Therefore, during the decomposition of hydrocarbon on the Cu surface, carbon radicals/atoms nucleate and attach carbon segments to form graphene domains. The growth process will terminate when the substrates are fully covered by a graphene layer; this process is usually referred to as a 'surface mediated' or 'self-limited' growth mechanism. In this growth mechanism, carbon dissolution and subsequent segregation and/or precipitation can be neglected. Distinct from graphene growth on Ni foil, graphene grown on Cu is always monolayer with a coverage of more than 95%. In the recent years, many works have reported large area monolayer graphene and/or single crystal graphene islands/films on Cu foil by substrate engineering, tuning growth condition, and by using different carbon source.[52-54] In 2013, Yufeng Hao and co-workers reported large size single crystal graphene growth on O_2-treated Cu foil (**Figure 1.11**)[55] where they discovered that oxygen on the Cu surface substantially decreased the graphene nucleation density by passivating surface active sites on Cu. A control of surface oxygen enabled the repeatable growth of centimeter-scale single-crystal graphene domains. GFET devices made from these single crystal graphenes showed high carrier mobilities ranging from 15,000 to 30,000 $cm^2 V^{-1} s^{-1}$ at room temperature, indicating the high quality of the as-prepared graphene.

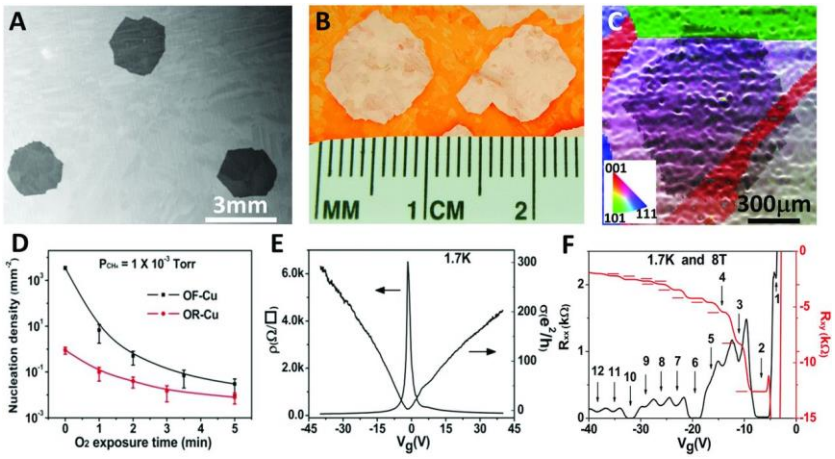

Figure 1.11. Size, structure, and electrical transport properties of large graphene domains grown on Cu exposed to O_2.[55]

1.3.3 Cobalt

As a common catalyst (along with Ni and Fe) for carbon nanotube growth, cobalt (Co) has also been used as the substrate for graphene growth. Due to the high carbon solubility in Co at high growth temperatures, graphene growth on Co is a segregation/precipitation dominated process. Ago and co-workers reported graphene growth on single crystalline Co films.[56] The single crystalline Co film was prepared on sapphire by sputtering at a high temperature followed by H_2 annealing. The effect of the crystallinity of the Co film was investigated by comparing graphene grown on crystalline Co film/sapphire substrate to that on a polycrystalline Co film/SiO_2-Si substrate. They found an epitaxial relationship between the graphene and the underlying crystalline Co film/sapphire substrate and the graphene thickness was much more uniform on single crystalline Co as compared with that grown on a polycrystalline Co film/SiO_2-Si substrate. Zheng and colleagues have prepared graphene with different layer numbers ranging from 1 to 5 on a polycrystalline Co film by radio-frequency plasma-enhanced CVD at a relatively low temperature of 800 °C for only 40 s (**Figure 1.12**).[57] The graphene showed high quality as confirmed from Raman spectroscopy and X-ray photoelectron spectroscopy and also showed an optical transmittance of around 70% in the wavelength range 500–1200 nm, indicating the non-uniform thickness of the as-prepared graphene film. Jung and co-workers have also used a Co film deposited on SiO_2/Si substrate for graphene growth.[58] In this work, they have compared graphene growth results on Co and Ni films and found that graphene grown on a Co film is thinner than that on Ni under the same growth conditions, which they attributed to the larger grain size of the Co film as compared to the Ni film (a lower grain size will induce more grain boundaries for carbon dissolution and result in greater segregation/precipitation).

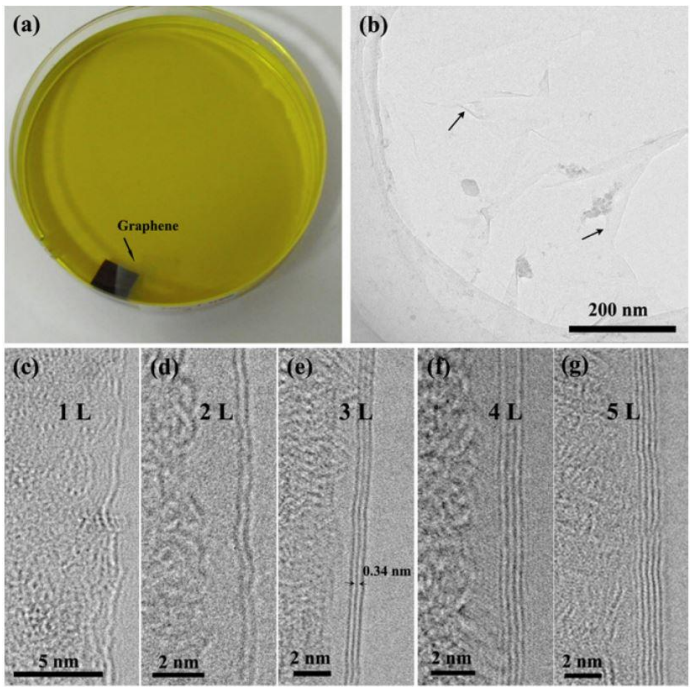

Figure 1.12. Optical and TEM images of the transferred graphene from Co substrate.[57]

1.3.4 Ruthenium

Experimental and theoretical results have indicated that the graphene growth depends strongly on the interaction between graphene and the metal substrate. In this respect, Ru is a special substrate when compared to Cu since graphene is strongly chemisorbed on Ru(0001) substrate *via* a significant hybridization of C 2*pz* states and Ru *d*-states.[59] In 2008, Sutter and co-workers reported the growth of single-crystalline graphene islands on Ru(0001) substrate in a UHV system (**Figure 1.13**). In this work, they monitored graphene growth on a Ru surface using in-situ LEEM technique. They observed that graphene showed a fast expansion in the direction parallel to steps on the substrate and across steps in the 'downhill' direction. This growth pattern was explained to be due to the different energy barriers in different directions for graphene growth.

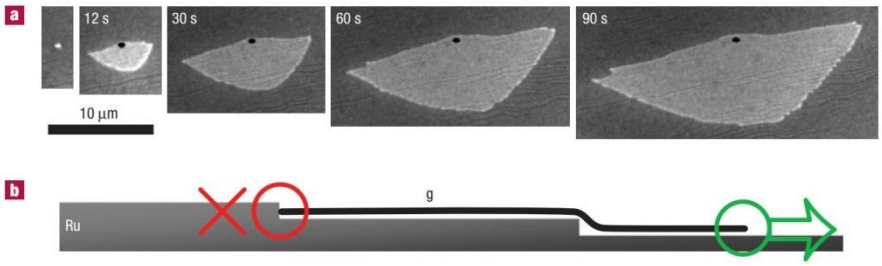

Figure 1.13. In situ microscopy of graphene epitaxy on Ru(0001).[59]

Sutter group also investigated graphene growth both on an epitaxial Ru thin film on sapphire and on a polycrystalline Ru film deposited on a SiO_2/Si substrate.[60-61] Bao and colleagues have also used in-situ LEEM to study the graphene growth behavior on Ru(0001) substrate[62] where they found that graphene growth can be tuned or tailored by surface engineering; for example, graphene grown on a clean Ru(0001) substrate had the shape of a sector, but it was circular on the surface treated by Ar^+ sputtering. This difference in shape was attributed to subsurface Ar gas bubbles induced during Ar^+ sputtering process, which affected the graphene growth process.

1.3.5 Iridium

Ir is also a commonly used substrate for graphene growth under low pressure conditions. Coraux and co-workers reported the low pressure CVD (LPCVD) growth of monolayer graphene on Ir(111).[63] The as-prepared graphene exhibited large-scale continuity of its carbon rows over terraces and step edges when imaged using scanning tunneling microscopy (STM). One year after this work was published, their group tried to investigate the effect of growth conditions (mainly temperature) on graphene growth on Ir substrate.[64] They employed two growth methods for graphene on Ir(111), namely, room temperature adsorption and thermal decomposition at 870–1470 K (temperature programmed growth (TPG)), and direct exposure of the hot substrate at 870–1320 K (chemical vapor deposition (CVD)). Their result showed that TPG facilitates the formation of small graphene islands with sizes ranging

from a couple of nanometers to several hundreds of nanometers, depending on the growth temperature. While the CVD favors the synthesis of large area graphene with coverage up to 100% of the substrate surface, providing a reproducible method for the growth of macroscopic single-layer graphene with high crystalline quality.

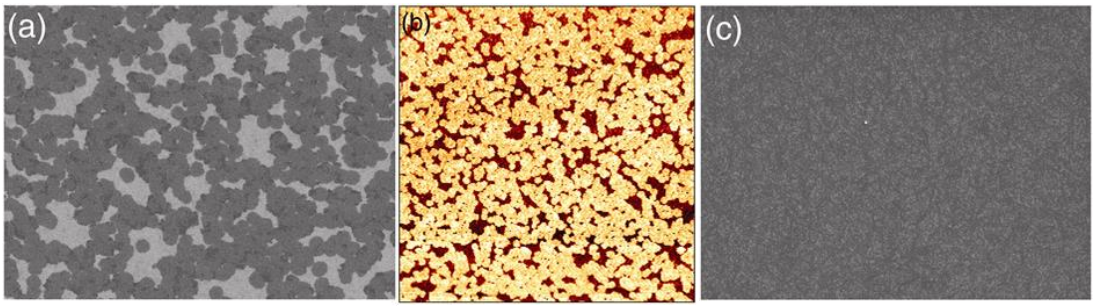

Figure 1.14. SEM and AFM images of an incomplete graphene layer (a, b) and a continuous graphene film (c).[65]

In 2011, Hattlab et al. conducted a systematic study of the change in the structure of graphene on Ir(111) as a function of the CVD growth temperature.[66] They found that the orientation of the as-formed graphene domains with respect to the Ir substrate is highly dependent on the growth temperature. Typically, graphene domains showed high disorder and structural disintegrity at temperatures below 1200 K, while they were in a single orientation epitaxial incommensurate phase for temperatures higher than 1500 K. In the temperature range between 1200 and 1500 K, graphene formed showed a large fraction of well oriented grains along with some randomly oriented domains. This report thus provided an route to control the orientation of graphene grown on Ir. Wintterlin and co-workers reported the scalable synthesis of graphene on single crystal Ir(111) films prepared by hetero-epitaxial growth on Si(111) wafers with yttria-stabilized zirconia (YSZ) as a buffer layer (**Figure 1.14**).[65]

1.3.6 Platinum

Pt is another metal that has been extensively used as a substrate for graphene growth.[67-70] Cho group reported monolayer graphene growth on a sputtered platinum thin film and they found that good surface morphology (small surface roughness and large grain size) is the key to enabling uniform large area monolayer graphene growth on Pt substrate.[67] Gao and co-workers reported the epitaxial growth of graphene on Pt(111) surface.[68] They found that the proportion of different rotational domains varies with growth temperature and that graphene quality can be improved by controlling the CVD growth temperature and the carbon source (ethylene used in this work) exposure. Cheng group demonstrated the growth of millimeter-sized graphene single-crystals on Pt by ambient-pressure CVD.[71] By using a bubbling transfer method (also known as electrochemical delamination method), they could reuse the Pt substrate for graphene growth (**Figure 1.15**). Sun and co-workers have

reported graphene (monolayer, bilayer and some multilayer islands) growth on Pt and studied the growth mechanism.[72] In their proposed mechanism, monolayer graphene is formed by a self-limiting process (surface catalysis effect) at a high growth temperature and the bilayer/multilayer is formed *via* a segregation process during cooling. Thus, a predominantly monolayer graphene film with high quality can be selectively synthesized by controlling the kinetic parameters.

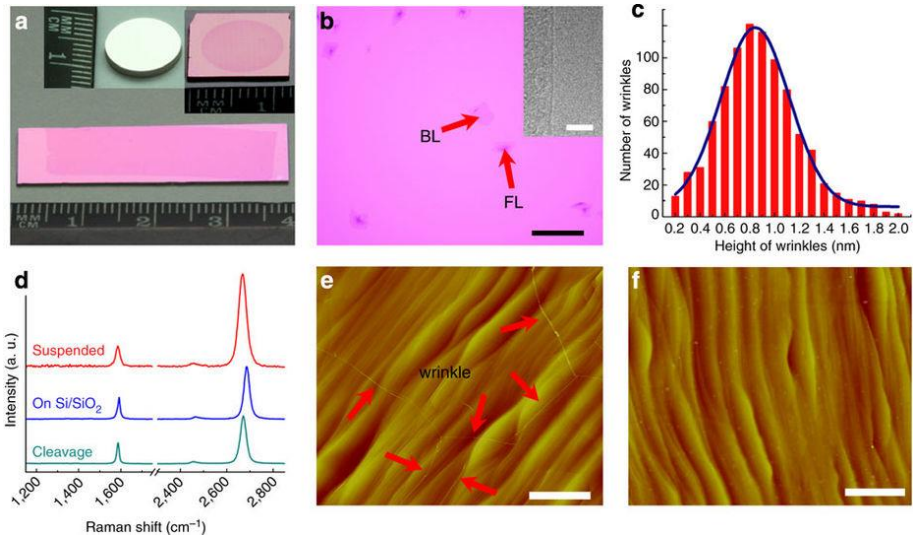

Figure 1.15. Repeated growth and bubbling transfer of millimeter-size single-crystal grains of graphene formed using platinum substrate.[71]

While considering all the efforts for the graphene growth on these metal foils we mentioned above, the Cu foil is the best choice for the preparation of large area monolayer graphene film. However, the fine control for the layer number of graphene on all of these metals has not been achieved.

1.4 Motivation and goal

Despite significant progress in optimizing the CVD method used for high quality graphene films growth, many challenges and problems still exist. First of all, exploring and/or designing of new substrates for fast growth (in a few minutes) of large-area high quality graphene films for industrial production would be very important. Second, the synthesis of large-size single-crystal graphene or highly oriented graphene film (formed by merging highly oriented graphene islands) is also crucial (since the grain boundaries in the polycrystalline graphene film will degrade its property) to expand the use of graphene to many electronic or photonic-related applications. Third, the controlled synthesis of graphene films where the number of layers (AB-stacked bilayer graphene can be used in semiconductor due to its tunable bandgap with a perpendicularly applied tunable electrical field) and their stacking sequence can be tuned. Finally, a deeper understanding of the graphene growth behavior and mechanism is also needed.

Meaningful improvements in graphene synthesis require understanding not only its specific peculiarities but also the fundamental process of the graphene growth during the CVD process. In this thesis, we focus on these challenges and present the various strategies we have used for achieving the large-area high quality graphene film with tunable layer numbers and studied the multilayer stacking sequence/stacking order and also the graphene growth mechanism.

Chapter 2 describes the main fabrication and characterization techniques for the graphene. Chapter 3 explores how to prepare single-crystal graphene film in a large scale: a single crystal Cu/Ni(111) foil was applied for the fast growth of graphene. The influence of the Ni content and also the graphene growth mechanism on this Cu/Ni(111) alloy was discussed in detail. It further gave a detailed characterization of the quality of the as-prepared graphene. A folding phenomenon on both the joined island and continuous monolayer graphene film was also explored. Chapter 4 systematically investigates the Ni content for the growth of layer-tunable graphene film. The growth mechanism of the graphene on the high Ni content alloy was also studied by the isotope-labelled experiment. The layer structure of the bi/tri and multilayer graphene was studied by ToF-SIMS depth profiling/mapping, in-situ SEM with hydrogen etching, and cross-section TEM imaging. Chapter 5 gave a summary of the main findings in this thesis and also proposed some future research directions.

Chapter 2 Experimental techniques

2.1 Substrate preparation and CVD growth of graphene

In this thesis, Cu/Ni(111) alloy foils were mainly used as the substrates for graphene growth. The alloy foils may contain a thin layer of oxides and/or adsorbed organic impurities (especially if used after being stored for a certain period of time) which affect the graphene quality during the CVD process. Prior to loading the Cu/Ni(111) foils into the CVD chamber, they are treated with acetic acid (CH_3COOH), deionized water (DI water), and acetone, in that order, and then blow-dried with N_2 gas.

In the CVD growth of graphene, there are mainly five steps: (1) Vacuum pumping of the CVD growth system, (2) ramping up to the graphene growth temperature, (3) substrate annealing at the growth temperature, (4) graphene growth, and (5) cooling of the substrate. Pretreated Cu/Ni(111) foils were loaded into the inner quartz tube (4 cm in diameter) and this inner tube was inserted into the CVD growth chamber which was then pumped down to ~0.3 mTorr. After purging with Ar gas for a few cycles, the chamber was fed with Ar and H_2 gas to adjust and maintain a constant pressure. The temperature was increased to the growth temperature (typically 1075 ℃) in 1 h and held for another 1 h at this temperature. Methane gas was then introduced into the system for graphene growth. After growth, the furnace was turned off and the substrate was rapidly cooled by sliding the furnace (naturally cooling of the sample region) downstream. A typical CVD growth process (temperature-time profile) is shown in **Figure 2.1**.

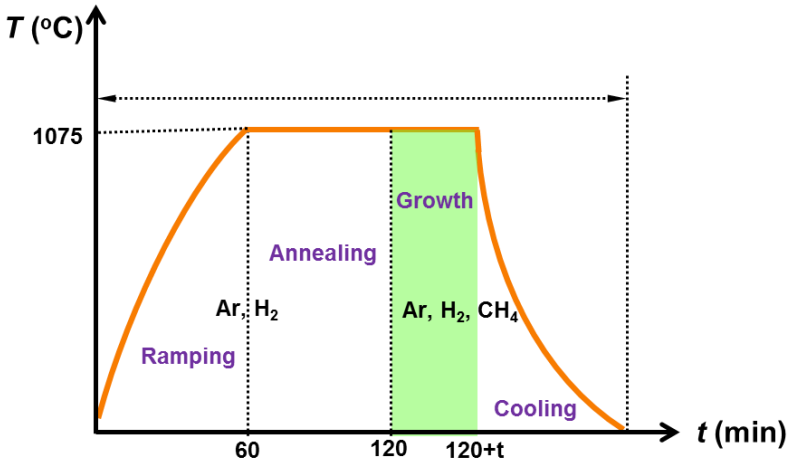

Figure 2.1. A typical temperature-time profile for the CVD growth of graphene.

2.2 Graphene transfer

2.2.1 Conventional PMMA-assisted transfer method

Considering the characterization and the application of the graphene films, it's essential to transfer graphene from the metal substrates onto target substrates. The typical PMMA-assisted transfer method includes the following steps (**Figure 2.2**)[73]: (1) Spin-coating a layer of PMMA on one side of a graphene/Cu foil; (2) O_2 plasma treatment to remove the graphene on the other side (without PMMA

coating); (3) Cu etching in aqueous $FeCl_3$ or $(NH_4)_2S_2O_8$; (4) floating the PMMA/graphene film on a diluted HCl solution or DI water for cleaning; (5) transferring the PMMA/graphene film onto the target substrate; and (6) removing the PMMA layer by acetone.

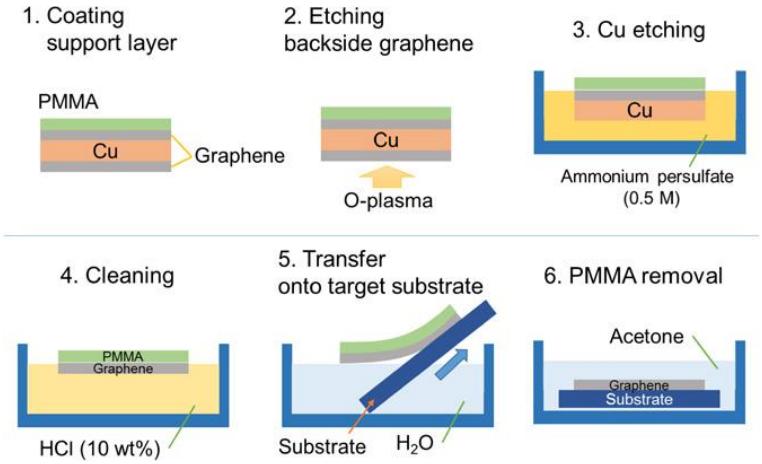

Figure 2.2. A schematic of the conventional PMMA-assisted graphene transfer process.[73]

The PMMA-assisted transfer method is a universal method to transfer graphene from Cu and/or Ni onto various target substrates, but this process can result in contamination from the etchant solution and also has some limitation for the transfer of graphene from the metal substrates with high carbon solubility.

2.2.2 Support-free transfer method

The conventional PMMA-assisted (or other polymers) method invariably suffers from support material residues left on the surface of the transferred graphene films. Therefore, support-free transfer methods are highly desirable for a clean transfer of the CVD-grown graphene onto target substrates.

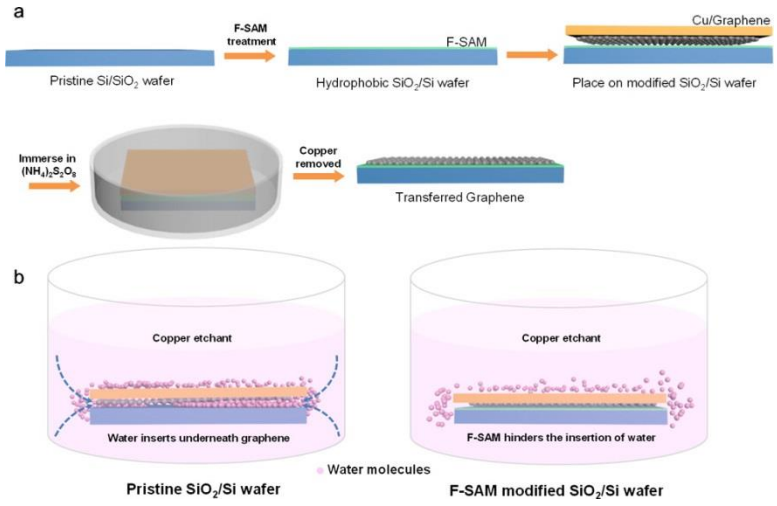

Figure 2.3. Illustration of transferring graphene onto fluoric self-assembled monolayer (F-SAM) modified substrates.[74]

Our group has developed a support-free transfer method for transferring graphene onto fluoric self-assembled monolayer (F-SAM) modified substrates such as Si wafer, polyethylene terephthalate (PET) films, and glass.[74] The transfer process mainly involves the following steps: (1) Target substrate modification (treatment) by trichloro-(1H,1H,2H,2H-perfluorooctyl) silane self-assembled monolayers (F-SAM); (2) gently pressing a piece of Cu/graphene on the modified substrate (with the graphene side contacting the substrate); (3) Cu etching by etchant; (4) sample washing in deionized water. In this work, we have compared the transfer onto bare SiO_2/Si wafer and F-SAM-modified SiO_2/Si wafer. It was found that the graphene films tend to detach from the bare SiO_2/Si wafer and become suspended in water (and break) due to water molecules diffusing between the graphene and substrate (**Figure 2.3b**). In contrast, the insertion/diffusion of water molecules was hindered by the hydrophobic groups of the SAM layer (the adhesion between the graphene and the substrate was maintained) on the modified F-SAM-coated SiO_2/Si wafer-treated substrate during the Cu etching process. This approach provides an efficient and clean route for transferring CVD-grown graphene films onto different substrates.

2.2.3 Dry transfer method

Ruoff group recently reported a dry transfer method by using poly(bisphenol A carbonate) (PC) as the support layer.[75] In this work, the copper foil was preserved and could be further reused for graphene growth without substantial weight loss. The typical transfer process and the characterization of the transferred graphene is shown in **Figure 2.4**.

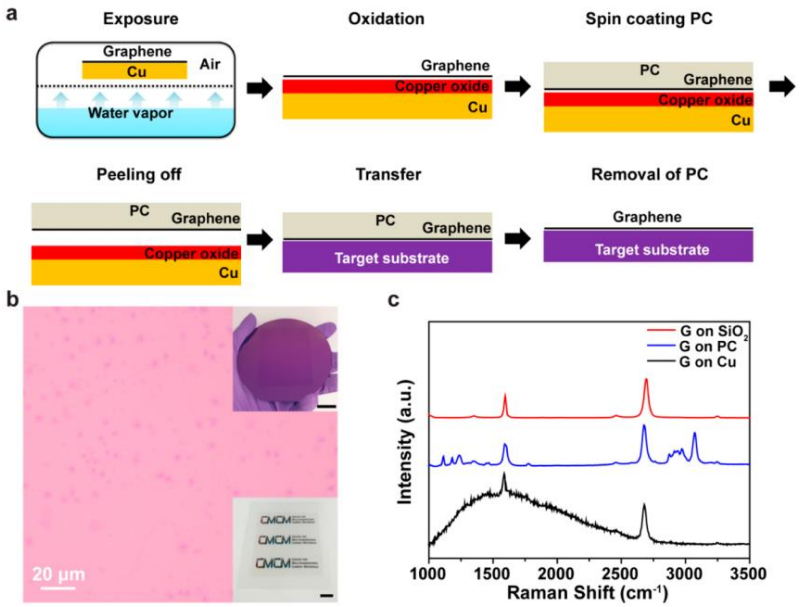

Figure 2.4. Direct delamination and transfer of graphene from Cu to a 300 nm SiO_2/Si wafer through exposure to water-saturated air.[75]

In this dry transfer process, the delamination of graphene when using PC as a support layer (capping layer) is due to the weakened adhesion between the oxidized Cu foil and graphene following the oxidation of the Cu foil by water-saturated air. The detailed transfer process includes six steps: (1) Oxidation of the graphene/Cu sample in water-saturated air (50 ℃ for 24 h); (2) spin coat a PC layer onto graphene/Cu; (3) baking the PC/graphene/Cu stack on a hot plate (150 ℃) for 10 min to increase the adhesion between graphene and the PC film; (4) peeling off the PC/graphene layer using a tweezer; (5) transferring the PC/graphene layer onto a target substrate; (6) removing the PC layer with chloroform. This dry transfer method yielded graphene with lower amounts of both Cu impurity and polymer residues as compared to the conventional PMMA-assisted transfer method with the etching of Cu.

2.2.4 Electrochemical delamination method

The conventional Cu etching transfer method and dry transfer method by oxidization of Cu are both time-consuming and also result in metal residues, and are therefore not suitable for the large-area graphene transfer in industrial applications. In addition, these two methods cannot be used for substrates made from chemically-inert metals or metal alloys (such as Pt, Cu-Pt alloy, and Cu/Ni alloy). The electrochemical delamination method can address these issues and realize the fast and nondestructive transfer of graphene from almost all types of metal substrates. Loh and co-workers first reported the electrochemical delamination of graphene from a Cu foil substrate using $K_2S_2O_8$ (0.05 mM) as the electrolyte.[76] Later, Cheng and colleagues used a similar process to transfer graphene from Pt substrates by using NaOH (1 M) as the electrolyte.[71] The electrochemical delamination method is also called “bubbling transfer” since the graphene is detached from the metal substrate by hydrogen bubbles produced between graphene and metal surface after applying a voltage. The electrochemical delamination method includes five steps: (1) PMMA layer coating on the graphene/metal substrate; (2) using the PMMA/graphene/metal stack as the cathode and inserting it into the electrolyte; (3) applying a voltage between the cathode and anode (always a Pt substrate as a counter electrode) and detaching the PMMA/graphene stack from the metal substrate; (4) transferring the PMMA/graphene stack onto the target substrate; (5) removal of the PMMA layer by acetone.

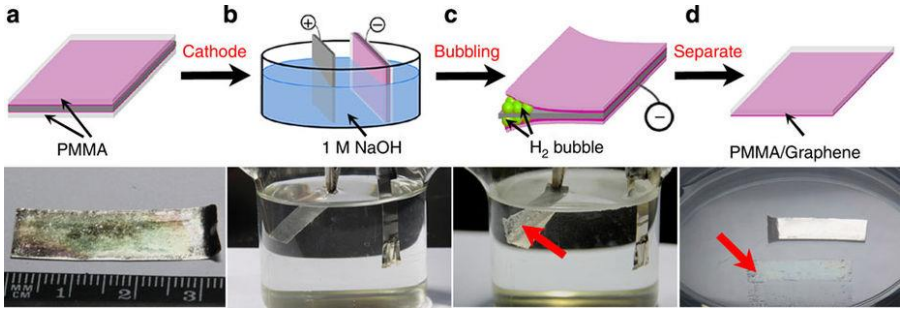

Figure 2.5. Illustration of the bubbling transfer process of graphene from a Pt substrate.[71]

2.3 Characterization techniques

Since uniformity, number of layers, and quality of graphene, are very important for both scientific research and industrial application, a thorough characterization of the as-prepared graphene is crucial.

2.3.1 Optical microscopy

Optical microcopy can be used to check the morphology, coverage, uniformity, and the number of layers of the transferred graphene on 300-nm thick SiO_2-on-Si wafer.[15] It was found that the light interference from a SiO_2 substrate can be modulated by the overlaid graphene layers, and the change in color contrast can be used to determine the variations in the layer numbers of the graphene layer. **Figure 2.6** shows a typical example of the OM images of graphene flakes on 300-nm SiO_2-on-Si wafer, where we can clearly observe the morphology and size of the graphene flakes, and further distinguish the layer numbers of the different flakes from their color contrast difference.[77] In addition, sub-monolayer graphene (not a continuous film) on Cu can also be directly visualized after a thermal treatment (180 ℃ at a hot plate for around 10 minutes) of the graphene/Cu sample in air.[78] The thermal annealing process can transform the naked Cu to Cu oxides while keeping graphene-covered Cu intact, resulting in an interference color contrast between Cu oxide and Cu, which thus makes graphene easily visible under optical microscope. In our experiment, optical microscopy (Zeiss, AxioCam MRc5) is used to check the cleanness and layer number of the transferred graphene on 300-nm SiO_2-on Si wafer.

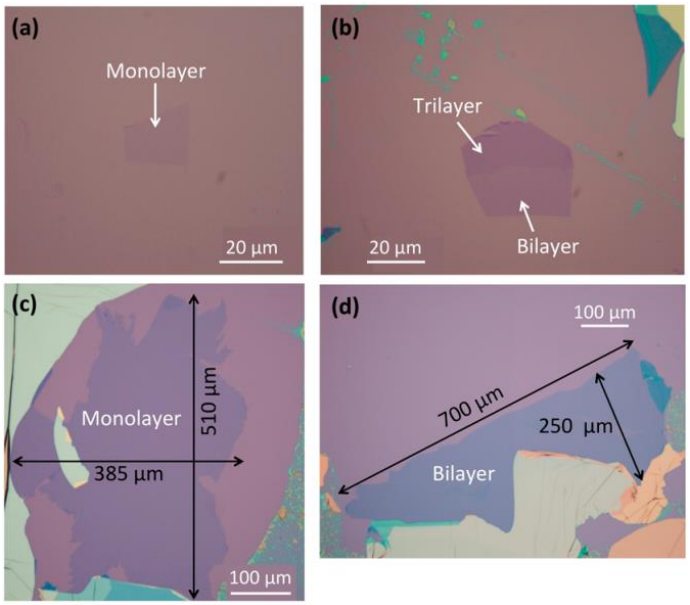

Figure 2.6. Optical images of the graphene flakes (different layer numbers) prepared by the mechanical exfoliation method.[77]

2.3.2 Scanning electron microscopy (SEM)

SEM can also be used to characterize the morphology, size, coverage and even layer numbers of the graphene. As compared to optical microscopy, the graphene layer can be directly visualized on the

metal substrate without any graphene transfer process. In the SEM image shown below (**Figure 2.7**),[79] we can clearly see the steps on the metal surface after the CVD growth process, and wrinkles on graphene (formed due to the different thermal expansion coefficients of graphene and the metal substrate). The "wrinkle" morphology is a typical feature of graphene prepared by CVD on metal substrates. Bilayer or multilayer graphene domains can also be distinguished from the SEM images due to their darker contrast.

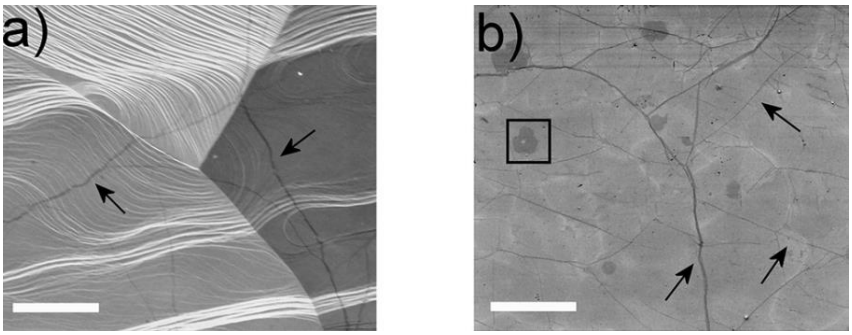

Figure 2.7. SEM images of graphene grown on a polycrystalline Cu substrate.[79] Arrows indicate the graphene wrinkles and the boxed region shows the bilayer (adlayer) graphene domain.

2.3.3 Low-energy electron microscopy (LEEM)

Low energy electron microscopy (LEEM) is a powerful technique for the investigation of surfaces, thin films and surface supported nanostructures and is widely used in the study of graphene.[80] LEEM images surfaces with elastically backscattered low energy electrons. For crystalline samples, which are usually studied with LEEM, elastic electron scattering is accompanied by diffraction from the crystal lattice. Sutter and co-workers used in-situ LEEM to observe epitaxial graphene growth on Ru(0001).[59] The *in-situ* LEEM images showed a fast expansion of growing graphene domains parallel to substrate steps and across steps in the 'downhill' direction (Figure 2.8).

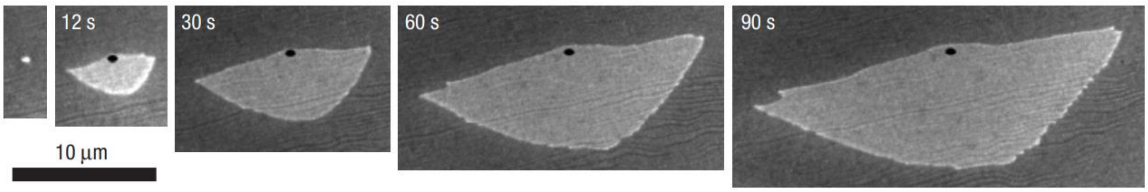

Figure 2.8. Time-lapse sequence of LEEM images showing the initial growth of graphene island on Ru(0001).[59] Black dots mark the position of the initial graphene nucleus.

2.3.4 Transmission electron microscopy (TEM)

Transmission electron microscopy (TEM) is a direct method to visualize graphene on the atomic level and the corresponding electron diffraction patterns can be used to study the layer number and stacking order of bilayer and/or multilayer graphene. Cross-sectional TEM images can clearly indicate the layer numbers of the as-prepared graphene and low-magnification TEM images can be used to assess

the uniformity and cleanness of the transferred graphene. **Figure 2.9** shows the HRTEM images and the corresponding selected area electron diffraction (SAED) patterns of bilayer graphene with different stacking order.[81] The bilayer graphene in panels a and b clearly shows Moiré patterns indicating twisted bilayer graphene; this is further verified by the two sets of diffraction spots in the SAED pattern. However, the AB-stacked bilayer graphene does not show any Moiré pattern with only one set of diffraction spots. The atomic structure of the graphene lattice, vacancy defects, and even grain boundaries in the graphene lattice can be clearly observed in the HRTEM images, which are crucial aspects for the study of graphene structures.

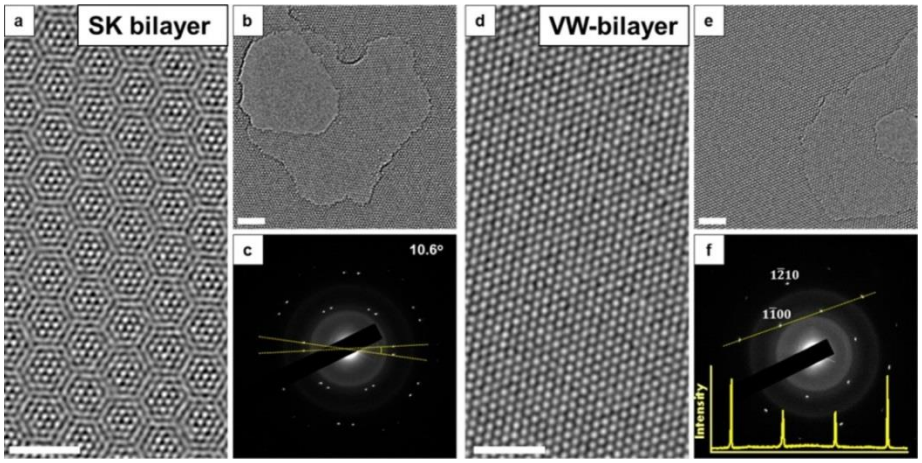

Figure 2.9. HRTEM and SAED characterization of Stranski–Krastanov (SK)-like and Volmer–Weber (VW)-like grown bilayer graphene.[81]

2.3.5 Atomic force microscopy (AFM)

Atomic force microscopy (AFM) is a type of scanning probe microscopy (SPM), with a very high resolution (of the order of fractions of a nanometer) can be achieved. AFM is a very useful tool to determine the thickness of the as-prepared graphene and investigate its surface roughness and cleanness. **Figure 2.10c** shows a typical AFM scanning image of a transferred graphene film on SiO_2/Si wafer.[74] The transferred graphene film is uniform and free of residue. The thickness of the monolayer region was measured to be around 1 nm, suggesting a highly conformal contact between the graphene and the substrate.

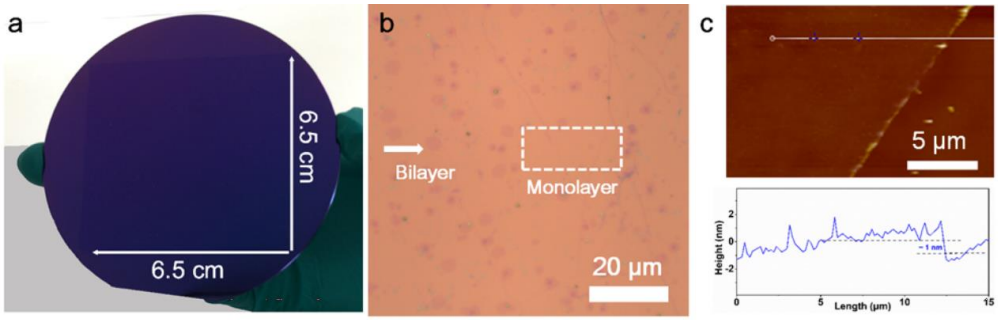

Figure 2.10. Optical image and AFM measurement of monolayer graphene film.[74]

2.3.6 Raman spectroscopy

Raman spectroscopy is one of the vibrational spectroscopic techniques used to provide information on phonons in crystals. This technique uses a laser light source to irradiate a sample and generates a small amount of inelastically scattered light, which is detected as a Raman spectrum using a CCD camera. Raman spectroscopy has been widely used in the study of the different allotropes of carbon (such as diamond, carbon nanotubes, fullerenes, etc.) where the different forms differ in phonon frequency due to their different crystalline structure.[82] With the development of graphene, Raman spectroscopy has also been applied as a fast, non-destructive means to determine the quality and layer thickness of graphene thin films. The main features in the typical Raman spectra of graphene-related materials are the D, G and 2D bands (second order of D band). The D band is known as the disorder band or the defect band which is not visible in pristine graphene because of crystal symmetries. In order for a D peak to occur, a charge carrier must be excited and inelastically scattered by a phonon, then a second elastic scattering by a defect or zone boundary must occur to result in recombination.. The D peak intensity can be used to analyze the defect density in graphene materials for the evaluation of graphene quality (for example, a perfect graphene sample has no D peak). The G band always appears around 1585 cm^{-1} and is an in-plane vibrational mode involving sp^2 hybridized carbon atoms that comprise the graphene sheet. The 2D band is the second order of the D band and results from a two-phonon scattering process, but unlike the D band, it does not need to be activated by proximity to a defect. The features (including position, peak width and intensity) of the 2D band can be used to analyze the thickness of the as-prepared graphene. **Figure 2.11a** shows the Raman spectra of graphene with different layer numbers ranging from monolayer to five-layer, along with that of graphite (HOPG).[83] There is a clear change of the 2D/G intensity ratio, 2D peak position and the peak width of the 2D peak with increasing layer number of graphene. **Figure 2.11b** shows the peak fitting results of the 2D band, from which we can determine the layer numbers of the as-prepared graphene.[84]

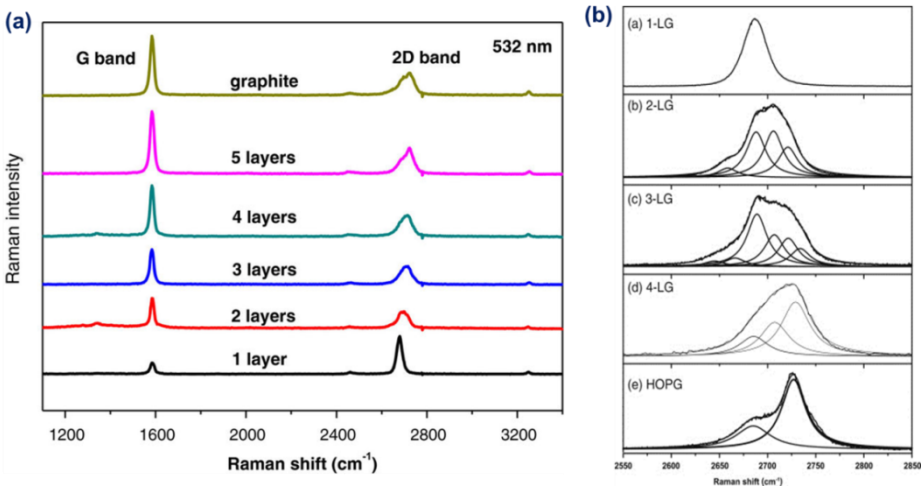

Figure 2.11. Raman spectra of graphene with different layer numbers (a) and the corresponding Raman peak fitting of the 2D peak (b).[83-84]

Chapter 3 CVD growth of highly-oriented monolayer graphene on Cu/Ni(111) foil

3.1 Background research and motivation

In this chapter, we will first present the background of the preparation of high quality graphene film and then demonstrate our strategy to further achieve large area highly-oriented monolayer graphene film by using our home-made Cu/Ni(111) foil.

Several approaches such as mechanical exfoliation of graphite,[77] epitaxial growth on SiC substrates,[85] and chemical vapor deposition (CVD) have been used to obtain monolayer graphene. [41, 55] Among these methods, CVD is currently the most effective approach to achieving large-area graphene films.[86] However, graphene grain boundaries (GBs) are formed during CVD growth when laterally misaligned graphene islands coalesce, which influence both the physical and chemical properties of the film.[87] The synthesis of a large-area graphene film with minimal GBs is an exciting scientific challenge that also has ramifications for mechanical, optical, and electronic applications.

Two approaches have been reported for the synthesis of large-area single-crystal-like graphene. The first ("slow method") is to decrease the number of nucleation centers and to promote growth of the islands so that larger islands are obtained. Using this approach, the growth of millimeter-to-centimeter-size single-crystal graphene islands in a few hours or longer (over a day) on Cu and Cu/Ni have been reported.[53, 88-90] The other approach ("fast method") is to control the orientation of graphene islands on a suitable substrate (for example, single crystal Cu(111) foil) and to join aligned islands to form large graphene crystals whereby, the formation of GBs at the 'stitching regions' can be avoided.[59, 91-92] This approach appears to be suitable to meet the demands of large-area graphene growth for application. The joining of aligned hexagonal graphene islands to achieve monocrystalline graphene has been reported on Cu(111) foils with hexagonal symmetry and having a small lattice mismatch with respect to graphene (the value is reported to be about 3–4% at room temperature).[93-94] Here, it is noted that previous reports by surface scientists have confirmed[95-97] that pure Cu has zero catalytic activity for the decomposition of methane, whereas Ni has a relatively strong catalytic activity and high melting point (1455 ℃) for "activating" methane and other hydrocarbons to yield, e.g., radical species at high temperature.[46, 51, 98]

Since Cu and Ni have the FCC crystal structure and show complete solid solubility, we have here revisited our previous notion that a Cu/Ni alloy could be a good substrate for controlled graphene growth by changing the Ni content in the alloy (using '70/30' and '90/10' commercial Cu/Ni alloy foils for graphene growth)[99-100]. Given our capability to convert a polycrystalline Cu foil to a single crystal Cu(111) foil over large areas, we decided to expand our studies to find out if Cu/Ni(111) alloy foils could also be made with fine control of the Ni content; we have found that this can be achieved, as described herein. Recent studies have demonstrated that Ni doped in Cu/Ni alloy not only

maintains its own catalytic activity, but also improves the activity of neighboring surface Cu atoms during CH_4 dissociation, thus leading to a higher growth rate of graphene.[90, 101-103] However, merging aligned graphene islands into a continuous monolayer graphene layer on Cu/Ni(111) foil has never been investigated. Here, we provide compelling evidence that the continuous single layer film so obtained, is one large single crystal or very close thereto.

We report the preparation of large area single crystal Cu/Ni(111) alloy foils and their use for the fast growth of highly-oriented monolayer graphene films. We discovered using low energy electron diffraction (LEED) that the surface of the Cu/Ni(111) foil does not have a random distribution of Ni, but instead has a superstructure with the composition Cu_6Ni_1, whether coated with a monolayer of graphene or not. We have therefore modeled the catalytic activity of a surface with this stoichiometry using density functional theory (DFT) and compared it to that of a Cu(111) surface, specifically for the reaction of methane on the surface. The Cu_6Ni_1 surface superstructure is present at least in the composition range from 1.3 to 7.8 bulk at.% of Ni, which we have verified experimentally by preparing and measuring LEED on foils with different bulk atomic percentages of Ni precisely controlled to 1.3, 2.4, 3.9, 5.9, 6.2, and 7.8 at.% Ni. The Cu/Ni(111) alloy foil substrates allow growth of highly aligned hexagonal graphene islands on their surface. Full coverage of highly-oriented monolayer graphene on the entire substrate is achieved in 5 min by joining the aligned graphene islands (hexagonal islands almost all having the same orientation; that is, their growth is epitaxial, as shown below). Our studies of the kinetics of island growth on the Cu(111) and Cu/Ni(111) surfaces under identical growth conditions show that the activation energy is significantly lower for this Cu/Ni(111) surface, and these experimental results are supported by DFT modeling. The crystallinity and the 'quality' of the large-area monolayer graphene film were investigated by: Raman spectroscopy, polarized optical microscopy (POM) on a spin-cast nematic liquid crystal (NLC) layer, hydrogen etching, low-energy electron diffraction (LEED), aberration-corrected high-resolution transmission electron microscopy (HRTEM) and selected area electron diffraction (SAED), and SEM. For the continuous monolayer films, an array of essentially parallel folds roughly 40 nm wide (widths range from 10 nm to 300 nm) and 3-layers in height was found by SEM and AFM with each fold oriented perpendicular to step edges on the substrate and roughly separated by 20 μm; the fold regions comprise roughly 0.4 percent of the essentially single crystal surface. Finally, we present a detailed investigation on the merging of the graphene islands using HRTEM and ambient STM on samples obtained by deliberately arresting the growth prior to full coverage.

3.2 Experimental section

3.2.1 Preparation of Cu/Ni(111) foil

A 2 cm × 8 cm Cu foil (80 μm, 99.9%, Nilaco Co., Japan) was heated at 1050 ℃ with 10 sccm Ar and 10 sccm H_2 at atmospheric pressure (1 atm) for 12 h to convert it to a Cu(111) foil. Ni layers were

then plated on the Cu(111) foil in an electrolytic solution, which was prepared by dissolving 140 g of $NiSO_4$ $6H_2O$, 4 g of $NiCl_2$ $6H_2O$, 2 g of NaF and 15 g of H_3BO_3 in 500 mL of deionized water. The current density in all the plating experiments was 0.02 A cm^{-2}. After washing and drying, the Ni-plated Cu(111) foils were placed in a quartz furnace and heated at 1050 ℃ for 4-6 h in a gas flow of Ar (20 sccm) and H_2 (20 sccm) at atmospheric pressure.

3.2.2 CVD growth of graphene on Cu/Ni(111) alloy

Before graphene growth, the Cu/Ni(111) alloy foils were immersed in acetic acid (CH_3COOH) for 20 min so as to remove the native oxide layer. After drying by blowing with N_2 gas, the substrates were immediately loaded into the CVD chamber for growth. In a typical graphene growth process, the CVD chamber was purged twice with pure Argon gas, after which, the alloy foils were heated from room temperature to 1075 ℃ during 1 h in a gas flow of Ar (500–1000 sccm) and H_2 (50–100 sccm), held for another 1 h at 1075 ℃, and 1% CH_4 diluted in Ar (a pre-made gas mixture) was then introduced into the chamber. During the growth process, the temperature was thus fixed at 1075 ℃, and the total pressure at 1 atm. Finally, the graphene/substrate was rapidly cooled to room temperature (a typical temperature profile is shown in **Figure 3.1**).

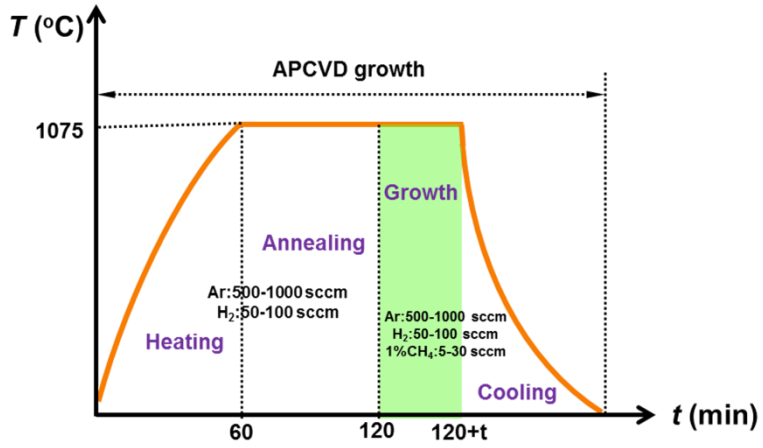

Figure 3.1. Temperature-time profile for the CVD growth of monolayer graphene.

3.2.3 Low energy electron diffraction (LEED) measurement

Observations using Low energy electron diffraction (LEED) provided evidence of long-range crystallinity and the absence of rotational disorder. To study the long-range crystallinity and the orientation of the hexagonal lattice of graphene, we measured LEED for the Cu/Ni(111) foil without graphene, and for graphene on the Cu/Ni(111) foils, with an electron beam energy of 20–200 eV. LEED patterns were recorded at a pressure of ~1 × 10^{-10} Torr in a chamber equipped with LEED optics (SPECTRALEED, Omicron NanoTechnology GmbH). The Cu/Ni(111) foil samples (without graphene) were loaded into the LEED chamber, and annealed at 400 ℃ (200 ℃ for the graphene-

coated Cu/Ni(111) alloy foil samples) overnight in ultrahigh vacuum. The LEED measurement was conducted at room temperature on a sample with a typical size of 1 cm × 1 cm.

3.2.4 Raman spectroscopy of the as-grown graphene and study of isotope-labelled growth

Prior to Raman spectroscopic measurements, the graphene samples were transferred onto a 300-nm SiO_2-on-Si wafer. Raman spectroscopy and mapping were performed using Ar^+ laser excitation (wavelength of 532 nm) with 1 mW power. The accumulation time for each spectrum was 0.5 s for image scanning and 1 s for a single spectrum. Raman mapping was conducted on both sub-monolayer graphene and continuous monolayer graphene film samples at many locations on the samples.

To further investigate the mechanism of growth of graphene on our Cu/Ni(111) foils, we used the carbon isotope labeling technique together with Raman spectroscopy. The isotope distribution (^{13}C and ^{12}C) in the local graphene regions reflects the dosing sequence used and can be mapped according to the different Raman mode frequencies of ^{13}C- and ^{12}C-labeled graphene. A flow of $^{13}CH_4$ was first used to form graphene nuclei and thus islands at an early stage of growth, and the gas was then switched to normal methane ($^{12}CH_4$) gas. After growth, the graphene was transferred onto a SiO_2-on-Si substrate and Raman mapping was done. We mapped the 2D peak position to distinguish the distribution of ^{13}C and ^{12}C species (the 2D peak at 2580 cm^{-1} represents the signal from pure ^{13}C-labeled graphene and that at 2680 cm^{-1} the signal from normal graphene, i.e., predominantly ^{12}C).

3.2.5 Polarizing Optical Microscopy (POM) measurements

For POM (Nikon LV100-POL) measurements, the graphene samples were first transferred by the bubbling transfer method18–20 onto 300-nm SiO_2-on-Si substrates for measurements in the reflection mode and onto glass substrates for measurement in the transmission mode. 4-pentyl-4-cyanobiphenyl (5CB; Sigma Aldrich) was then spin-coated on the surface of the transferred samples at 8000 rpm for 60 s. During the measurements, the polarizer was fixed while the analyzer was rotated from 0 °to 180 °.

3.2.6 Graphene transfer and reusing the Cu/Ni(111) foils to grow graphene

After CVD growth, the graphene was transferred onto target substrates (300-nm SiO_2-on-Si) using the electrochemical delamination (‘bubbling’) method, both for Raman characterization and for fabricating electrical devices. Prior to transfer, the graphene was spin-coated with a polymethyl methacrylate (PMMA) layer at 3000 rpm for 1 min to provide mechanical support to the film during transfer. The PMMA/graphene/Cu-Ni(111) alloy foil/graphene/PMMA stack was then dipped into aqueous NaOH solution (1M) to act as the cathode in an electrolysis cell with a constant current supply. The PMMA/graphene layer detached from the Cu/Ni(111) foil after tens of seconds due to the formation of a large number of H_2 bubbles at the interface between the graphene and the Cu/Ni(111) foil. After cleaning with deionized water, the floating PMMA/graphene layer was transferred to the

target substrate. Finally, the sample was dried and the PMMA was dissolved in acetone. The transfer process is illustrated in **Figure 3.2**.

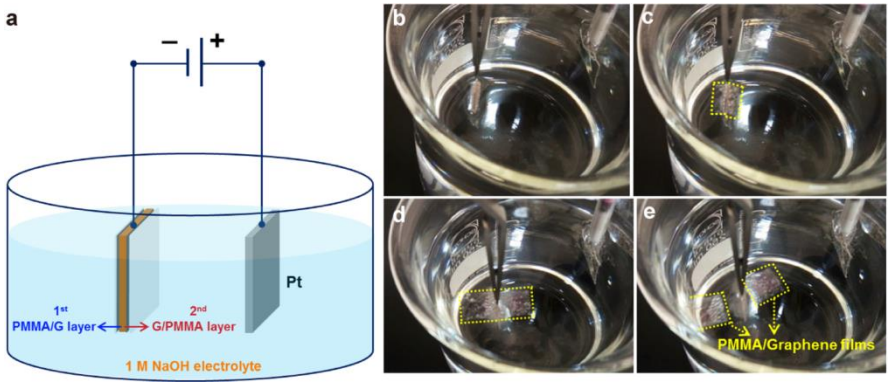

Figure 3.2. Electrochemical delamination of graphene from the Cu/Ni(111) foil. (a) Schematic of the transfer process for graphene. (b–e) Photographs show the transfer process.

3.2.7 Transmission electron microscopy (TEM) and selected area electron diffraction (SAED)

TEM was performed on graphene islands and on continuous monolayer graphene films. The graphene sample was transferred by the bubbling method (as described in the section on graphene transfer) onto a copper Quantifoil TEM grid with 1.2 μm diameter holes. Before TEM characterization, the sample was annealed at 150 ℃ in high vacuum (10^{-6} Torr) for 12 h to remove any residue introduced during transfer. HRTEM images and the corresponding SAED patterns were obtained on an aberration-corrected TEM (FEI Titan^3 G2 60–300) with an acceleration voltage of 80 kV to determine the graphene crystal orientation at various locations across the 3-mm diameter sample. DF-TEM images were obtained by selecting one of the second-order diffraction spots in the SAED pattern with a 1.28 nm^{-1} diameter objective aperture.

3.2.8 Scanning Tunneling Microscopy (STM)

Scanning Tunneling Microscopy (STM) was performed under ambient conditions at room temperature with a Nanoscope IIIa multimode SPM (Digital Instruments). The STM tip was a tungsten wire prepared by electrochemical etching and annealed by electron beam heating.

3.2.9 Optical transmittance and sheet resistance of the graphene film

The optical transmittance of the monolayer graphene film was measured by detecting the light transmitted through a circular hole with a diameter of 5.3 mm (Cary Series UV-vis-NIR spectrophotometer; Agilent Technologies) after transferring it onto a glass substrate. The sheet resistance was measured on five transferred monolayer graphene samples (1 cm × 1 cm) using a surface resistivity measurement system (AIT Co., Ltd., CMT-2000N, Seoul, Korea) with a four-point-probe head unit.

3.2.10 Device fabrication and mobility measurements

A field effect transistor (often referred to as a "G-FET") device with graphene as the active region was fabricated by transferring the monolayer graphene and joined islands samples onto a 300-nm SiO_2-on-Si substrate, followed by deposition of source and drain electrodes (Cr/Au; 5 nm/50 nm) by electron beam evaporation. Electron beam lithography was used to define and pattern the graphene to form a field-effect transistor. Oxygen plasma was used to etch away the unwanted graphene region. The back-gated graphene field-effect transistor (GFET) obtained was characterized at room temperature. The mobility was calculated using the following equation:

$$\mu = \frac{\mathrm{d}I_d}{\mathrm{dV}_g}\frac{L}{WC_gV_d}$$

where I_d is the source drain current, V_d is the source drain voltage, V_g is the gate voltage, L and W are the channel length and width, respectively, and C_g (11 nF cm^{-2}) is the capacitance of the back-gate dielectric layer.

3.2.11 Density Functional Theory calculations

In the calculation of the energy barriers relevant to CH_4 decomposition, the Cu/Ni(111) surfaces were simulated by a 3-layer-thick slab model with a Cu(111) surface. Each layer had 28 Cu atoms, while on the top layer, four Cu atoms were substituted by Ni atoms (one in the center and the other three at the corners) to simulate the Ni:Cu composition (1:6) used in the experiment (LEED patterns). To avoid periodic image interaction, all slabs were separated by a vacuum layer of 10 Å. During both structure optimization and calculation of the energy barriers, the bottom layer of the slab was fixed while all the other metal atoms were fully relaxed. To further study the influence of superstructure (on Cu/Ni(111) surface) on the growth of highly-oriented graphene, we have performed density functional theory (DFT) calculations within the method of Tkatchenko and Scheffler (DFT-TS).[104] All the density functional theory (DFT) calculations were carried out with the Vienna ab initio Simulation Package (VASP).[105-106] The projected augmented wave (PAW)[107] pseudopotential was employed to describe the interactions between valence electrons and the ion cores. The generalized gradient approximation (GGA) parametrized by Perdew et al. (PW91)[108] was adopted as the exchange-correlation functional. To introduce a weak van der Waals interaction into the system, the DFT-D2 method was used.[109] The Brillouin zone was sampled using a 3×3×1 Monkhorst–Pack mesh k-point[110] and a plane-wave cutoff energy of 400 eV was employed. The energy barriers and minimum energy paths (MEP) were explored with the climbing image nudged elastic band (CI-NEB) method[111] proposed by Jonsson and Henkelman. All the structure relaxations were conducted with energy and force convergence criteria of 10^{-4} eV and 10^{-2} eV/Å.

3.3 CVD growth and characterization of graphene on Cu/Ni(111) foils

3.3.1 Preparation and characterization of Cu/Ni(111) foils

A typical process for the preparation of a Cu/Ni(111) foil and graphene growth on this foil is depicted in **Figure 3.3**. The process consists of electroplating a desired amount of Ni on both sides of the Cu(111) foil, heat-treatment of the Ni-plated Cu(111) substrate to obtain Cu/Ni(111), growth of aligned graphene islands, and the formation of a continuous graphene film. **Figure 3.4** shows SEM images of the surfaces of the Cu(111), Ni-plated Cu(111), and Cu/Ni(111) foils, where we can clearly see the surface morphologies and roughness. The XRD patterns shown in **Figure 3.5a** indicate that both the Cu foil and the as-prepared Cu/Ni(111) foils are exclusively (111) oriented. The single peak observed for the Cu/Ni alloy foil indicates complete mixing of the two metals during annealing, further confirming the transformation of Ni-plated Cu(111) to Cu/Ni(111) alloy. EBSD mapping (**Figure 3.5b** and **c**) shows (111) orientation of both the Cu foil and the Cu/Ni(111) foil. AFM measurement (**Figure 3.5c** and **d**) indicates a very flat surface of both the Cu(111) and Cu/Ni(111) foils.

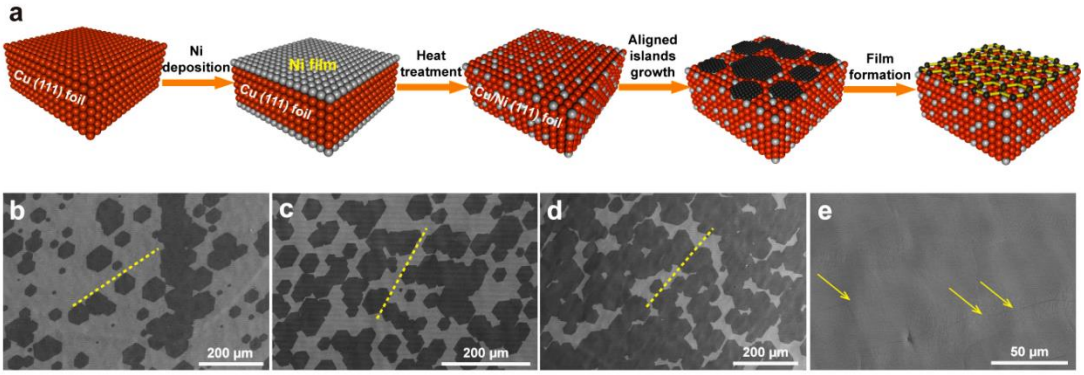

Figure 3.3. Making the Cu/Ni(111) alloy foil and the typical growth of highly-oriented single-layer graphene. (a) Schematic of CVD growth of highly-oriented graphene formed by the joining graphene islands with the same orientation. (b–e) Typical SEM images of graphene grown on Cu/Ni(111) alloy foils (5.9 at.% Ni) for 1, 2, 3, and 5 min, respectively. The dotted lines in b–d indicate the alignment of the hexagonal islands. The arrows in (e) show folds in the continuous single-layer graphene.

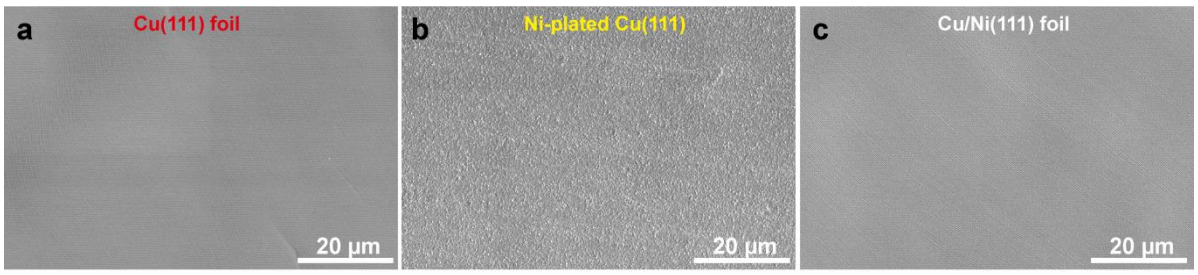

Figure 3.4. Preparation of Cu/Ni(111) alloy foils. (a–c) SEM images of Cu(111), Ni-plated Cu(111) and Cu/Ni(111) foils.

XPS depth-profile measurements showed that the bulk composition was uniform, further confirming that Cu and Ni were well mixed in the alloy (**Figure 3.6**). The top atomic layer(s) have a different composition and have an ordered structure of Cu and Ni atoms rather than randomly substituted Ni (Cu_6Ni_1; see discussion of LEED results below). **Figure 3.3b-e** show scanning electron microscopy (SEM) images of the graphene grown at 1075 ℃ on Cu/Ni(111) alloy substrates (growth conditions given in **Figure 3.1**). It can be seen that the graphene first nucleates and then grows into islands that (almost) all have the same orientation across the imaged area (~800 μm; **Figure 3.3b-d**) and, that upon extended growth time, eventually coalesce into a continuous film. All the graphene islands are hexagonal with sizes in the range 50–100 μm after 1 min exposure to methane/hydrogen gas mixture. Like the islands, the continuous graphene film was identically oriented in almost all regions. We have found between 1 to 2% mis-oriented graphene islands in different samples (the OM image of a typical sample is given in **Figure 3.7**).

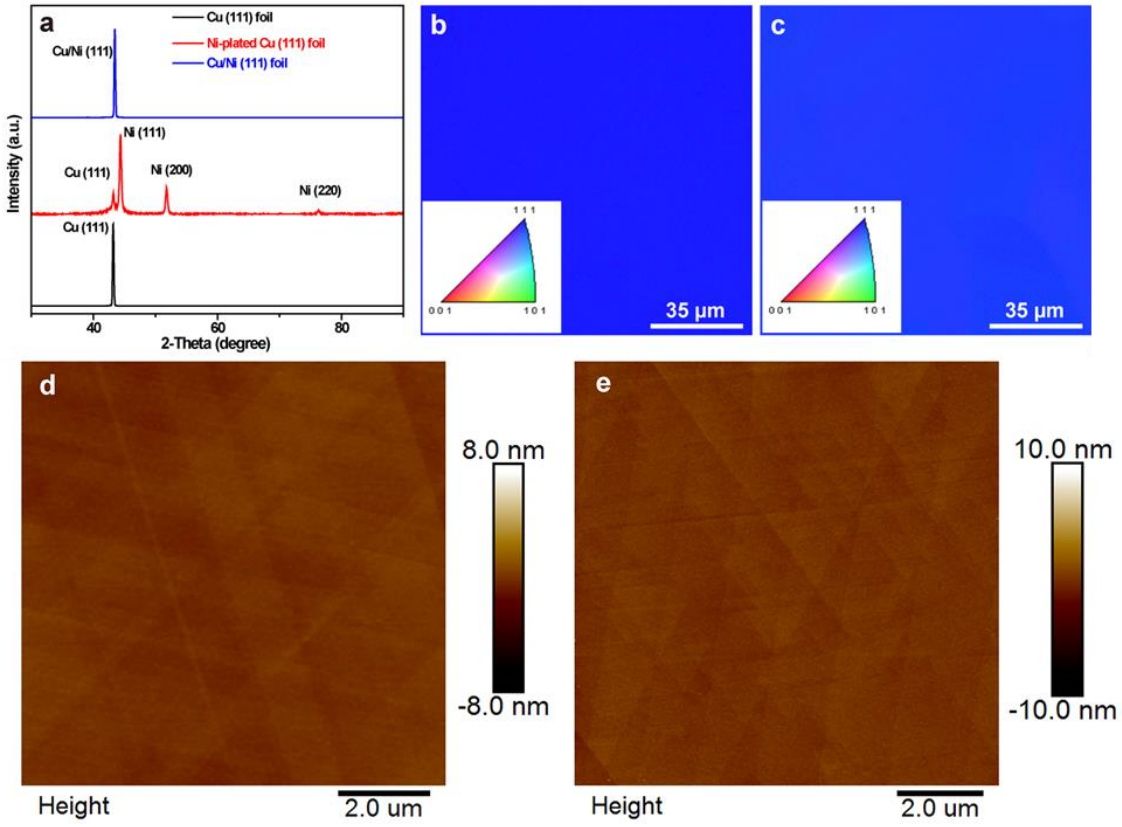

Figure 3.5. Characterization of Cu(111) and Cu/Ni(111) foils. (a) XRD patterns of pure Cu(111), Ni-plated Cu(111) and Cu/Ni(111) alloy foils. (b, c) EBSD of Cu(111) and Cu/Ni(111) alloy foils, respectively. (d) AFM image of Cu(111) foil (surface roughness is 0.82 nm after polishing). (e) AFM image of Cu/Ni(111) alloy foil (surface roughness is 1.25 nm after polishing).

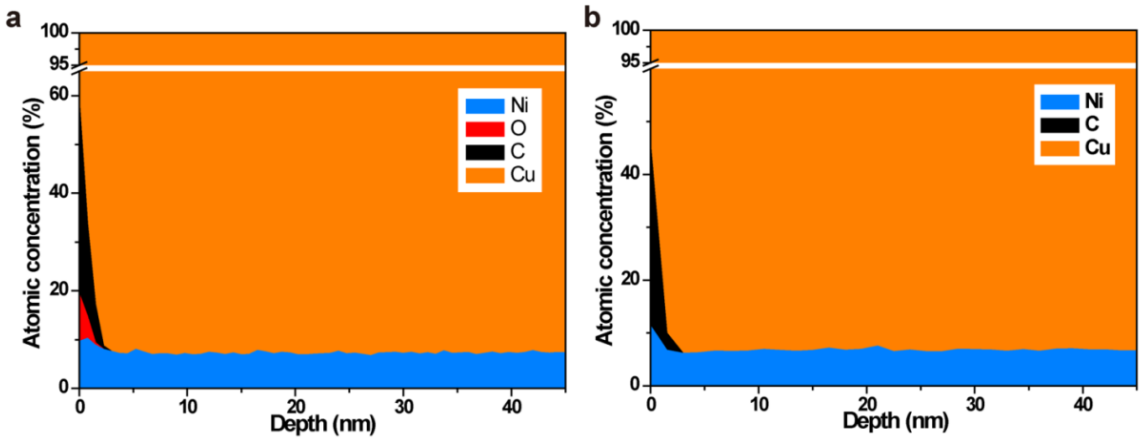

Figure 3.6. XPS depth profile measurements. (a) Cu/Ni(111) alloy foil. (b) Monolayer graphene on Cu/Ni(111) alloy foil.

In addition to transferred samples, we have also analyzed several SEM images of the as-grown graphene islands on the Cu/Ni(111) substrate and found that the misorientation angle is essentially random (ranging from greater than 0 to less than 30 °) with respect to the aligned islands. This broad range of misorientation angles in misoriented graphene islands has been previously observed for graphene grown on Cu(111).[94] Thus, a large majority of the islands are epitaxial with the substrate and closely aligned with each other (marked with yellow dashed lines in **Figure 3.7**). Full coverage of the highly-oriented monolayer graphene film can be achieved in 5 min, which is much shorter than the growth time reported in previous studies.[91, 94, 112-113]

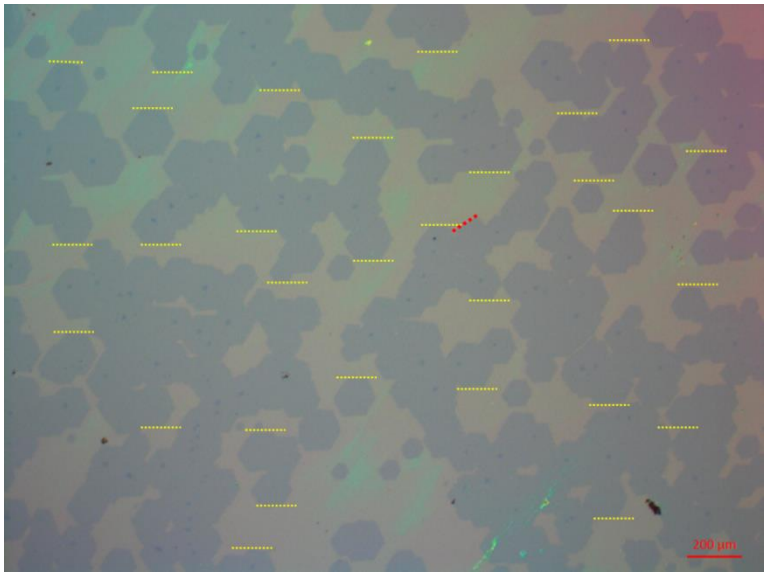

Figure 3.7. Optical image of a transferred graphene island sample on SiO_2-on-Si substrate. The yellow dashed lines indicate the direction of oriented graphene islands. The red dashed line shows one mis-oriented island.

Figure 3.8a shows a photograph of the Cu/Ni(111) alloy foil and we note its mirror-like surface; **Figure 3.8b** shows a SEM image of the same foil. The uniform color of the EBSD maps (**Figure 3.8c**–**d**) for the out-of-plane (z) and in-plane (rolling direction) (y) maps indicates that the Cu/Ni(111) alloy foil is a single crystal over a large area (about 2 cm × 3.5 cm). Combined data from XRD and EBSD analysis prove that the whole Cu/Ni alloy foil is a single crystal. The LEED pattern of the Cu/Ni(111) alloy foil obtained at 75 eV (the spot size is approximately 1 mm) has two sets of hexagonal patterns (**Figure 3.8e**). These two sets of satellite LEED spots (see detailed analysis in **Figure 3.9**) indicate the formation of (√7×√7)R19.1º and (√7×√7)R-19.1 ºsuperstructures (they have the same periodicity but different chiral angles). The models of the superstructures in **Figure 3.9c-d** show that the Ni atoms are periodically arranged on the surface; the atomic ratio of Cu and Ni is 6:1 from the unit cell shown in **Figure 3.9e**, corresponding to a Ni percentage of 14.3 at.% at the surface. This result indicates that the surface is Ni-rich relative to the bulk, and we note other studies where, for Cu-rich Cu/Ni alloys, Ni was reported to segregate to the alloy surface.[114-116] More interestingly, we find that the same superstructure was detected by LEED with or without graphene grown on the surface, for the bulk composition of 5.9 at.% Ni (for 1.3, 2.4, 3.9, 6.2, and 7.8 (bulk) at.% Ni, an identical superstructure was found for the graphene-coated samples; we did not study if it was present prior to graphene growth for these compositions).

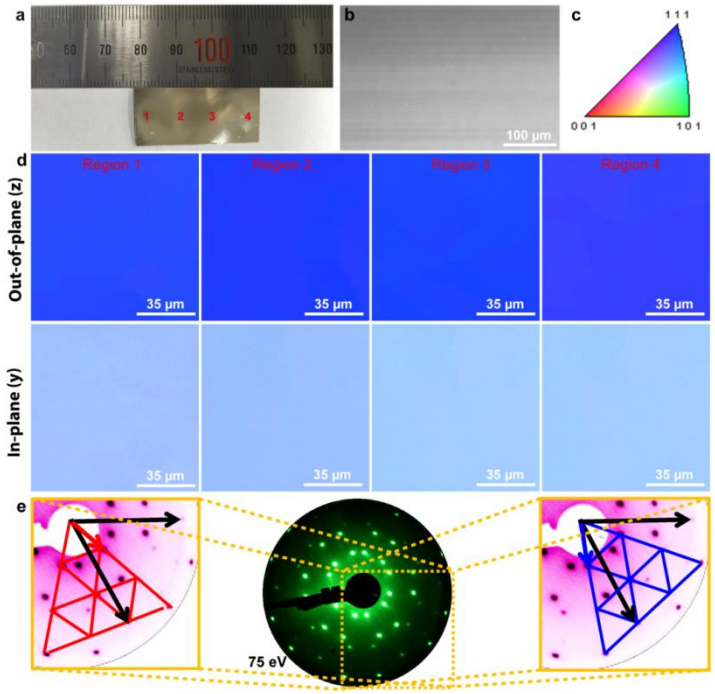

Figure 3.8. Characterization of Cu/Ni(111) alloy foils. (a) Optical image of a Cu/Ni(111) alloy foil (5.9 at.% Ni). (b) SEM image of the Cu/Ni(111) alloy foil. (c) Inverse pole figure orientation coloring scheme of the EBSD maps. (d) EBSD maps taken over four 100×100 μm^2 areas across a 2 cm × 3.5 cm Cu/Ni foil. Out-of-plane (z) data represent the surface orientation, while the in-plane (y) measurements indicate the azimuthal angle. (e) LEED measurement of the Cu/Ni(111) alloy foil.

To the best of our knowledge, such single crystal Cu/Ni(111) foils, and also the superstructure of Ni in the Cu lattice in the top atomic layer(s) in a Cu/Ni(111) crystal (surface is Ni-rich) has never been reported. The exceptionally fast growth of epitaxial graphene on a metal foil surface motivated us (see below) to study the kinetics of growth of the graphene islands.

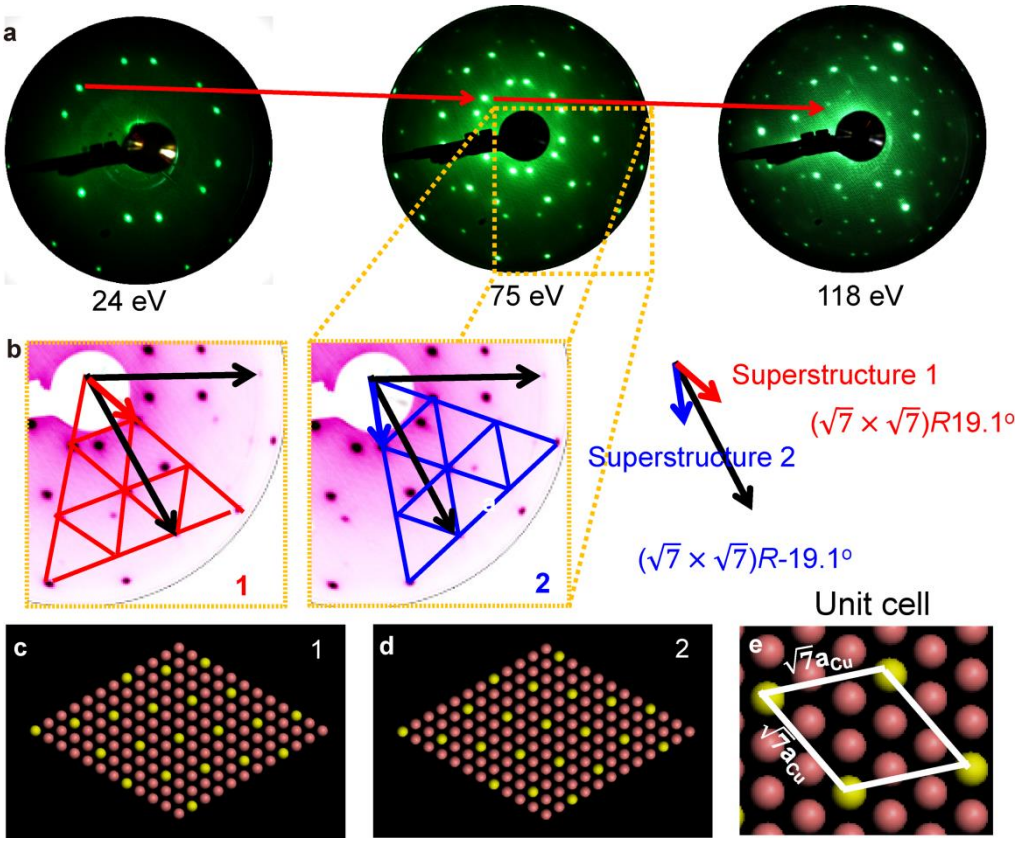

Figure 3.9. LEED investigations of the Cu/Ni(111) alloy. (a) LEED patterns of Cu/Ni(111) alloy (5.9 at.% Ni) at different incident energies. (b) Superstructure analysis from the LEED pattern taken at 75 eV. (c, d) Corresponding optimized models of (b). (e) The unit cell is illustrated with solid lines.

3.3.2 Growth, mechanism and characterization of graphene

The rate of nucleation and the growth rate of graphene islands on the Cu/Ni(111) foil can be controlled by adjusting the Ni concentration. **Figure 3.10a** shows the very high density of nucleation and subsequent growth of graphene islands with an average size of ~20 μm on a pure Cu(111) foil. **Figure 3.10b-f** show SEM images of graphene islands grown on Cu/Ni(111) alloy foils with 1.3, 2.4, 4.3, 5.9 and 8.6 at.% Ni in the bulk foil. A significant drop in nucleation density along with increase in island size is observed as the Ni content is increased, indicating increased growth rate of the graphene islands. A parametric study of the effect of the bulk Ni concentration on the nucleation density and graphene island size gives the results shown in **Figure 3.10g-h**. It is seen that the size of the hexagonal single-crystal graphene islands reaches ~350 μm (in 5 min; note that we chose growth conditions that allowed to study the island size rather than finding the conditions that allowed for

complete film growth in only 2–5 min) on the Cu/Ni(111) alloy foil with 5.9 at.% Ni (the surface is Cu_6Ni_1). The maximum growth rate of the islands for this Ni composition reached approximately 70 μm min^{-1} which is about 17 times that on pure Cu. For the alloy with 8.6 at.% Ni, the graphene island size was around 400 μm. We further measured the island size as a function of the growth temperature for Cu(111) and Cu/Ni(111) (5.9 at% Ni; this is the bulk concentration, while the surface composition is 14.3 at% Ni) foils under identical growth conditions, see **Figure 3.11**. The plot of the island size as a function of temperature fits well to the Arrhenius equation (for island growth on both the Cu/Ni(111) alloy and Cu(111) foils).

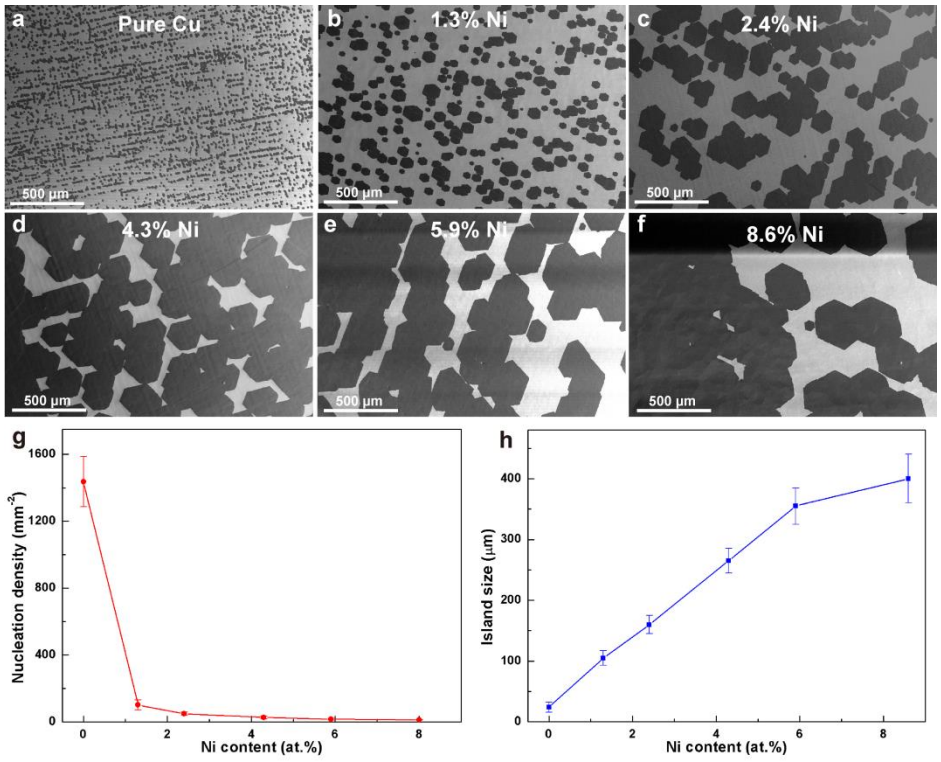

Figure 3.10. Effect of Ni concentration on the nucleation density and island size of the as-grown graphene. (a) SEM images of graphene islands on pure Cu(111). (b–f) SEM images of graphene islands grown on Cu/Ni(111) alloy foils with (b) 1.3 at.%, (c) 2.4 at.%, (d) 4.3 at.%, (e) 5.9 at.%, and (f) 8.6 at.% Ni at 1075 ℃. (g) Dependence of the nucleation density on Ni concentration. (h) Dependence of the graphene island size on Ni concentration.

The activation energy and the pre-exponential factor A can be obtained from the following equation.

$$k=A\exp(-E_a/k_BT) \qquad (1)$$

where k is the rate constant, A is the pre-exponential factor, E_a is the activation energy, k_B is the Boltzmann constant and T is the temperature in degree Kelvin. For an elementary reaction, A is the number of properly-oriented collisions per unit time. We note however, that graphene growth on a metal substrate consists of several reactions including the dissociation of carbon feedstock, diffusion of the precursor, the attachment of the carbon precursor to the edge of graphene islands, and the

corresponding reverse reactions. Thus, the graphene growth process cannot be considered as an elementary reaction, which means that A and E_a are functions of all the parameters of many different reactions.

For a *simplified* model of graphene growth, the growth rate of graphene on a catalyst surface can be written as:

$$R \sim \rho^{\alpha} * (k_B T/h) * P_{Att} \quad (2)$$

Where ρ is the concentration of the carbon precursor on the metal surface, h is the Planck constant. α =1, 2, or 5 depending on the smallest number of atoms in the carbon clusters that could be attached to the edge of graphene (that is, C_1, C_2, or C_5).[117-120]

$$P_{Att} \sim \exp(-E_b/k_B T) \quad (3)$$

P_{Att} is the probability of carbon species attachment for each try and E_b is the barrier to carbon species attachment. Under near thermal equilibrium condition,

$$\rho = \exp(-E_f/k_B T) \quad (4)$$

where E_f is the formation energy of the surface carbon precursor on the metal surface. Thus, the island growth rate can be roughly written as

$$R \sim \exp[-(\alpha E_f + E_b)/k_B T] \quad (5)$$

With R the rate of island growth and the calculated activation energy $E_a = \alpha E_f + E_b$. Depending on the way graphene growth actually proceeds, E_f ranges from 1.0 to 2.5 eV[121-122] according to if one assumes that α to be 1, 2 or 5. (The picture we briefly present here helps to understand the large range of E_a values reported in various prior works on the kinetics of graphene growth on a variety of metal substrates.)

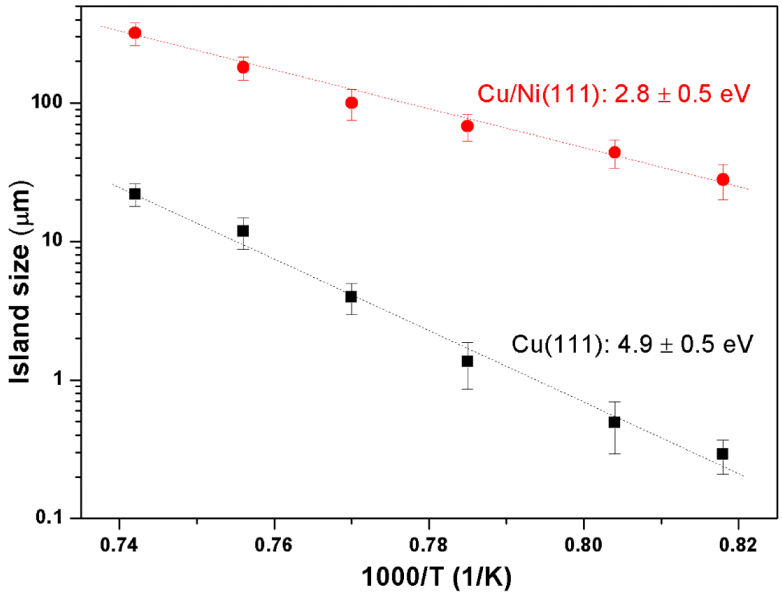

Figure 3.11. Arrhenius plot of island size as a function of inverse of the temperature for graphene growth on Cu(111) and Cu/Ni(111) (5.9 at.% Ni). Here, 5 sccm of 1% CH_4 (diluted in Ar) was used at different temperatures (1075, 1050, 1025, 1000, 970, and 950 ℃) for graphene growth.

For graphene growth on pure Cu(111), E_a is calculated from the fitted curve to be 4.9 ± 0.5 eV and the pre-exponential factor A_{Cu} is $10^{18.9\pm2.0}$ from Eqn. 1; for Cu/Ni(111), the E_a is 2.8 ± 0.5 eV and the pre-exponential factor $A_{Cu/Ni}$ is $10^{12.3\pm2.0}$. In other studies, the reported E_a values for graphene growth using Eqn. 1 range from 2.7–5.5 eV.[123-128] Both the E_a and A values for graphene growth on Cu(111) are significantly higher than those of graphene growth on Cu/Ni(111). The smaller E_a of graphene on Cu/Ni(111) surface might be due either to the lower formation energy of carbon precursors on the substrate, or the possible reduced barrier to incorporating carbon species onto the edge of graphene, or both. Further insight into the growth kinetics was obtained from DFT calculations. As shown in **Figure 3.12**, the energy barriers for sequential dehydrogenation of CH_4 on the Cu/Ni(111) surface are significantly lower than those on the Cu(111) surface and the reaction energies are also lower. For example, the energy barrier for decomposing a CH_4 molecule to a CH_3 radical on Cu(111) is 1.56 eV, whereas it is only 0.88 eV on the Cu/Ni(111) surface. The reduction of the energy barrier (by 0.68 eV) will greatly accelerate CH_4 dissociation on the Cu/Ni(111) surface, leading to a drastic increase of the concentration of CH_3 radicals. This will further increase the amount of CH_3, CH_2, and CH radicals to form more surface-active carbon species. The catalytic activity of a Cu/Ni(111) substrate is thus much higher than that of a Cu(111) surface.

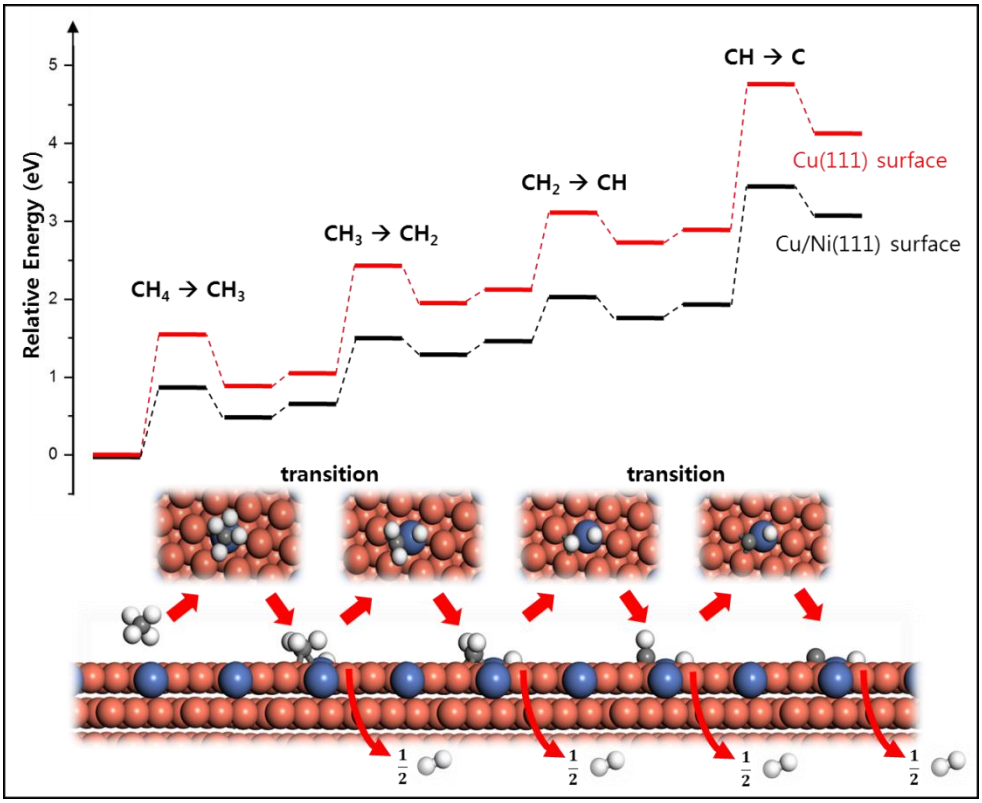

Figure 3.12. Dehydrogenation of a methane molecule on Cu(111) and Cu/Ni(111) surfaces and the associated transition states. Inset shows the transition states of CH_x radicals on the Cu/Ni(111) surface and the removal of H from the surface in the form of a H_2 molecule.

To further investigate the mechanism of growth of graphene on our Cu/Ni(111) foils, we used the carbon isotope labeling technique together with Raman spectroscopy. The isotope distribution (^{13}C and ^{12}C) in a graphene region depends on the dosing sequence used and can be precisely mapped due to the difference in the frequencies of the Raman modes of ^{13}C- and ^{12}C-labeled graphenes.[129-130] In our experiment, a flow of $^{13}CH_4$ was first used to form graphene nuclei and islands formed therefrom at an early stage of growth, and the reacting gas was then switched to normal methane ($^{12}CH_4$) gas. After growth, the graphene was transferred onto a SiO_2-on-Si substrate and Raman mapping was carried out. We mapped the 2D peak position to distinguish the distribution of ^{13}C and ^{12}C species (the 2D peak at 2580 cm^{-1} represents the signal from pure ^{13}C-labeled graphene and that at 2680 cm^{-1}, the signal from normal graphene, i.e., predominantly ^{12}C).

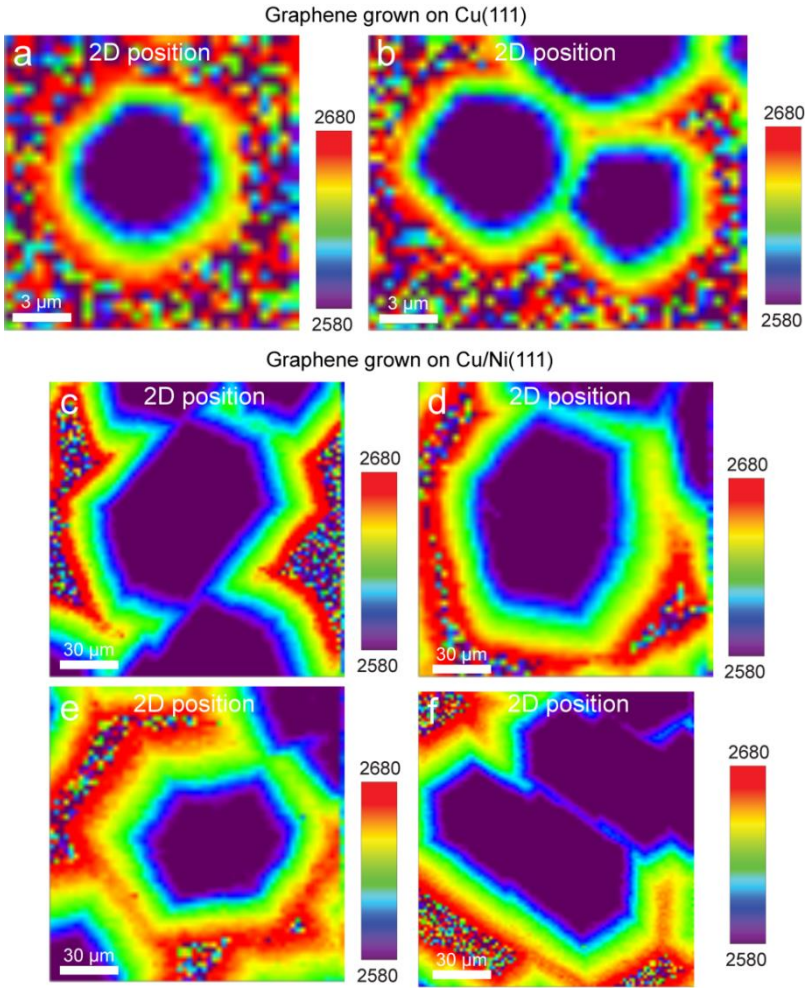

Figure 3.13. Raman mapping of $^{13}C/^{12}C$ labeled graphene (transferred onto 300-nm SiO_2-on-Si substrates) grown on Cu(111) and Cu/Ni(111) foils (5.9 at.% bulk Ni). (a, b) Raman maps of the 2D peak of transferred isotope-labeled graphene grown on Cu(111) foil. (c–f) Raman maps of the 2D peak of transferred isotope-labeled graphene grown on Cu/Ni(111) alloy foil. The color indicates the peak position of the 2D peaks, where purple (2580 cm^{-1}) represents pure ^{13}C- and red (2680 cm^{-1}) represents (almost) pure ^{12}C-labeled graphene.

In the 2D peak mapping data (**Figure 3.13**), the central region is observed to be pure ^{13}C (purple color; 2D peak position around 2580 cm^{-1}) with a sharp transition to a blue ring (mixed $^{13}C/^{12}C$ with around 9% ^{12}C and 91% ^{13}C after the introduction of normal CH_4). The percentage of ^{12}C in the growing graphene islands increased with increasing feed time of normal CH_4 (The outermost red ring shows a 2D peak at 2665 cm^{-1} equivalent to about 14% ^{13}C, and the remainder is ^{12}C). Both the pure Cu(111) and Cu/Ni(111) foils showed similar mapping results when pure ^{13}C-labeled graphene was initially nucleated and grew into islands with an increasing amount of ^{12}C is mixed in following the introduction of normal methane. Both the pure Cu(111) and Cu/Ni(111) foils showed a transitional zone with several rings (^{13}C gradually decreasing and ^{12}C increasing). This result proves that graphene growth on the Cu/Ni(111) foil used in this work is surface-mediated,[129-130] similar to graphene growth on pure Cu. There is evidently an influence of the flow characteristics of the CVD system we used, in that the transition from ^{13}C-labeled graphene in the interior of the islands to graphene at the perimeter of the islands that is enriched in ^{12}C is 'gradual'.

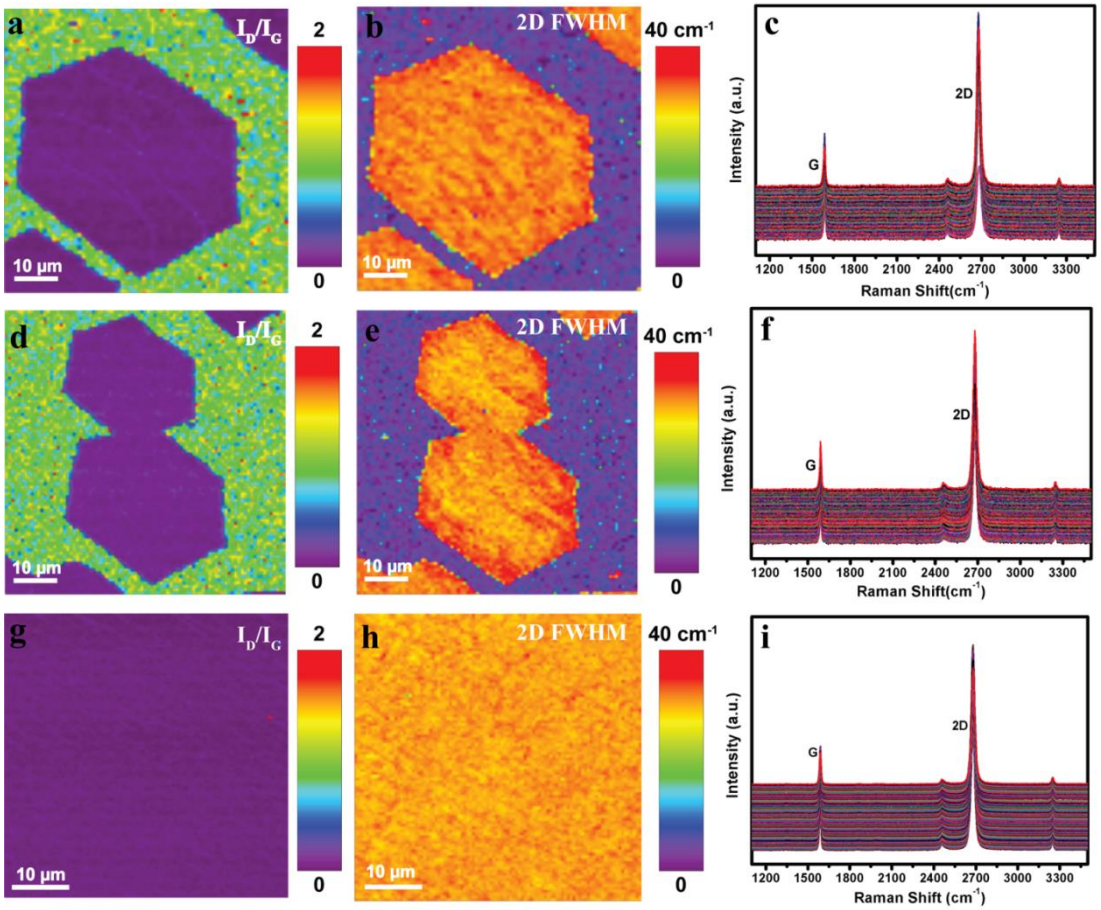

Figure 3.14. Raman characterization/mapping of graphene. Raman maps of the I_D/I_G peak height ratio and 2D FWHM of (a and b), hexagonal islands, (d and e) joined islands, and (g and h) a continuous monolayer graphene film. (c, f, i) Raman spectra randomly taken at ~100 locations on the islands and on the continuous film.

Raman spectroscopy was used to evaluate the number of layers, 'quality' and uniformity of the obtained graphene samples. **Figure 3.14a** shows a typical Raman map of a hexagonal graphene island which indicates a negligible intensity of the D band even at the edges, suggesting dominant zigzag termination.[131-133] The I_D/I_G peak height ratio and 2D average full width at half-maximum (FWHM) maps also show a high uniformity across the whole island (which is representative of all the islands that we studied by Raman). One hundred representative Raman spectra taken from the mapping region showed sharp G and 2D peaks with a 2D/G peak ratio of ~3; no D peak related to disorder or defects was detected, further indicating that the obtained graphene was a single-layer and of high quality.

Identifying the structure of the regions between the joined islands is important to further evaluate the quality of the continuous graphene film. In the Raman mapping, there was no pronounced D peak in this region (**Figure 3.14d-f**), suggesting the absence of obvious grain boundaries. This result is thus different from the observations reported in the literature of a large D peak at a grain boundary between two coalesced islands of different orientation.[71, 134]

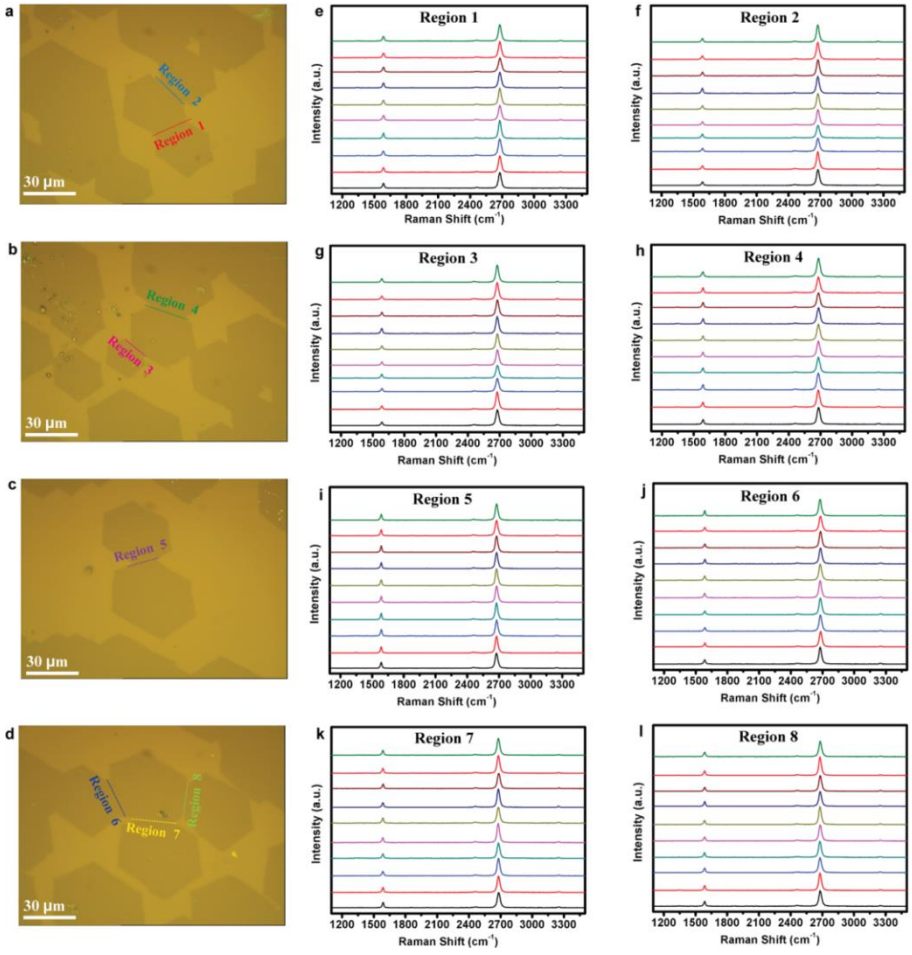

Figure 3.15. Raman line spectra collected at the regions where the different graphene islands merged. (a–d) Optical images at different merge regions. (e–l) Corresponding Raman line spectra taken at different merge regions of the islands.

Raman line scans and the statistics of the height ratio of the D peak to the G peak collected across whole graphene island(s) and for the merged regions are given in **Figure 3.15**. The negligible D peak and the uniform I_D/I_G ratio (~0.01) throughout the islands and in the merge regions is further proof of the absence of grain boundaries.

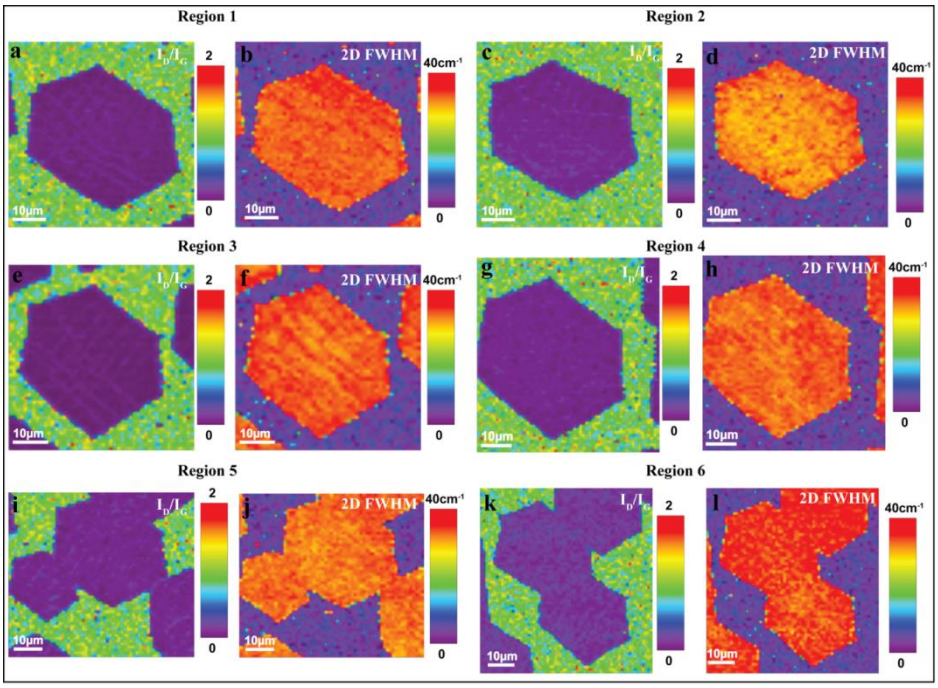

Figure 3.16. Characterization of hexagonal graphene islands and joined islands. Raman mapping of different regions shows the high quality of the graphene islands without any D peaks being observed.

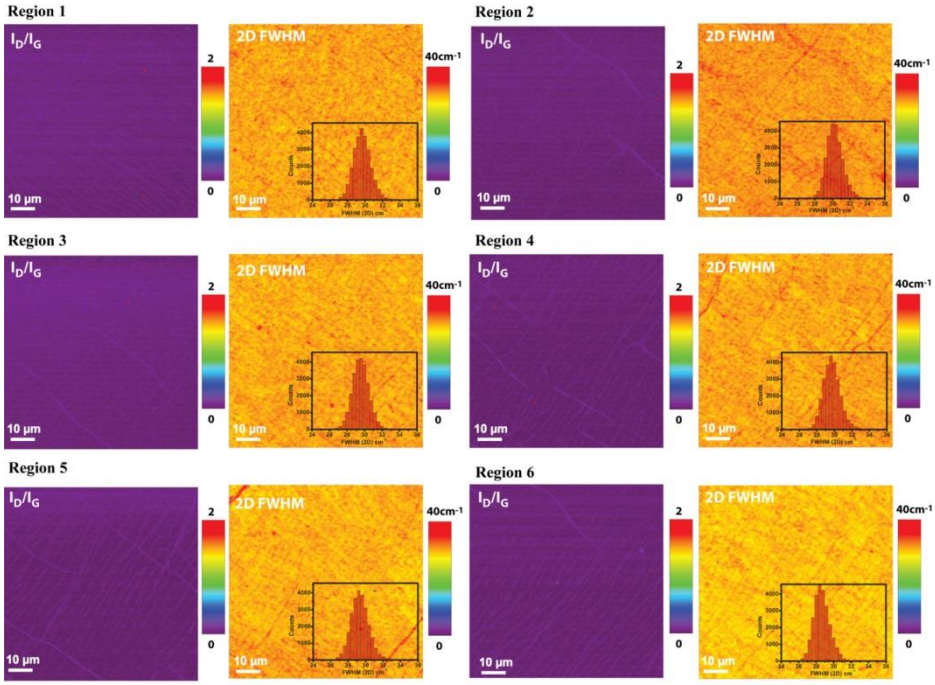

Figure 3.17. Evaluating the uniformity of the monolayer graphene film over the whole region of the transferred sample (1 ×1 cm^2). Insets are histograms of the 2D FWHM of the Raman 2D band.

Raman maps of several isolated islands as well as joined islands across the whole sample confirm the high quality and uniformity of the islands (**Figure 3.16**). **Figure 3.14g-h** show the Raman maps of the I_D/I_G ratio and 2D FWHM of the continuous monolayer graphene film. The whole area has a very uniform color and an average FWHM of the 2D peaks of 30 cm^{-1}, proving that monolayer graphene films with high quality and uniformity were obtained. More areas mapped in different regions across the whole sample are shown in **Figure 3.17**.

Furthermore, the low-energy electron diffraction (LEED) pattern of monolayer graphene grown on Cu/Ni(111) (Cu_6Ni_1 surface, bulk composition 5.9 at.% Ni) shows six sharp hexagonally-arranged spots that correspond to a highly-oriented monolayer graphene film (**Figure 3.18**). A series of LEED patterns (**Figure 3.18d-f**) of the graphene-coated Cu/Ni(111) foil taken at different positions confirmed that the graphene grown on the Cu/Ni(111) alloy foil also had a single orientation.

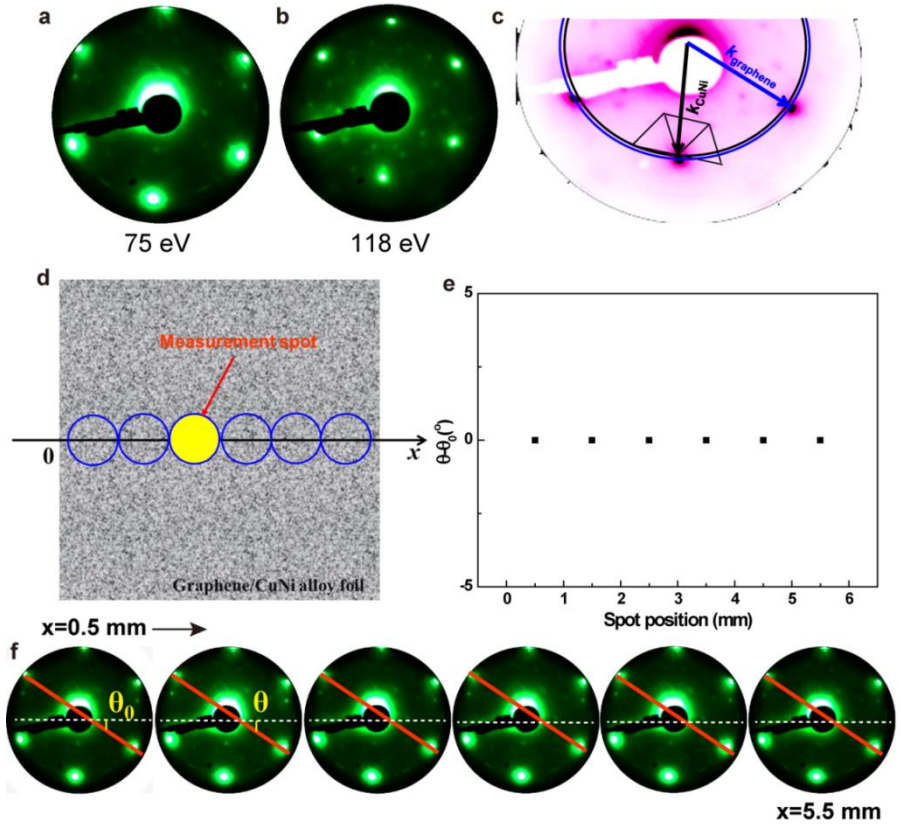

Figure 3.18. (a, b) LEED patterns of single-layer graphene on Cu/Ni(111) (5.9 at.% bulk Ni). (c) LEED analysis of graphene on Cu/Ni(111) surface; the graphene lattice is aligned with the Cu/Ni(111) substrate (d) Schematic of the LEED measurement (spot size is 1 mm^2). (e) Dependence of the angle of the diffraction spots on the sample position (angle θ-θ_0 is marked in (f), where θ_0 is the angle between the horizontal dashed line and the red line from the first measured position, and θ represents the angles for the other positions); no difference in angle is seen. (f) LEED patterns taken across the sample in steps of 0.5 mm. The LEED patterns were obtained at a beam energy of 75 eV.

To further study the influence of superstructure (Cu_6Ni_1 on the Cu/Ni(111) surface) on the growth of highly-oriented graphene, we have performed density functional theory (DFT) calculations (collaboration with Prof. Feng Ding's group) within the method of Tkatchenko and Scheffler (DFT-TS).[104] Results show that the configuration with a C atom above each Ni atom (*top-fcc*) is the most stable one for graphene on the Cu_6Ni_1(111) surface (**Figure 3.19a**). The *top-hcp*, *bridge*, and *fcc-hcp* configurations show weaker interactions (but only a few meV per atom smaller than that of *top-fcc*). The distance between graphene and this surface ranges from 0.32 to 0.34 nm, indicating that the interaction between graphene and the Cu_6Ni_1 substrate is a typical van der Waals interaction. In addition, the extent of graphene corrugation, and the mean distance from the (slightly corrugated) graphene to the substrate is affected by the surface structure of the alloy (ranging from (weak) van der Waals physisorption to chemisorption based on the surface Ni distribution). According to our calculations, the van der Waals interaction between the superstructure surface and the graphene layer is 112 meV/atom on the Cu(111) surface, 117 meV/atom on Cu_6Ni_1(111) (inset in **Figure 3.19b**), and 121 meV/atom on Cu_2Ni_1(111) (inset in **Figure 3.19b**). Further increasing the content of Ni to 100% on the surface leads to a binding energy of 160 meV/atom and a graphene-metal surface distance of 2.15 Å. These calculations show that increasing the Ni content (such as in the superstructure) should increase the van der Waals interaction, until eventually there is a cross over to what may be termed chemisorption, with a much shorter graphene-metal surface distance.

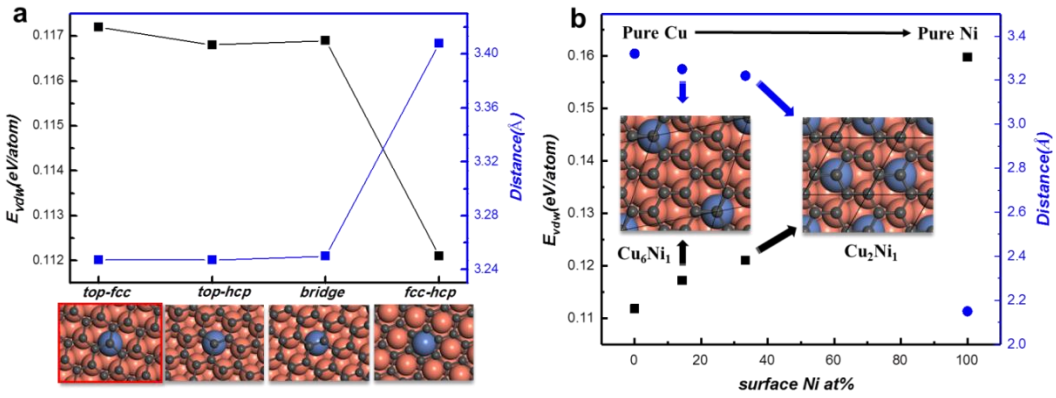

Figure 3.19. Theoretical investigation of the influence of the superstructure Cu/Ni(111) surface on the graphene growth. (a) The van der Waals energies of different configurations for graphene on the superstructure surface with the stoichiometry Cu_6Ni_1 (black squares), and the corresponding distances between the graphene layer and the substrate (blue squares). (b) The van der Waals energies (black squares) of graphene on the superstructure surfaces with different surface Ni content, and the corresponding distance of the graphene layer to the substrate (blue circles).

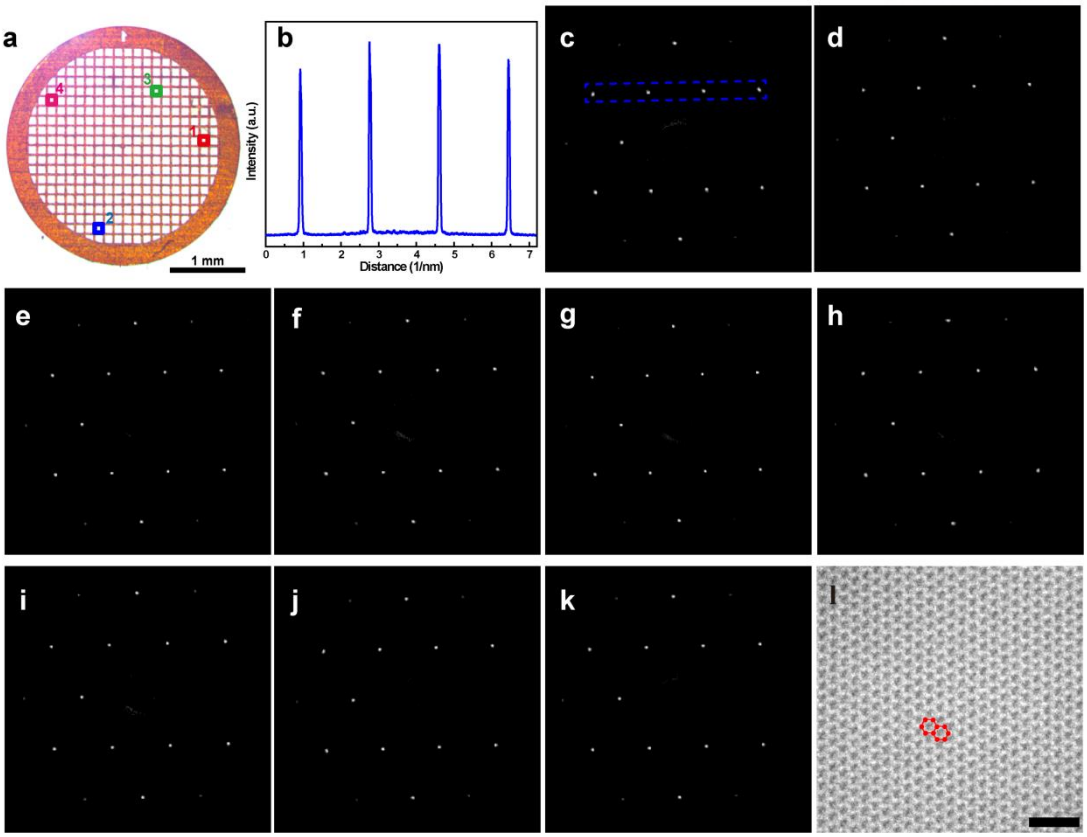

Figure 3.20. Millimeter-scale grain mapping of a single-layer graphene film. (a) Photograph of a graphene film transferred onto a TEM grid. The squares marked 1 to 4 indicate the regions where multiple SAEDs were obtained. (b) Intensity profile of the diffraction spots along the line illustrated in (c). (c–k) Nine representative SAED patterns taken from different grid holes as indicated in (a). (l) HR-TEM image of the single-layer graphene film showing a hexagonal atomic arrangement. The scale bar in (l) is 1 nm.

The crystal structure of the continuous graphene film was investigated using SAED and HR-TEM imaging. **Figure 3.20a** shows a photograph of a graphene film transferred onto a TEM grid (3 mm in diameter). Multiple SAEDs were acquired at four different regions and nine representative SAED patterns taken from different positions on the grid are shown in **Figure 3.20c-k**. Each of the SAED patterns shows only one hexagonal diffraction pattern, and an average band intensity ratio (outermost to innermost) of 0.83 (**Figure 3.20b**), confirming that the graphene sample is a monolayer. Three batches of continuous monolayer graphene samples obtained in different CVD growth runs and more than 100 SAED patterns were randomly collected, and the SAED patterns are essentially identical with a uniform six-fold symmetry (the typical SAED patterns are shown in **Figure 3.21**), demonstrating the single crystalline nature and quality of the monolayer graphene film. **Figure 3.20l** shows an atomic-resolution TEM image of graphene with a perfect carbon lattice with six-fold symmetry with no structural defects or disorder.

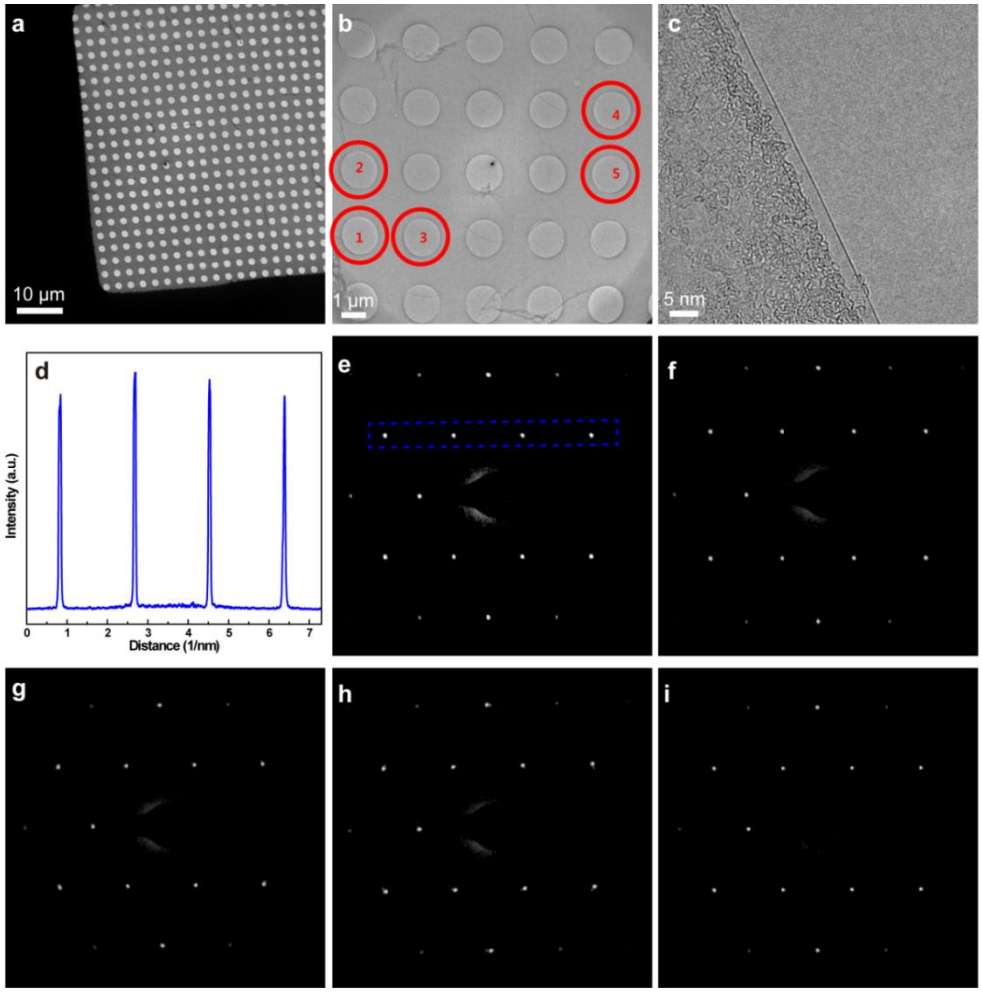

Figure 3.21. TEM and SAED patterns showing that the monolayer graphene film is highly-oriented. (a, b) TEM images of the monolayer graphene transferred on a TEM grid. The red circles indicate the presence of a graphene film suspended over several grid holes. (c) High-resolution TEM image of monolayer graphene. (d) Intensities of the diffraction spots along the line illustrated in (e). (e-i) SAED patterns recorded from areas 1–5 indicated by the red circles in (b).

Hydrogen etching is an effective method by which the crystal orientation and the grain size of CVD grown graphene can be visualized and measured.[135-137] Here, we used this etching method to determine whether GBs are present in the graphene samples. **Figure 3.22a-c** show hexagonal graphene islands that have been etched for 1 min in which the small etched holes are hexagonal and have edges roughly parallel to the edges of the island. Etching for 3 min led to more holes formed on the single hexagonal island (**Figure 3.22d-f**). All the etched holes are approximately hexagons oriented parallel to the edges of the islands, which is consistent with the fact that these islands are single-crystals with zigzag edges.[134, 138] We also used hydrogen etching on a continuous graphene film and examined different regions (**Figure 3.23**) across the whole sample (around 2 cm × 3 cm). The hexagonal holes are well aligned with each other over the whole sample, which indicates that the

sample is either a single-crystal graphene film, or close thereto.[136] We also compared the etching result with that on graphene grown on polycrystalline Cu foils (**Figure 3.24**). Etched holes with different alignment directions are observed on the continuous graphene film grown on polycrystalline Cu foil, which is likely due to grain boundaries (*i.e.*, different grains) in the polycrystalline graphene.

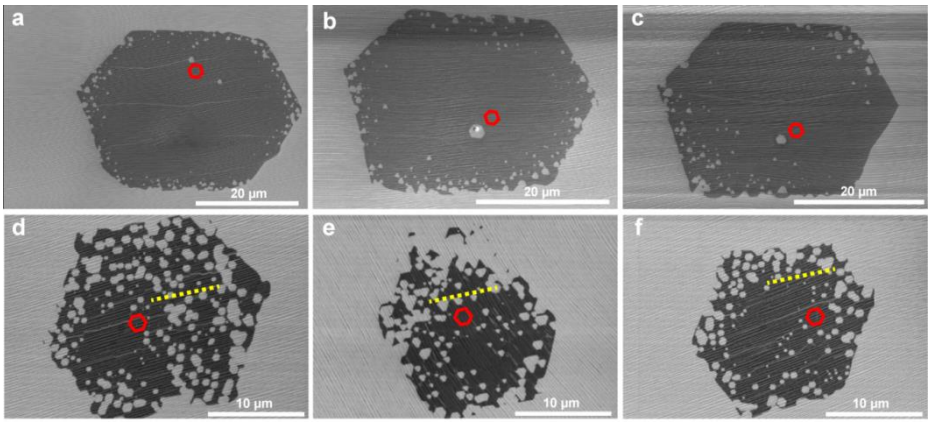

Figure 3.22. Hydrogen etching of hexagonal graphene islands for different etching times. SEM images (a–c) after 1-min etching and (d–f) after 3-min etching.

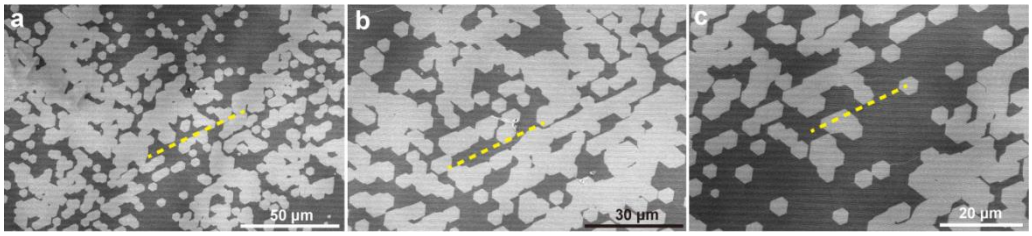

Figure 3.23. Hydrogen etching of a continuous monolayer graphene film grown on Cu/Ni(111) foil. SEM images of the etched graphene film at different regions on the sample.

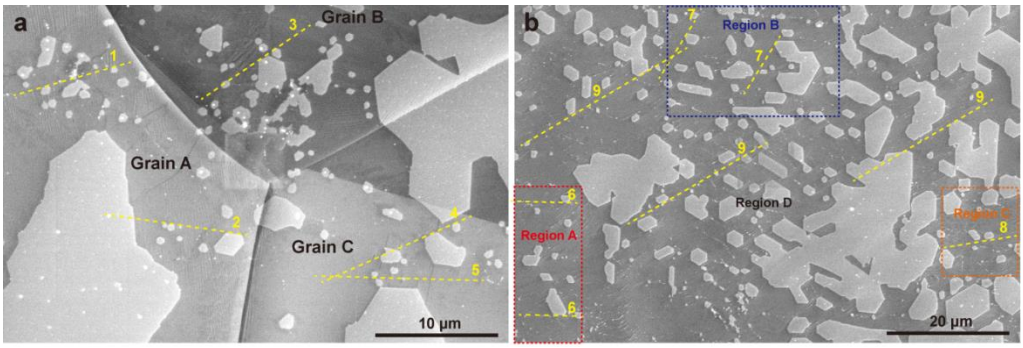

Figure 3.24. Hydrogen etching of a continuous monolayer graphene film on polycrystalline Cu foil.

SEM images of the etched graphene film at different regions across the sample. Different etching directions (highlighted by the yellow dashed lines) are observed on differently oriented Cu grains (a), which are also observed in different regions on the same Cu grain (b). In addition, one can roughly obtain the grain size of graphene by comparing the directions of the etching holes (as shown in the marked boxes in (b)).

Liquid crystal (LC)-assisted polarized optical microscopy (POM) was also used to examine the crystallinity of the graphene samples.[139] **Figure 3.25a** shows an optical image of LC-coated hexagonal graphene islands on 300-nm SiO_2-on-Si. **Figure 3.25b-f** show POM images of the graphene islands using different rotation angles of the analyzer. The colors of all the hexagonal islands are uniform and change in an identical manner for different rotation angles, indicating that they have the same orientation. POM measurements on the continuous monolayer graphene show a highly uniform birefringence color across the whole sample (**Figure 3.25g-h**), indicating a highly oriented continuous monolayer graphene film. This is quite different from what was observed on a polycrystalline graphene film grown on the polycrystalline Cu/Ni alloy (**Figure 3.25i**). Therefore, POM measurements on both sub-monolayer and continuous graphene film grown on Cu/Ni(111) foils show a highly uniform birefringence color across the whole sample, further confirming that the graphene is highly oriented, being either a single crystal or very close thereto.

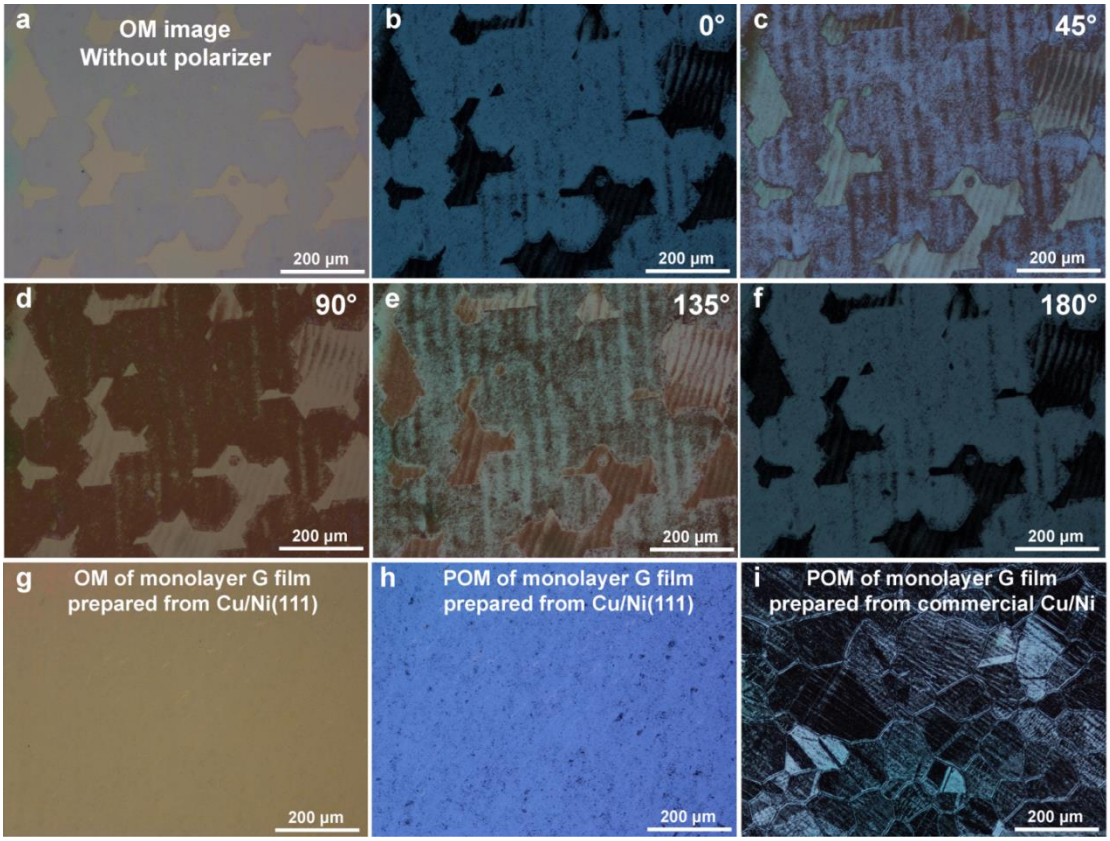

Figure 3.25. Polarized optical microscopy (POM) imaging of graphene using a nematic liquid crystal (5CB). (a) OM image of monolayer graphene islands grown on the Cu/Ni(111) alloy foil transferred onto 300-nm SiO_2-on-Si wafer. (b–f) POM images of the monolayer graphene islands after coating with 4-pentyl-4-cyanobiphenyl (5CB; Sigma Aldrich) liquid crystals. (g) OM image of a continuous monolayer graphene film prepared on the Cu/Ni(111) alloy foil and transferred onto a 300-nm SiO_2-on-Si wafer. (h) POM image of the continuous monolayer graphene in (g). (i) POM image of a monolayer graphene film prepared from a commercial polycrystalline Cu/Ni alloy.

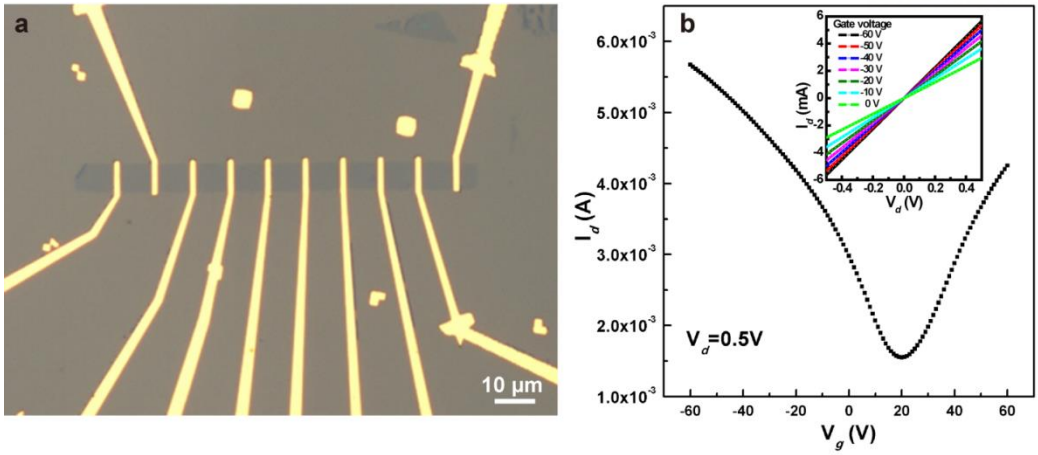

Figure 3.26. Measurement of electrical transport of the monolayer graphene film grown on Cu/Ni(111) foil. (a) Optical microscopy image of the fabricated device on a 300-nm thick SiO_2/Si substrate. (b) Typical gate-dependent conductance of the device measured at room temperature. The inset shows the linear and symmetric I_d-V_d curve, indicating a good ohmic contact between the Cr/Au contact and the graphene channels.

Table 3.1. Statistics of carrier mobility from the GFET devices for monolayer graphene.

Device number	Hole mobility ($cm^2 V^{-1} s^{-1}$)	Electron mobility ($cm^2 V^{-1} s^{-1}$)
1	5148	4744
2	2427	2321
3	11339	10077
4	3382	3259
5	3516	3336
6	9228	8894
7	2462	2184
8	4925	4369
9	11325	11129
10	4424	4268
11	8708	8269
12	2858	2106
13	6015	5220
14	3920	3100
15	5602	4745
16	8292	7406
17	2410	2074
18	8791	7416

To evaluate the electrical characteristics of the highly-oriented graphene film, transport measurements were performed on a back-gated graphene field-effect transistor (GFET) on a SiO_2-on-Si (with a 300 nm thick SiO_2 layer; henceforth referred to as "300-nm SiO_2-on-Si") substrate (**Figure 3.26**). A typical gate-dependent conductance plot and the statistics of the carrier mobility are shown in **Figure 3.26b** and **Table 3.1**. The carrier mobility extracted from a total of 18 devices (highest value was 11339 $cm^2\ V^{-1}\ s^{-1}$ and the average value 5800 $cm^2\ V^{-1}\ s^{-1}$ for holes) and (highest value was 11129 $cm^2\ V^{-1}\ S^{-1}$ and average value 5273 $cm^2\ V^{-1}\ s^{-1}$ for electrons). These electrical measurements indicate the good quality of the continuous monolayer graphene film. In addition, the transmittance of monolayer graphene was measured to be 97.7% at 550 nm (**Figure 3.27a**), which agrees with the ideal transmittance value for monolayer graphene at this wavelength.[11] The sheet resistance (**Figure 3.27b**) of the transferred graphene is ~ 650 Ω/sq, which is comparable to or lower than previously reported values.[140-142]

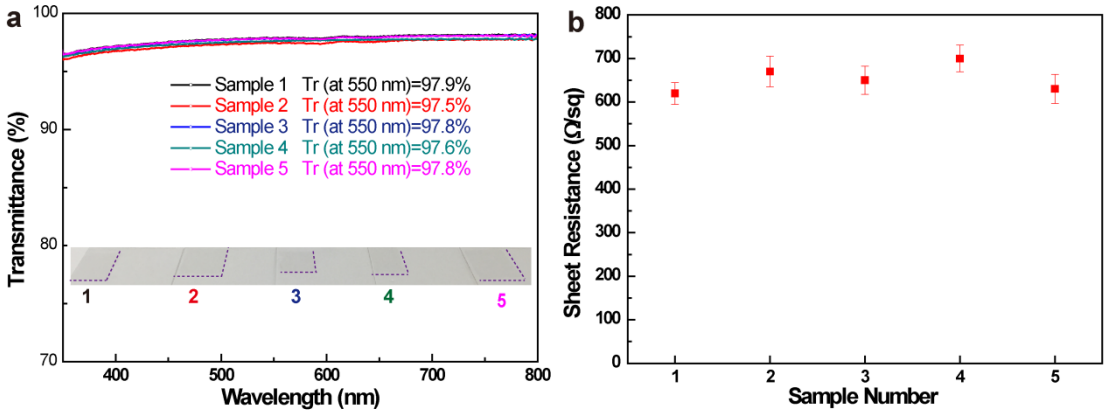

Figure 3.27. Properties of the monolayer graphene film. (a) Optical transmittance and (b) sheet resistance.

3.4 Graphene folds in a continuous film and in joined islands

We observed "fold" structures in the continuous single crystal (epitaxial) graphene film, which are formed due to a mismatch in thermal expansion (and thus also thermal contraction) between the metal foil substrate and graphene during the cooling process;[143] these folds have a thickness of around 0.7 nm as measured by AFM, which is consistent with the thickness of double layer graphene, indicating the folding of graphene (this is a 3-layer region with respect to the substrate). Such folds are rather fascinating. Wrinkles in graphene are typically observed after the metal substrate is cooled to room temperature, and they are typically much smaller—such as for graphene grown on polycrystalline copper foils. For the growths described here, perhaps the "wrinkle" reaches a large height, roughly around 40 nm, but even as high as 300 nm, and then falls over onto the substrate; alternatively, due to the contraction of the Cu/Ni(111) foil, one layer 'slides' over the other layer in some manner. We also found that these folding structures are essentially perpendicular to the direction of the steps present on

the substrate with lengths up to millimeters (**Figure 3.28**) and widths ranging from 10 nm to 300 nm. It has been stated that the metal steps underneath graphene can partially release the compressive stress in graphene perpendicular to the step direction.[144] Under this assumption, the primary component of compressive stress that remains will be along the step direction and will evidently lead to the formation of folds perpendicular to the steps. The gap between the folds is roughly 20 μm. Such (essentially) parallel folds all run perpendicular to step edges and are present due to the buildup of compressive stress during cooling of the metal foil that causes the graphene to de-adhere in these regions. Accounting for the width of the folds (twice that number is the total of width of graphene that is folded over) and the spacing between the folds, roughly 0.1 to 3% of the continuous and single crystal graphene has these long, folded regions.

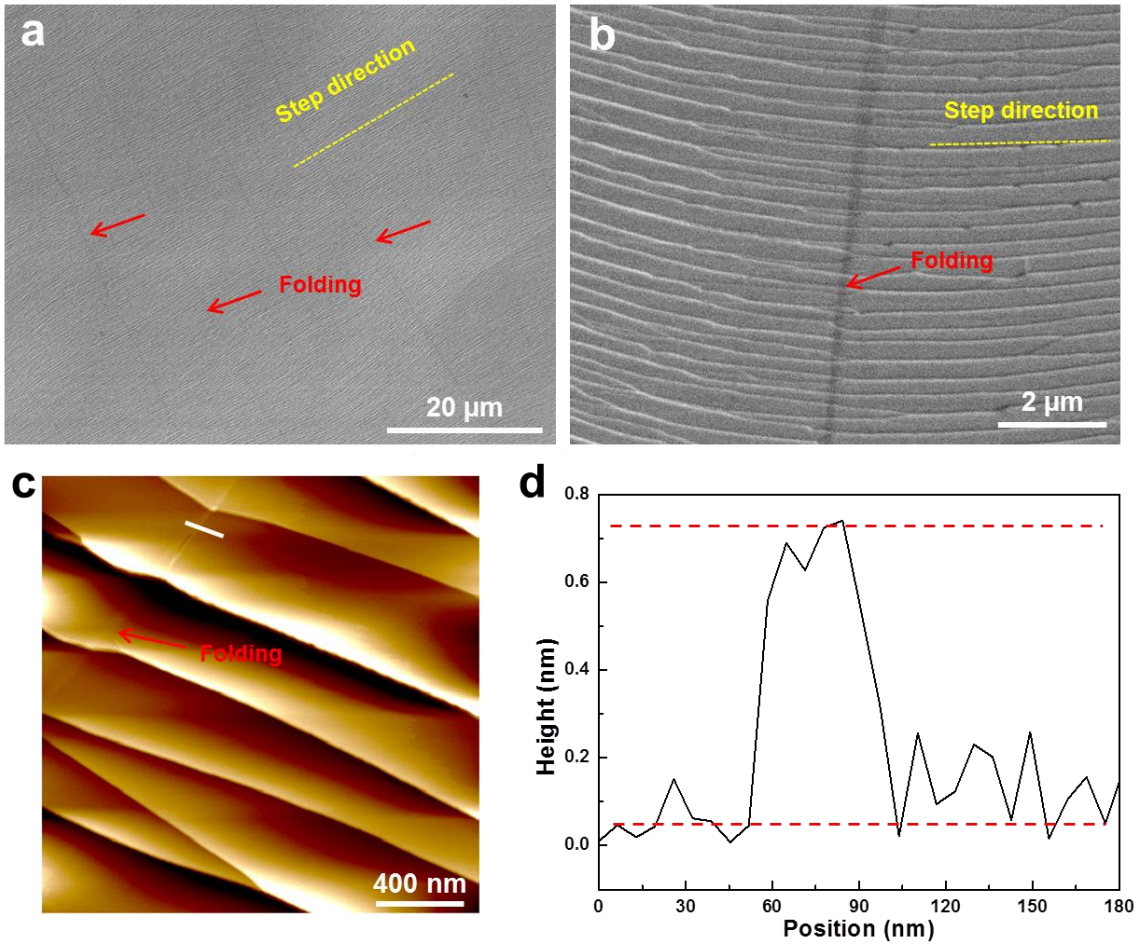

Figure 3.28. Characterization of the folding in a continuous graphene film on Cu/Ni(111) foil. (a, b) SEM images of the fold regions in the continuous graphene. (c) AFM topographic image of a fold region. (d) Height profile along the white line indicated in (c). The height change along the white line in (c) is around 0.7 nm, which is equivalent to the thickness of two layers of graphene (3 layers of graphene with respect to the substrate).

To study the structure of the graphene islands in the region where their edges join (growth stopped prior to the formation of continuous film), we used SEM, AFM, STM, and atomic-resolution TEM to study the area where two adjacent islands join. We first present the HRTEM results. Besides the seamless stitching and non-seamless stitching (forming grain boundaries) of two adjacent graphene islands without/with rotation angles[91, 94] (**Figure 3.29** and **Figure 3.30**), we observed by HRTEM, we believe for the first time, folding at the region where two hexagonal graphene islands joined.

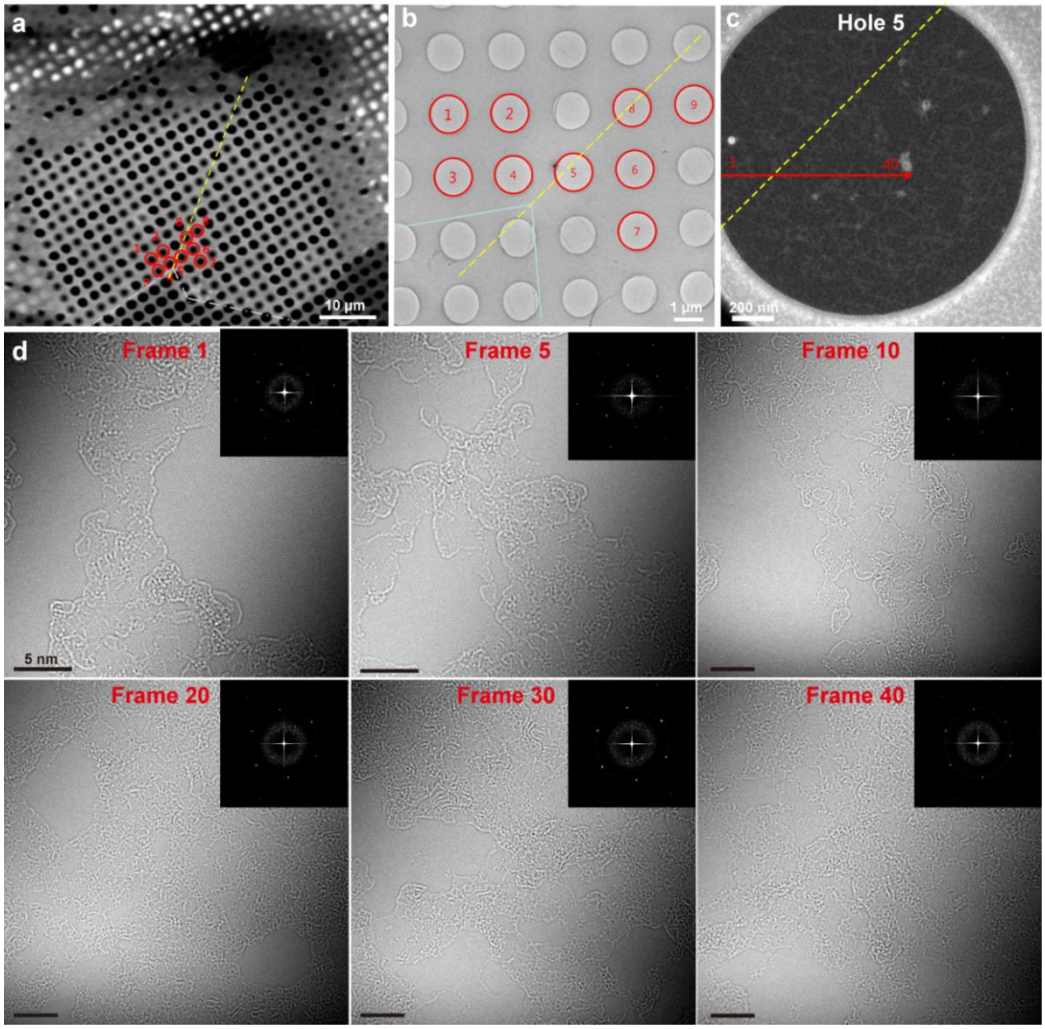

Figure 3.29. HRTEM observation across the junction of two adjacent graphene grains show no rotation angle. (a) SEM image of joined islands with the same orientation on TEM grid. (b) TEM image of the area shown in (a). The numbers labeled on the holes (in red) indicate the region where the SAED was obtained. (c) The dashed yellow line is the region where the two adjacent islands joined, while the red line is that along which 40 high-resolution TEM images were taken across the junction. (d) 6 selected images (frames 1, 5, 10, 20, 30, and 40) from the 40 continuous high-resolution TEM images. The identical orientation of all the FFTs and the absence of a distinct grain boundary in HRTEM images indicate the perfect stitching of the two islands with the same orientation. All the scale bars are 5 nm.

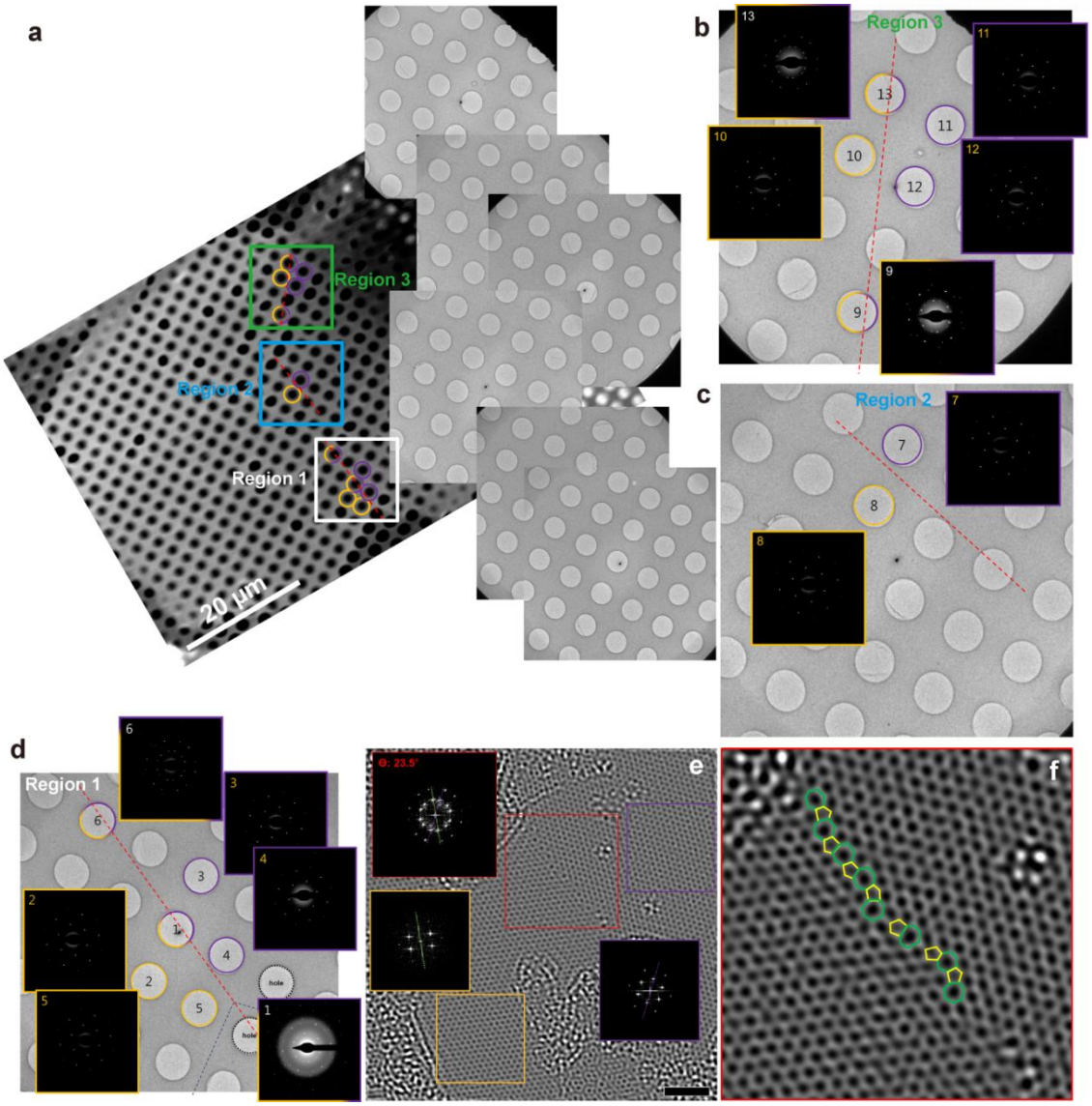

Figure 3.30. Analysis of atomic-resolution TEM images of joined graphene islands with a rotation angle with respect to each other. (a) SEM image of the two joined islands transferred onto a TEM grid. The regions enclosed by the highlighted box were analyzed. The TEM images on the right indicate the corresponding area (located at the joint between the two islands) under TEM. (b–d) Corresponding TEM images of the regions shown in (a). The numbers indicate the regions selected for acquisition of SAED. (e) HRTEM images of the graphene islands suspended over hole 1. Two grains (bottom left highlighted in yellow, top right highlighted in purple) are joined with a 23.5 ° relative rotation. A line of 5-7 defects (pentagon-heptagon pairs) occurs along the boundary between the two grains (see (f) below). The scale bar is 2 nm. (f) Magnified HRTEM image of the high-angle tilted GB of graphene (magnification of the area highlighted in red in (e)). The heptagons and pentagons are overlaid with green and yellow polygons, respectively. The GB has an array of 5-7 defects.

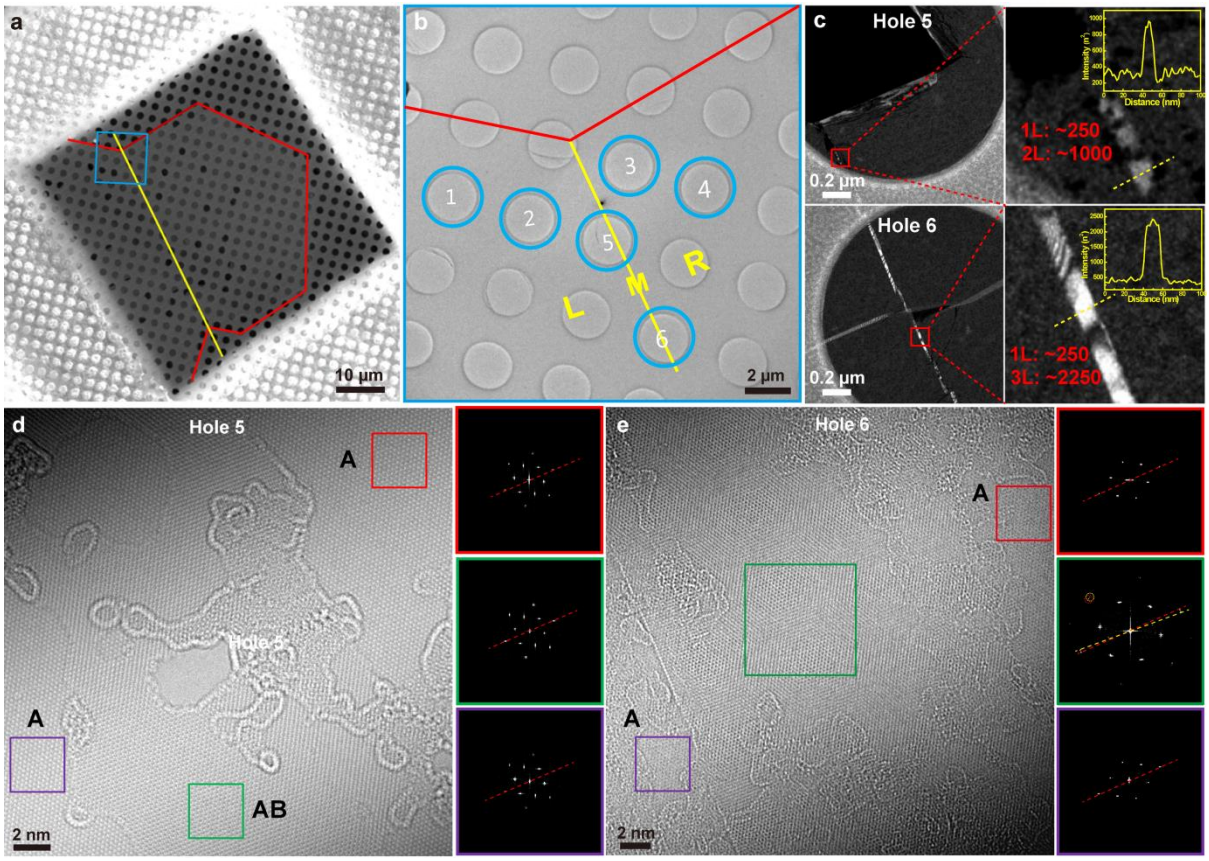

Figure 3.31. High resolution TEM observations at the junction (joining region) of two graphene islands with the same orientation. (a) SEM image of the joining area of two graphene islands with the same orientation. (b) TEM image of the area shown in (a). The red line shows the outline (edges) of the two joined islands and the yellow line indicates the boundary. The blue circles and their numbers indicate the regions where SAED and HRTEM were done. (c) DF-TEM images from hole 5 and hole 6, which are across the boundary between the two joined islands. The two on the right are the corresponding magnified images. The intensity profiles (inset) demonstrate the existence of an overlapped bilayer and a folded trilayer. (d) HRTEM image taken from hole 5 (joining region). "A" marked in the image represents the monolayer nature of the islands with the same orientation. The images on the right side are the fast Fourier transforms (FFT) of the regions highlighted in the box region. All three FFTs show one set of hexagonal spots that are essentially identical. The regions highlighted in red and purple are both single-layer regions, while the green region showed A-B stacking (AB), indicating the overlapping of two aligned islands at the joining region. (e) HRTEM image taken from hole 6 (joining region). FFT images on the right side are taken from the region within the highlighted box. The regions marked in red and purple are single-layer regions (one set of FFT, essentially identical) while the green region shows two sets of FFTs (with a rotation angle), indicating folding at the joining region.

Figure 3.31a shows a SEM image of the two islands in which the red line traces the edges of the joined islands and the yellow line indicates the joining region. A TEM image of part of this region is shown in **Figure 3.31b**. The marked blue circles indicate the areas where the SAED and HRTEM analyses were performed (L and R indicate the left island and right island, while M is the joining region). The SAED patterns at different positions on the two joined islands are essentially identical (**Figure 3.32**). **Figure 3.31c** shows dark-field (DF) TEM images of the joining region across holes 5 and 6. Magnified DF-TEM images from the regions enclosed by the red box are also shown on the right. The intensity of the bright band (joining region, hole 5) is four times that of the single-layer graphene region, which indicates that it consists of 2 overlapping graphene layers (the intensity of a DF-image acquired from a second-order diffraction spot is proportional to the square of the number of layers).[145-147] The intensity of the brighter line shown in hole 6 is nine times that of the single-layer region, corresponding to 3 layers and thus indicates folding in the joining region. **Figure 3.31d** is a HRTEM image of the region in hole 5, where we observed single-layer regions at the top-right and the bottom-left with the middle region, approximately 20-nm wide, showing an overlapping structure that is AB-stacked. Similar overlapping structures but with a non-zero rotation angle (non-AB stacked) have been observed by others for graphene grown on Cu.[148-149] The FFT patterns on the right taken from the areas in the highlighted box in **Figure 3.31d** further indicate that the overlapping of two graphene island edges is AB-stacked in the 'joining' region (the three FFT patterns taken from two islands and the middle region show only one set of hexagonal patterns with the same orientation). An interlayer shear strain and a tensile strain can be observed in the HRTEM images from the overlapping region (**Figure 3.33**).[150-151] The HRTEM images at the top-right and bottom-left regions at hole 6 (**Figure 3.31e**) are single-layer regions from two different islands with the same orientation (with a 'honeycomb' structure and corresponding FFT with the same direction). However, the middle region clearly shows misorientation (a folded structure) indicated by the two corresponding sets of hexagonal FFT patterns with a small rotation angle. In both cases, there is no evidence of a grain boundary between the two adjacent islands. These results constitute a clear evidence of the folding graphene structure in the "joining region" which is very likely due to the different thermal expansion between the graphene and Cu/Ni(111) foil during cooling to room temperature.

In addition, we checked different regions in different samples (more than 50 'joining' regions) by high resolution SEM imaging, and the percentage of 'folding regions' is around 70% (an example SEM image is shown in **Figure 3.34**). Our measurement of many of these folds shows that at the joining regions of graphene islands the folds are usually wider (10 nm to 1000 nm) than for the relatively long parallel folds in continuous graphene film (10 nm to 300 nm). We have also studied the joining region of two merged hexagonal graphene islands on Cu/Ni(111) before transfer by STM. From the STM image (**Figure 3.35**) one clearly sees folding at the joining region as was observed in the TEM imaging of the transferred samples.

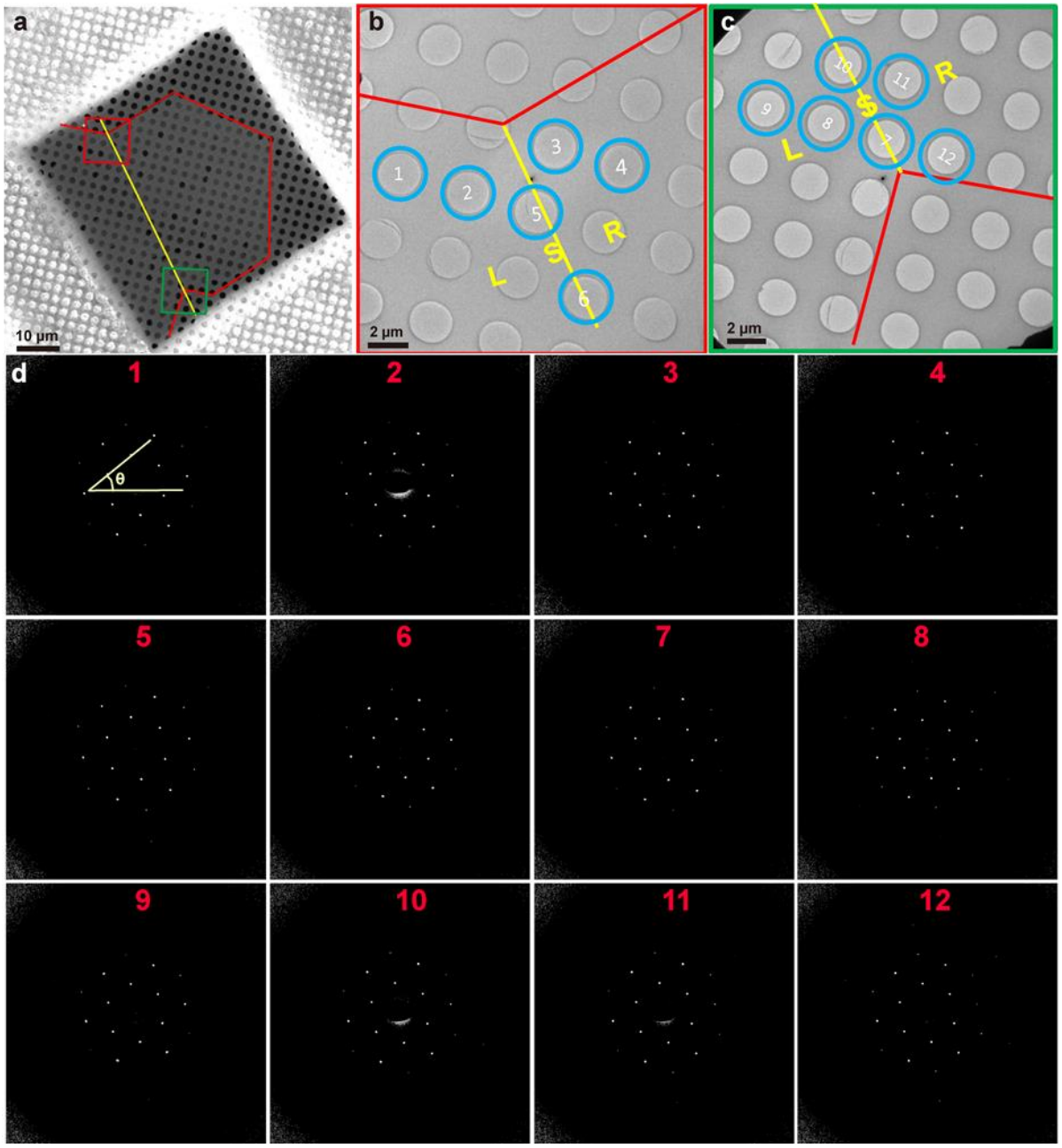

Figure 3.32. SEM, TEM images and SAED patterns obtained at the point where of two islands with the same orientation merge. (a) SEM image of two joined graphene islands with the same orientation transferred onto a TEM grid. (b, c) TEM images of the areas highlighted in (a). The red lines trace the edges (outlines) of the two adjacent islands and the yellow line indicates the hypothetical boundary (junction). The numbers of the holes indicate the regions where SAED patterns were acquired. (d) A series of SAED patterns taken from the grid holes highlighted in (b) and (c). All areas show the same orientation, indicating that the two joined islands have the same orientation.

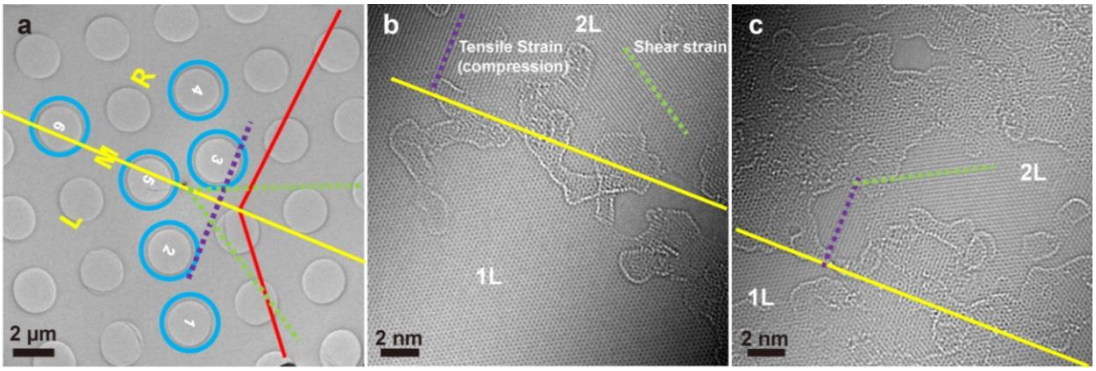

Figure 3.33. Atomic resolution TEM images of the region in the hole 5 where two islands overlap. (a) TEM image of two joined graphene islands. (b, c) HRTEM images showing the tensile strain and shear strain in the overlap (bilayer) region; the purple and green dashed lines highlight the tensile strain and shear strain at the overlap region, respectively. The left bottom part in each of (b) and (c) is the single-layer region.

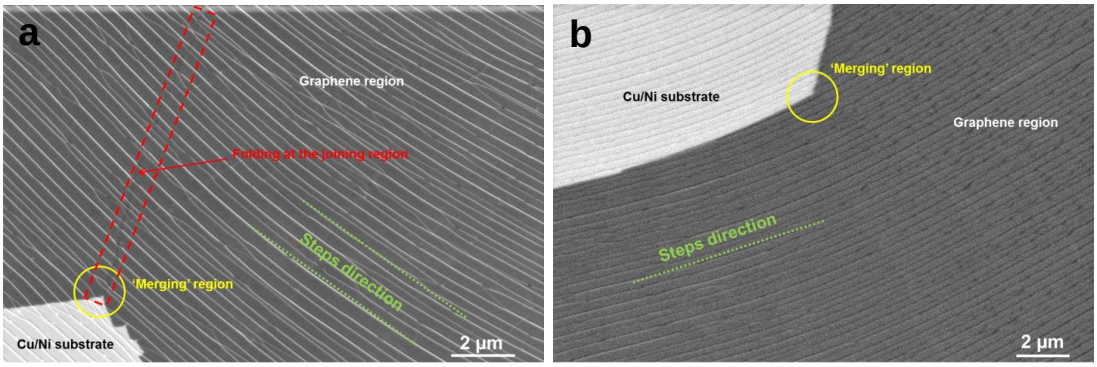

Figure 3.34. SEM images of the merging (joining) graphene islands. (a) Joining region shows folding. (b) Joining region shows no folding.

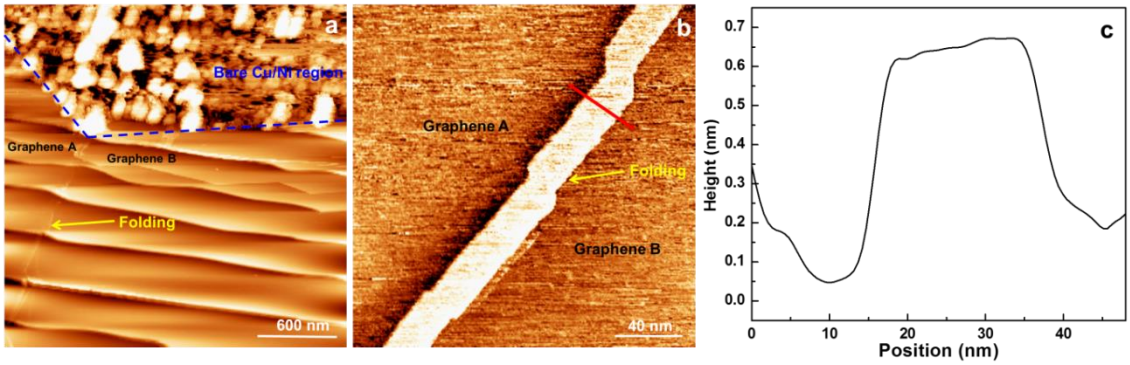

Figure 3.35. Scanning tunneling microscopy (STM) images at the joining region of two adjacent graphene islands (A and B). (a) Low-magnification STM image shows the corner of the joining region. The blue dashed line highlights the edges of the two adjacent graphene islands and the yellow arrow indicates the folding at the joining region. (b) Magnified image of the folding in image (a). (c) Height profile along the red line indicated in (b).

It is important to note that the orientation of the folds in joined islands is not (typically) perpendicular to the step edges, as observed by SEM, AFM, and STM. Indeed, an evaluation of many of these regions containing folds, showed a variety of angles between the folds and the step edges. This is because the folding of these regions is governed by different mechanics than the very long folded regions in the continuous film (**Figure 3.36**). We note that 'stress concentration' (marked with red circles in **Figure 3.36a**) should be present due to the configuration (the overall geometry) of the joined graphene islands. It is much easier to form a wrinkle (here we found it is a fold, it might be a wrinkle at first, which may then 'fall over')[152] due to release of the compressive stress (de-adhesion at this point of "weak link" in the overall structure). This hypothesis is strongly supported by our SEM, AFM and STM data. Note that there is no particular relationship between the orientation of the fold and that of the underlying steps (as per our observations on many joined islands). Briefly, folds happen in these regions because of interfacial compressive stress (as the Cu/Ni(111) foil contracts) that is concentrated at these regions due to the configuration of the joined islands, and because these regions are mechanically weaker (since they are shorter—they are 'weak links' in the structure). This is to be contrasted with the result for the continuous films where the folds are essentially perpendicular to the steps.

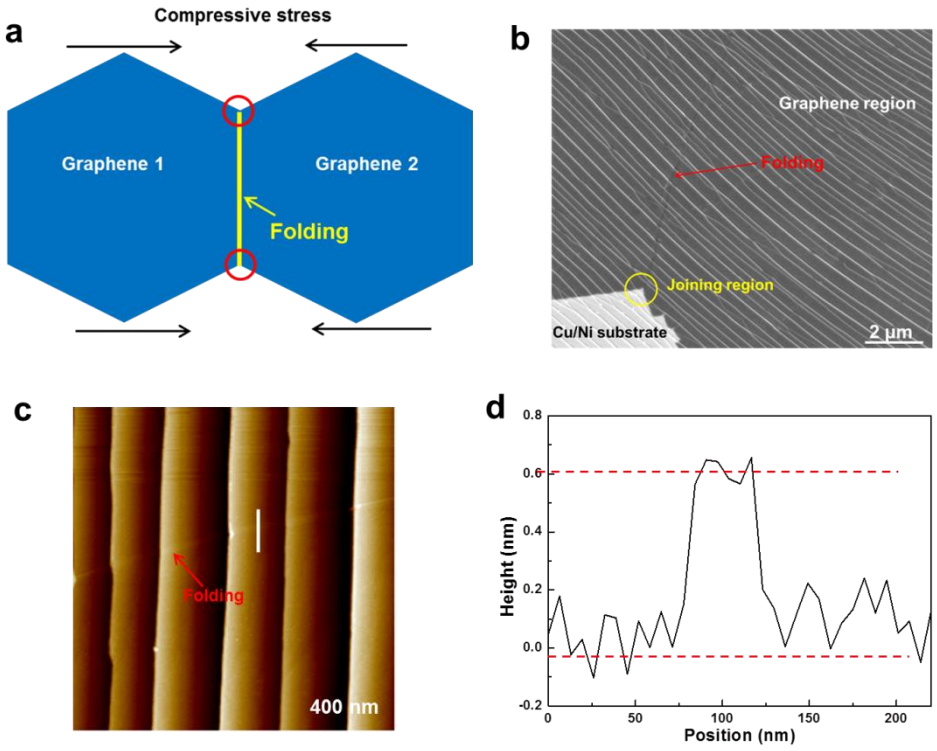

Figure 3.36. Folding in joined graphene islands on Cu/Ni(111) foil. (a) Schematic image of the fold at the junction of adjacent islands. (b) SEM image of the fold in the joining region. The yellow circle highlights the joining region. (c) AFM topographic image of the folding. (d) Height profile (white line) indicated in (c). The height is around 0.7 nm, which is consistent with a thickness of 2 layers of graphene (that is, 3 layers with respect to the substrate—a fold).

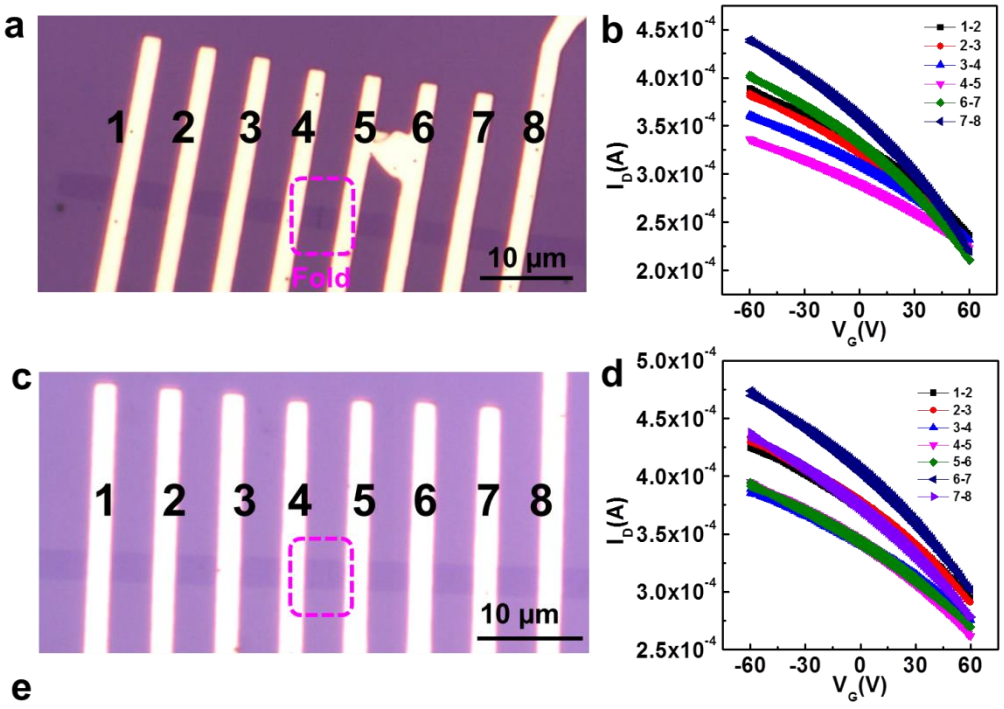

Devices (mobility, $cm^2 V^{-1} s^{-1}$)	1-2	2-3	3-4	4-5 (joining region)	5-6	6-7	7-8
With fold	3094	2895	2407	1988	N/A	4132	5251
Without fold	2381	2630	2008	2573	2232	3295	3049

Figure 3.37. Carrier mobilities across the joining regions of two adjacent islands. (a, b) Optical microscopy image and intra-island and inter-island I_d-V_g curves for joined islands having a fold. (c, d) Optical microscopy image and intra-island and inter-island I_d-V_g curves for joined islands without a fold. (e) Summary of the device mobilities extracted from (b) and (d) for the joined islands with and without a fold.

To study the possible influence of folds on electrical transport, measurements (GFET type) on joined islands with and without a fold were carried out. **Figure 3.37** shows representative intra-island and inter-island transport characteristics (I_d–V_g) of the FETs measured under ambient conditions. In the absence of folds, the mobility from the inter-island region (joined region without a fold) shows no difference to the intra-island regions, which is due to the absence of grain boundaries in the joining region. However, in the presence of folds, the mobility from the inter-island region (located at the joining region with a fold) is lower than that from the intra-island regions, demonstrating that electron scattering sites are present at the joining regions having a fold. Several studies on the electrical transport properties of intra- and inter-island regions of graphene grown on polycrystalline Cu foil are described in the literature.[134, 149, 153] Increase in sheet resistance was observed in transport

measurements across the islands (inter-island) than from within individual graphene islands (intra-island). The authors in these references mentioned that the reason for such increase in sheet resistance is due to the presence of a grain boundary or 'overlapped grain boundary' at the joining region. However, examination of previously published results (by magnifying their images, note: the folds are not very clear in the printed version rather these can be seen by magnifying the online SEM and TEM images in these references using one's computer) indicated that folds present at the joints could have been mistakenly interpreted to be grain boundaries.. In addition, the substantial increase in the sheet resistance (at joining regions for inter-island) reported in these papers indicates that there might be a grain boundary present in their joining region along with a fold, and the effects of these two features on the transport properties could not be separated. In our case, since we are using single crystal Cu/Ni(111), we do not have any grain boundaries in the joining regions of aligned graphene islands; thus, we have studied only the effect of a fold on the transport properties.

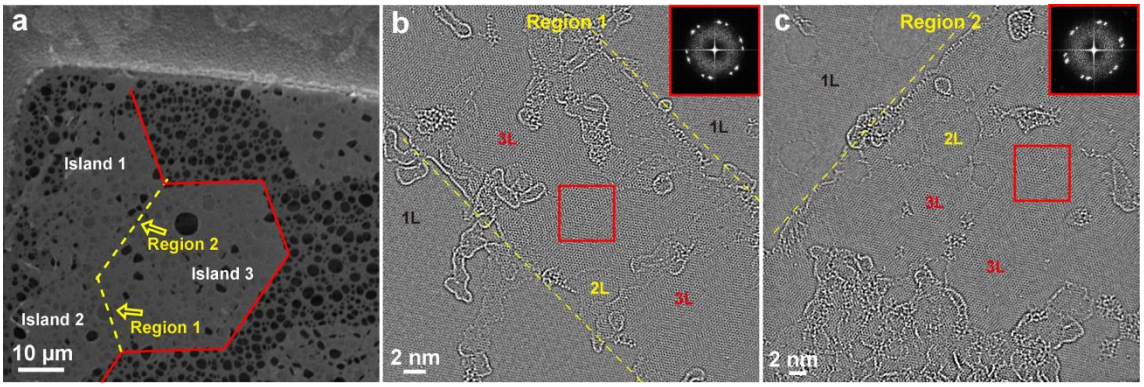

Figure 3.38. Analyses of SEM and TEM images of the junctions between three graphene islands. (a) SEM image of three adjacent graphene islands. (b, c) HRTEM image of regions 1 and 2 highlighted in (a). The number of layers in the monolayer region and the adjoining regions are highlighted in different colors. The 3L nature and the inset FFT patterns indicate the folding of both regions. 1L is the monolayer graphene region, 3L is the folded region and the 2L region (etched 3L region) is due to the e-beam irradiation ('knock-on damage' of carbon occurs under the high e-beam voltage) of the 3L region.

Evidence was also found from HRTEM that folds between joined islands can occur not only due to build up (and thus release) of compressive stress at the junctions, but also during transfer of the islands to another substrate. The atomic structures of two more joining regions (region 1 and region 2) were also characterized for three adjacent graphene islands (**Figure 3.38**). We performed HRTEM imaging of these two regions where the different numbers of layers are highlighted in different colors (**Figure 3.38b-c**). The three adjacent islands are clearly single layer; however, a narrow strip of "3L" (three layers, folding) was observed in each of the two joining regions. In the 3L joining regions, we

also observed some 2L regions (etched holes) that are created due to atom knockout caused by the e-beam irradiation.[154-155] The FFTs (insets in **Figure 3.38b-c**) acquired from each of these two regions show two sets of hexagonal patterns with a small rotation angle because of the folding (3L).

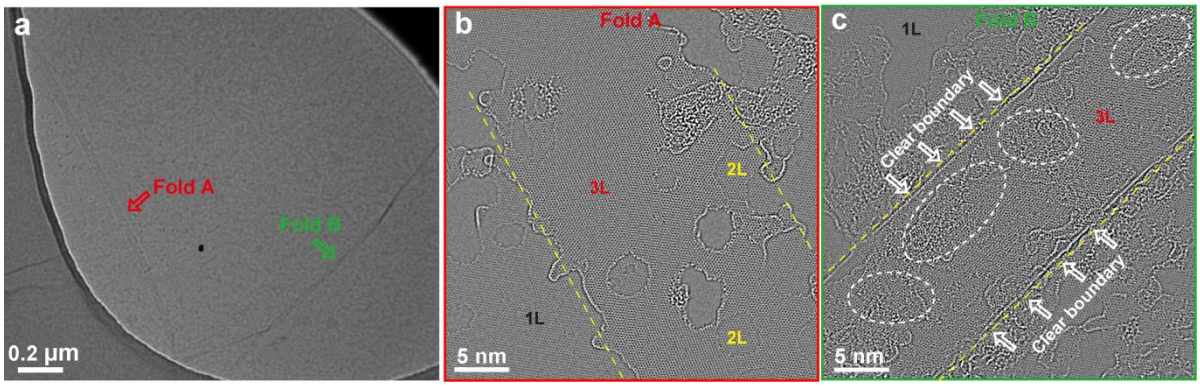

Figure 3.39. Comparison of layer folding produced during growth (located at a junction between two graphene islands) and during transfer. (a) Low magnification TEM image of the two folds. (b, c) HRTEM images of fold A and fold B highlighted in (a). Fold A is at the region where the two islands join (highlighted by the yellow dotted line) which does not show a clear boundary, but became clear under TEM beam exposure, while fold B shows a clear and straight boundary (highlighted in the image) with many contaminants (adsorbates, marked with white dotted ellipses) which persist even after long-time beam exposure.

In addition, we discovered two different types of folding, namely 'folding' during cool down (that is located in the region where adjacent islands join) and folding or wrinkles resulting from the transfer process. **Figure 3.39a** shows TEM images of two folded regions where "fold A" was taken from the joining region and "fold B" was taken from a nearby area. There are differences in these two types of folds in the presence or absence of molecular adsorbates, and in the characteristics of the boundary (the "crease"). The HRTEM image of fold A (**Figure 3.39b**) shows clean features with very few adsorbates present, while that of fold B (**Figure 3.39c**) shows many adsorbates even after long electron beam exposure. The reason why fold A is clean is that any previously present adsorbates were located on the exposed surface and were thus cleaned/removed under exposure to the high energy e-beam. However, in case of fold B, the adsorbates are evidently trapped "within" the folding region and cannot be removed due to presence of the top graphene layer. Thus, fold B happened during transfer in which the adsorbates (mainly hydrocarbons) were trapped inside the folding (stacking) layers.[156-157] In addition, the boundary of fold A (located at the joining region) is not atomically straight, while the boundaries, such as fold B, caused by transfer are always straight, and this is evidently related to how the films are transferred. (More than 10 folds of the B type were observed—always having straight boundaries). These results demonstrate that folding in the joining region

between adjacent graphene islands caused by compressive stress during cooling can be distinguished from wrinkles and folds that occur during transfer of the graphene samples, (in this case, to the TEM grid). Moreover, some of the folds can even be observed by optical microscopy.

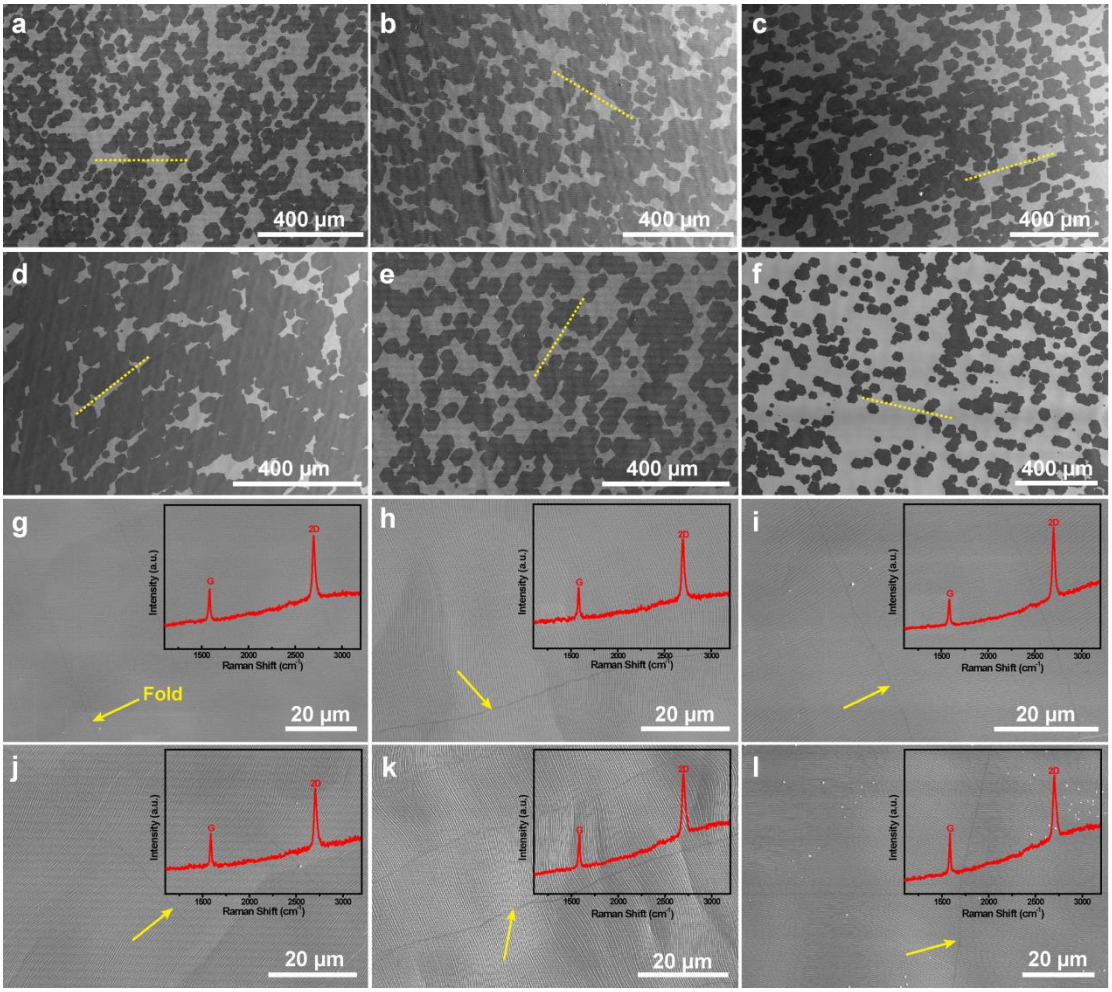

Figure 3.40. Reusing the Cu/Ni(111) foils for graphene growth. (a–f) SEM images of graphene islands on the same foil when reused. The dashed yellow lines represent the identical orientation of the islands. (g–i) SEM images of a continuous graphene film on the same substrate after it was reused. The yellow arrows indicate the folds. The insets are the corresponding Raman spectra of the graphene on the Cu/Ni(111) alloy foil.

3.5 Reuse of Cu/Ni(111) foil for graphene growth

Although straightforward, a certain amount of effort goes into preparing the Cu(111) foil based on which, Cu/Ni(111) foils are prepared with different Ni contents. One can wonder whether these substrates can be reused. Hence, we conducted repeated growth of both island and continuous graphene samples on the same Cu/Ni(111) alloy foil followed by transferring both types of graphene onto 300-nm SiO_2-on-Si wafer pieces using the electrochemical method. We found that this method does not alter the Cu/Ni(111) alloy foil that was used as the cathode during the bubbling process, and

thus allows repeated use of the foil for graphene growth. After cleaning the Cu/Ni(111) alloy foil, we used the same growth conditions to repeat graphene growth with no alteration to the foil. We repeated the growths of both the island and continuous graphene samples (**Figure 3.40**). After CVD growth, all the island samples produced in six successive growth-transfer-regrowth cycles were analyzed by SEM to monitor the quality. In all six runs, the graphene islands were hexagonal with roughly of equal size and of the same orientation. SEM images of the repeated growth of continuous graphene films on the same piece of Cu/Ni(111) alloy are shown in **Figure 3.40g-l** SEM images display growth of monolayer graphene without adlayers in the repeated growths, and indeed, we found that the method was 'perfectly' reproducible. The corresponding Raman spectra for each of the continuous graphene films grown on the Cu/Ni(111) foil are almost identical without any detectable D peak, indicating that the foils can be reused many times (essentially, forever) for the growth of high quality graphene. We also measured the weight change of each of the Cu/Ni(111) substrates during the reuse cycles (**Table 3.2**), and found there was no obvious weight change after six cycles (weight 'loss' was 0.00011 g (0.293%)), showing that the Cu/Ni(111) alloy foils can be reused, perhaps indefinitely. The results thus confirm that the Cu/Ni(111) alloy foils can be reused many times for the reproducible growth of high quality graphene without any apparent degradation of the foils.

Table 3.2. Weights of Cu/Ni(111) foils during the reuse cycles. The weight of the Cu/Ni(111) foil samples during and after reuse was measured (before and after growth).

Sample	Weight before growth (g)	Weight after growth (g)
Pristine	0.06831	0.06830
1st reuse	0.06826	0.06823
2nd reuse	0.06825	0.06824
3rd reuse	0.06824	0.06819
4th reuse	0.06818	0.06815
5th reuse	0.06814	0.06812
6th reuse	0.06811	0.06811

Conditions during weight measurement:

Equipment: METTLER TOLEDO; Measurement range: 0.00001-250 g

Temperature: 23.9 ℃-25.1 ℃; Relative humidity: 14.1%-15.3%

3.6 Conclusion

We have made large area single crystal Cu/Ni(111) foils and used them to achieve fast-growth of aligned hexagonal graphene islands and large-area highly oriented continuous graphene films. For the different samples with 1.3, 2.4, 3.9, 5.9, 6.2, and 7.8 at.% Ni in the bulk Cu/Ni(111) foil, LEED showed a superstructure in the top atomic layer(s) of the foil with the composition Cu_6Ni_1, equivalent to 14.3% Ni, and the catalytic growth of graphene is linked to the concentration and distribution of Ni

in this superstructure. Various measurements were made to characterize the graphene and it was found to be of very high quality and either single crystal or mostly single crystal, over large area. The GFET devices indicate a very high carrier mobility (highest value was 11339 $cm^2\ V^{-1}\ s^{-1}$ for holes, 11129 $cm^2\ V^{-1}\ S^{-1}$ for electrons). The continuous single crystal graphene has folded regions roughly 40 nm wide (they can be as wide as 300 nm) spaced by roughly 20 μm that run more or less parallel to each other and always perpendicular to step edges, as studied by SEM, AFM, and STM. The structure of several joined regions of adjacent graphene islands was studied using Raman spectroscopy, aberration-corrected HRTEM, SEM, AFM, and STM. Atomic-resolution TEM imaging in these regions indicated different types of joining, such as seamless stitching without GBs, one region with non-seamless stitching with a GB obviously present and also overlapping (one case only), and many joined regions that were folded. Our study on the fusion of graphene islands (that eventually forms a continuous film) also provides a methodology that will help to understand the joining of islands in other 2D materials and thin films.

Chapter 4 CVD growth of layer-tunable graphene and a study on the stacking sequence

4.1 Background research and motivation

It has been theoretically and experimentally demonstrated that the properties of graphene greatly depend on layer number.[158-159] Monolayer graphene has semimetallic properties and zero-energy band gap structure, limiting its application in semiconductor industry.[160] While AB-stackedbilayer graphene has attracted wide interest owing to its unique tunable electronic structure in a perpendicular electric field, which enables its use in electronic and photonic devices.[161-162] In multilayer graphene (typically trilayer graphene growth in our work), stacking order provides an important yet rarely explored degree of freedom for tuning its electronic properties.[163] For instance, Bernal-stacked trilayer graphene (B-TLG) is semi-metallic with a tunable band overlap, and rhombohedral-stacked trilayer graphene (r-TLG) is predicted to be semiconducting with a tunable band gap.[164-166] "Top-down" mechanical exfoliation yields bilayer graphene flakes (and many other types of flakes, so it is not selective in terms of layer number) that are typically tens of micrometers in size, but along with flakes of different thicknesses ranging from monolayer to thick multilayers.[167] The growth of large area graphene films with precisely controlled number of layers remains an important challenge for both scientific study and the practical applications. Chemical vapor deposition (CVD) is an effective "bottom-up" technique for the growth of large-area single layer graphene film on Cu foils. However, CVD growth of bilayer graphene on Cu foils still remains a challenge due to the 'self-limiting' nature of the growth process that favors single layer growth.[41] Recently, a few methods have been reported to "overcome" the 'self-limiting' effect during growth, such as spatially arranging Cu substrates in a row so that the piece(s) located upstream generate reactive gas phase species that collide with the piece(s) placed downstream,[168] adjusting the pressure of methane to control the nucleation rate,[89] introducing a high hydrogen/methane ratio (20–1400) to expose part of the monolayer-covered Cu surface,[169] use of a gradient temperature (the temperature is decreasing with a certain cooling rate) during CVD growth,[170] and using ethanol[171] rather than methane as the carbon precursor. However, a survey of the literature shows that it is still difficult to obtain a high coverage of bilayer graphene and particularly of AB-stacked bilayer graphene, over large area. In addition, there is, to the best of our knowledge, no report on high coverage, and also over larger area, of ABA-stacked trilayer graphene growth.

The alloy of Cu and Ni is a "textbook" isomorphous alloy (the Ni and Cu atoms are almost the same size and adjacent elements in the periodic table; they mix from 0% to 100% Ni in Cu). The pure metals have the face-centered cubic crystal structure. This compatibility allows to tune the solubility of carbon in a metal foil comprised of Cu and Ni by varying the atomic fraction of Ni, and thereby enable controlled growth. For example, by varying the Ni concentration, the mechanism of growth can be modified by selectively including growth through precipitation from the interior of the

foil during cooling, to enable the bilayer and multilayer graphene growth. Such strategies are based on the observation that the solubility of C in Cu at around 1000 ℃ is very low (about 75±0.5 ppm levels)[172], whereas the corresponding value at 1000 ℃ for C in Ni is 1.3 at%.[46] To date, commercial Cu/Ni alloy foils and deposited Cu/Ni thin films have been used for the growth of bilayer graphene; we have reported the use of commercial polycrystalline Cu/Ni alloy foils (such as "70-30" and "90-10" Cu-Ni alloys, ,) for the synthesis of bilayer and graphite thin films.[99-100] However, the fixed concentration of Ni and the presence of other elements that are deliberately added to such alloys particularly to improve corrosion resistance, are not conducive for an in-depth scientific study, for example, a systematic variation of Ni concentration, or having a very pure alloy of only the two elements Cu and Ni. Moreover, alloy single crystals with the (111) surface orientation are not commercially available. Alternatively, Cu/Ni alloy thin films made either by sputtering or by thermal evaporation with various alloy compositions have been used for the controlled growth of graphene film with different numbers of layers.[173-176] But the fraction of multilayer film that was AB-stacked was low and the layer stacking sequence of the grown multilayer graphene has not been fully characterized.

In this study, we first prepare a series of Cu/Ni(111) alloy foils by heat-treating Ni-plated Cu(111) foils. The Ni content in the alloy foil can be precisely controlled by adjusting the amount of the Ni plated on the Cu(111) foil. Using such 'home-made' Cu/Ni(111) foils, we have achieved large-area AB-stacked bilayer graphene with high coverage over several square centimeters (more than 95%) and high AB stacking ratio (nearly 100%). Trilayer graphene with more than 60% coverage has been achieved over several square centimeters by having a higher concentration of Ni. The structure of the bilayer and multilayer graphene has been investigated using time of flight secondary ion mass spectrometry (ToF-SIMS) mapping, hydrogen etching with in situ scanning electron microscopy (in situ SEM), and highresolution transmission electron microscopy (HRTEM) imaging of cross-sections of the samples.

4.2 Experimental section

4.2.1 Preparation of Cu/Ni(111) foil

Large-area Cu(111) foils were prepared by high temperature annealing (1050 ℃) under Ar and H_2 flow at atmospheric pressure (1 atm) for around 12 h. Nickel was then plated on the Cu(111) foil in an electrolyte containing $NiSO_4$, $NiCl_2$, NaF and H_3BO_3. The applied current density was 0.02 A cm^{-2}. After washing and drying, the Ni-plated Cu(111) foil was heat-treated in a CVD chamber at 1050 ^oC for 5–7 h to obtain a Cu/Ni(111) foil. The concentration of Ni in the alloy is determined by the weight change before and after plating process (the weight gain after the plating process is considered as the amount of Ni added into the alloy).

4.2.2 Graphene growth on Cu/Ni(111) foils

For graphene growth, the Cu/Ni(111) foil (first treated with acetic acid) was placed in a CVD system which was then pumped down to ~0.3 mTorr. The Cu/Ni(111) foil was heated up to 1075 ℃ and annealed for 120 min under a gas flow of H_2/Ar with a pressure of 40 Torr. Next, methane was introduced into the system for 10–20 minutes for graphene growth. After graphene growth, the sample was rapidly cooled down to room temperature under a constant H_2/Ar flow by sliding the furnace downstream to the cooler end of the of the CVD chamber maintained at room temperature .

4.2.3 Graphene transfer

The grown graphene was transferred by using an electrochemical delamination process. The graphene-coated Cu/Ni(111) alloy foil was spin-coated with a polymethyl methacrylate (PMMA) layer at 3000 rpm for 1 min and cured at 150 ℃ for 10 min to provide mechanical support for transfer. For the delamination process, an electrolytic cell with 1M NaOH as electrolyte was constructed with PMMA/graphene/Cu-Ni(111) (as cathode) and a Pt plate (as anode). Once a proper voltage (3-5 V) was applied between the cathode and anode, water undergoes electrolysis to form hydrogen bubbles at the interface of graphene and Cu/Ni(111) alloy, thus separating the PMMA/graphene stack away from the Cu/Ni(111) foil (the process takes around tens of seconds). After cleaning with deionized water, the floating PMMA/graphene stack was transferred to the target substrate. Finally, the PMMA film was removed by acetone.

4.2.4 LEED measurement of bilayer graphene-coated Cu/Ni(111) foil

LEED patterns were recorded at a pressure of ~1 × 10^{-10} Torr in a chamber equipped with LEED optics (SPECTRALEED, Omicron NanoTechnology GmbH). The bilayer graphene-coated Cu/Ni(111) foil sample was loaded into the LEED chamber, and then annealed at 200 ℃ overnight in ultra-high vacuum. The LEED measurement was conducted on a sample with a typical size of 1 cm × 1 cm at room temperature.

4.2.5 Optical transmittance measurement of the graphene films

The optical transmittance of the grown monolayer graphene film was examined after transferring it onto a glass cover slide. A Cary Series UV−vis−NIR spectrophotometer (Agilent Technologies) was used to measure the optical transmittance of the graphene samples, which was measured by detecting the light transmitted through a circular hole with a diameter of 5.3 mm.

4.2.6 Time-of-Flight secondary ion mass spectrometry (ToF-SIMS) measurements

ToF mass spectrometry is based on the principle that ions with the same energy but different masses travel with different velocities. Secondary ion mass spectrometry (SIMS) is a technique to analyze the

composition of solid surfaces and thin films by sputtering the surface of the specimen with a focused primary ion beam and collecting and analyzing ejected secondary ions.

The ToF-SIMS depth profiling and mapping can allow for fine control of the removal of individual layers as well as achieving high sensitivity (down to parts-per-billion) in detecting the composition of different layers. A Cs^+ ion beam (1 kV energy) was used for the sputtering process (layer removal) and the imaging process was mapped in Burst Alignment (BA) mode (high lateral resolution, around 200 nm) by a 25 kV Bi^{1+} ion beam. The imaging area was around 200 × 200 μm^2.

4.2.7 Preparation of TEM sample for cross-section HRTEM characterization

A TEM sample of multilayer graphene sheet on Cu/Ni(111) alloy was prepared by lift-out approach[177] with a dual-beam focus ion beam (FIB) instrument (Helios NanoLab 450). This instrument has a multitude of capabilities including high resolution electron imaging, ion imaging, nano-device fabrication, and material deposition, and thus enables high precision cross-section processing and TEM sample preparation. We deposited a carbon layer using the ion beam at the chosen region, to protect the graphene layers. The carbon layer protects the region of interest during the ion beam milling process and provides mechanical stability to the cross-sectional slice after its removal by milling. Trenches were milled around the carbon layer by using a 30 kV Ga^+ ion beam with a current of 0.5–2.5 nA. We then deposited a layer of carbon at one end of the target region to weld it onto a nanomanipulator needle and milling the other end of the target region and the region beneath it to remove the milled slice free from the substrate. The milled slice with a dimension of 1 μm × 5 μm × 10 μm (Width × Depth × Length) was then extracted, transferred and 'welded' onto an Omniprobe copper half grid using carbon layer deposition so that it could be separated from the nanomanipulator by FIB milling. The final fine milling was conducted using lower voltage and current (3kV–5kV and 38 pA–100 pA) to make the cross-section surface smooth and reduce the sample thickness down to less than 100 nm for TEM characterization.

4.2.8 *In situ* hydrogen etching of graphene grown on Cu/Ni(111) foil

Hydrogen etching of the graphene in the SEM chamber was performed according to our previous work.[178] Typically, hydrogen etching was conducted *in situ* after graphene growth under 10 sccm H_2 at 900 ℃ under a pressure of 25 Pa. During the etching experiment, environmental scanning electron microcopy (ESEM) was operated at an acceleration voltage of 7.5 kV and the images were acquired by a large field detector.

4.2.9 Device fabrication and measurement

Prior to measurement, the bilayer graphene samples were transferred onto a 300-nm SiO_2-on-Si substrate, followed by deposition of source and drain electrodes of Au/Cr (50 nm/5 nm) by electron

beam evaporation. Electron beam lithography was used to define and pattern the bilayer graphene to form a field-effect transistor. Oxygen plasma was used to etch away unwanted graphene regions. The back-gated GFETs were characterized at room temperature in vacuum on a MSTECH probe station with an Agilent 4155C analyzer. The mobility was obtained as

$$\mu = \frac{\mathrm{d}I_d}{\mathrm{d}V_g}\frac{L}{WC_gV_d}$$

where I_d is the source drain current, V_d is the source drain voltage, V_g is the gate voltage, L and W are the channel length and width, respectively, and C_g (11 nF cm^{-2}) is the capacitance of the back-gate dielectric layer.

4.3 Bilayer and trilayer graphene growth and characterization on Cu/Ni(111) foils

4.3.1 Preparation and characterization of Cu/Ni(111) foils

Recently, our laboratory has prepared large-area Cu(111) foils by heat-treating commercial Cu foils under Ar/H_2 environment. The characterization of the Cu(111) foils is shown in **Figure 4.1**. X-ray diffraction (XRD), scanning electron microscopy (SEM), electron backscattered diffraction (EBSD), and atomic force microscopy (AFM) were used to determine the crystallinity and surface morphology of the prepared foils. A photograph of the as-prepared Cu(111) foil is shown in **Figure 4.1a**. The XRD patterns from different regions of the annealed Cu foils show only two peaks at 43.3 °and 95.1 °in the scan range of 30–150 °which are assigned to Bragg reflections of the (111) and (222) crystallographic planes (**Figure 4.1b**). The EBSD mapping also indicates the face-centered cubic (fcc) (111) surface plane of the Cu foils, which is consistent with the XRD result. The X-ray diffraction (XRD) pattern and the electron backscatter diffraction (EBSD) mapping confirm the (111) orientation of the as-prepared Cu foils.

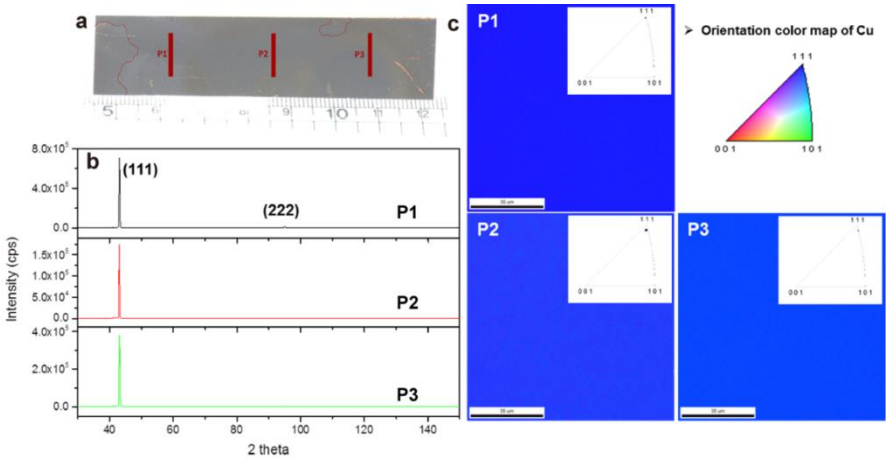

Figure 4.1. (a) Photograph of the as-prepared Cu(111) foil. (b) XRD pattern of the Cu(111) foil taken from different positions which are marked in (a). (c) EBSD mapping taken from the same positions as XRD patterns.

Figure 4.2a shows the process of preparing Cu/Ni(111) alloy foils, which includes the plating of Ni layers onto Cu(111) foils and heat-treatment of the Ni-plated Cu(111) foils. A photograph of a piece of the prepared Cu/Ni(111) alloy foil, 3 cm × 5 cm in size, is shown in **Figure 4.2b**. XRD was acquired from the marked regions. The XRD pattern of the Cu/Ni alloy shows that the foil is single crystal with (111) surface orientation.

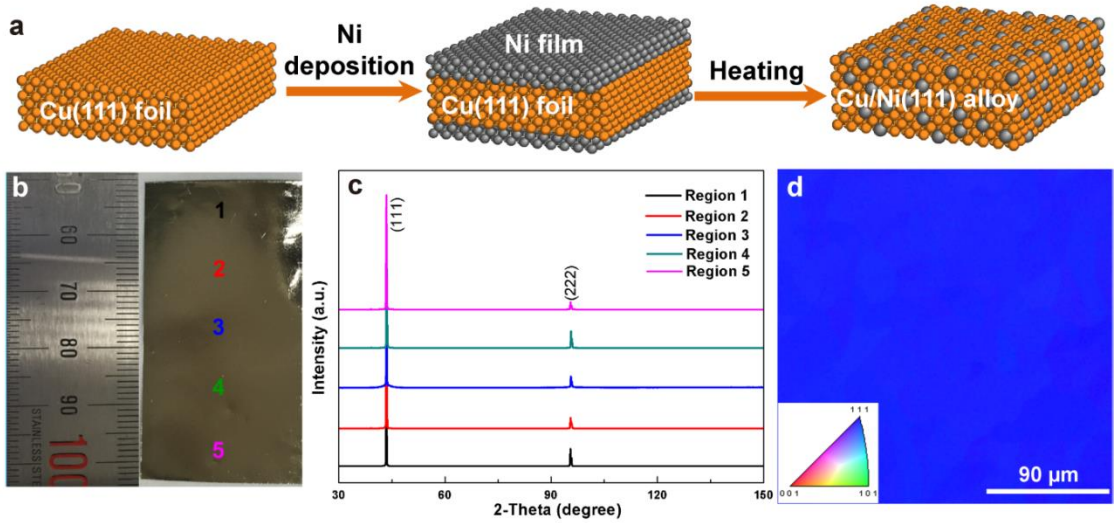

Figure 4.2. Preparation and characterization of Cu/Ni(111) foils. (a) Schematic of the preparation process of Cu/Ni(111) foil. (b) Photograph of the as-prepared Cu/Ni(111) foil. (c) XRD patterns taken from different regions across the whole sample (3 cm × 5 cm), as indicated in (b). (d) EBSD mapping of the Cu/Ni(111) foil.

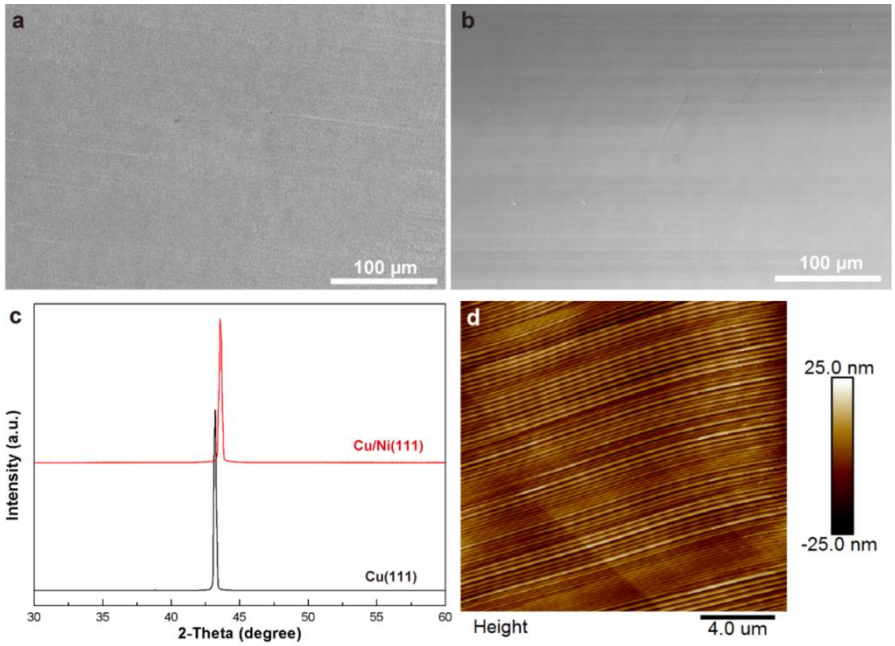

Figure 4.3. SEM images of (a) Ni-plated Cu(111), and (b) Cu/Ni(111) alloy foils. (c) XRD pattern of the Cu(111) foil and Cu/Ni(111) foil. (d) AFM image of the Cu/Ni(111) alloy surface.

SEM images of the Ni-plated Cu(111) foils and the Cu/Ni foils (**Figure 4.3a-b)** show a homogeneous and flat surface after the alloying process. The surface of the alloy was characterized as fcc (111), which is the same as that of the Cu(111) foil. The surface roughness of the as-prepared Cu/Ni(111) foil was found to be around 5 nm from the AFM measurement (**Figure 4.3d**). The EBSD maps of the Cu/Ni alloy foil and inverse pole figure (IPF) color maps of both the surface normal and transverse directions of the alloy foil are shown in **Figure 4.4**. These EBSD maps show the successful preparation of Cu/Ni(111) alloy foil from heat-treatment of the Ni-coated Cu(111) foil over a large area (about 3 cm × 5 cm).

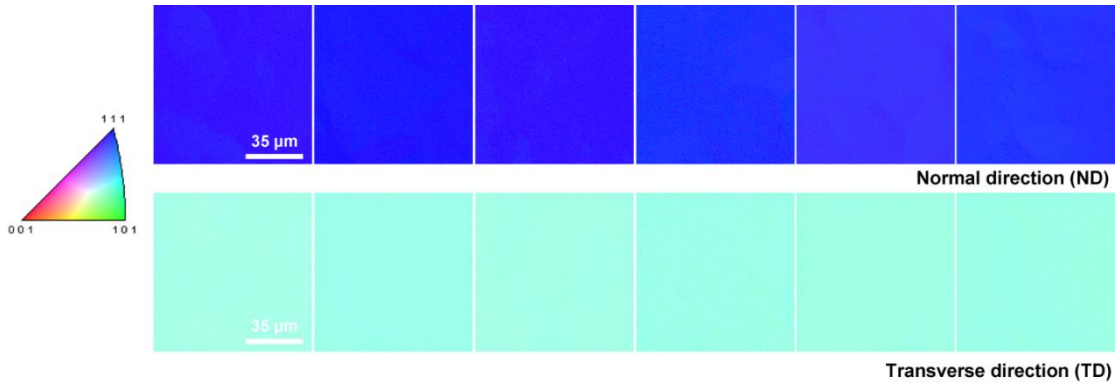

Figure 4.4. EBSD mapping at various regions on the Cu/Ni(111) foil with a size of 3 cm × 5 cm (the distance between each EBSD measurement region was more than 5 mm).

4.3.2 Characterization of bilayer and trilayer graphene

Figure 4.5a shows the Raman spectra of the graphene grown on the Cu/Ni(111) foils (15.5 wt.% Ni). No observable D peak(s) located at ~1350 cm^{-1} indicate the high quality of the as-prepared graphene films. Raman spectrum of the monolayer graphene region in the sample shows a narrow and symmetric 2D peak with an I_{2D}/I_G intensity ratio of ~2 and a full width at half maximum (FWHM) of ~30 cm^{-1}. The 2D band for bilayer graphene is much wider (the FWHM is ~51 cm^{-1}) with I_{2D}/I_G ratio close to 1, entirely consistent with AB-stacked bilayer graphene.[179] The asymmetric 2D band of the bilayer graphene can be fitted by four Lorentzian peaks, as shown in **Figure 4.5b**, proving the AB-stacking of the as-prepared bilayer graphene. **Figure 4.5c** shows an optical image of the transferred bilayer graphene island sample (the coverage was around 25%) prepared by 5-minute exposure to methane and hydrogen at 1075 ℃ (16.6 at.% Ni). **Figure 4.5d-e** show the Raman mapping of the intensity ratio of the D band to the G band, and the 2D peak FWHM of the bilayer islands, respectively. No obvious D peak(s) were observed and the uniform I_D/I_G ratio (~0.01) measured throughout the monolayer and bilayer island regions proves the high quality of the as-prepared bilayer island sample. The monolayer region and bilayer region can be easily distinguished from the 2D FWHM mapping (in the map, the monolayer region has a uniform green color and the bilayer region has a uniform red color). The uniformity in the 2D FWHM mapping also indicates that the bilayer

islands are AB-stacked (and single crystal). Increasing the growth time to 10 min resulted in the formation of a nearly continuous bilayer graphene film, **Figure 4.5f**. Raman mapping of I_D/I_G ratio and 2D FWHM for the continuous bilayer film showed uniform contrast over the entire mapping area (**Figure 4.5g-h**). The insets show representative Raman spectra from the mapping region and the 2D FWHM distribution histogram, which proves the high homogeneity of the AB-stacked bilayer graphene film.

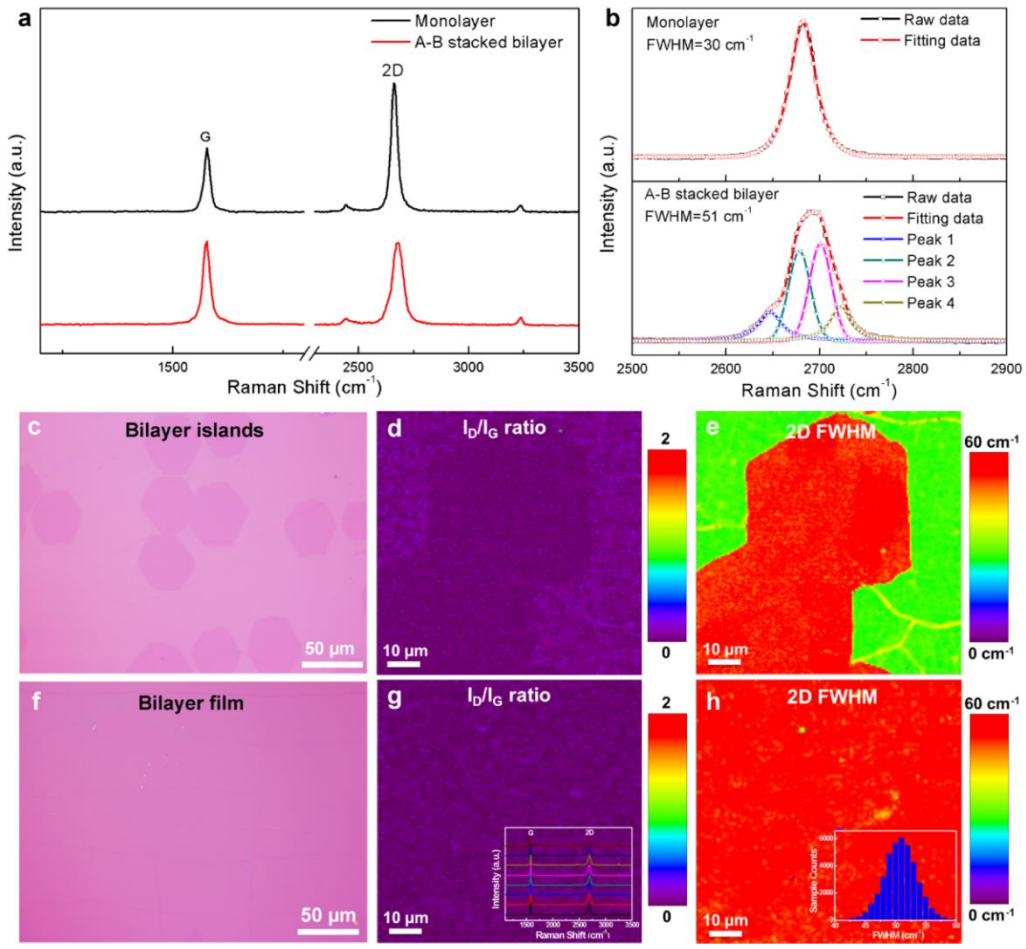

Figure 4.5. Raman spectroscopy of graphene. (a) Raman spectra of monolayer and bilayer graphene transferred onto SiO_2/Si substrates. (b) Lorentzian fitting of the 2D peaks for monolayer and AB-stacked bilayer graphene films. Optical images and Raman mappings of (c–e) bilayer islands and (f–h) a continuous bilayer film. The insets in (g) and (h) show the Raman spectra and the 2D FWHM distribution of the bilayer film, respectively.

Additional Raman mapping of the bilayer islands and of the continuous bilayer films at different regions across the entire transferred sample (1 cm × 1 cm) are given in **Figure 4.6**. The uniformity of the Raman mapping (for both bilayer island sample and bilayer continuous sample) indicates that the bilayer graphene is close to 100% AB-stacked.

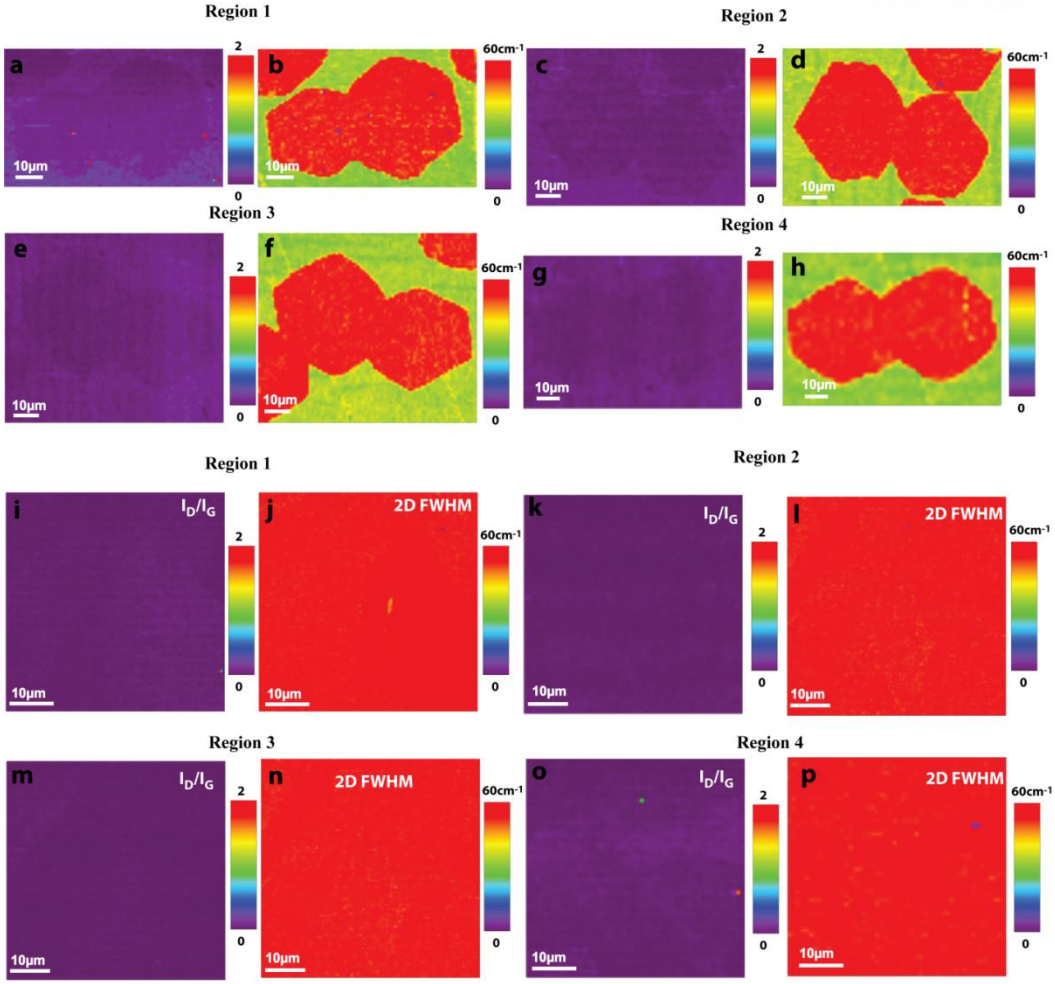

Figure 4.6. Raman mapping of bilayer graphene islands (a–h) and the continuous bilayer graphene film (i–p) at different regions. The uniformity of the Raman mapping indicates that the bilayer graphene regions we achieved are almost 100% AB-stacked, for regions over multi-centimeter areas of the Cu/Ni(111) foil.

We have also compared the bilayer graphene on Cu/Ni(111) foil with the bilayer graphene grown on polycrystalline Cu/Ni foil under the same growth conditions (**Figure 4.7**). The optical images in **Figure 4.7a-c** show that bilayer graphene grown on polycrystalline Cu/Ni foil has many non-uniform multilayer regions. The higher I_D/I_G ratio from the mapping data indicates that the bilayer graphene grown on polycrystalline Cu/Ni foil exhibits lower quality as compared to that grown on Cu/Ni(111) foil. Typical Raman spectra in **Figure 4.7b** show the comparison between AB-stacked bilayer and mis-oriented bilayer graphene samples. The Raman mapping of 2D FWHM for bilayer graphene shows many mis-oriented bilayer regions, indicating lower AB-stacked ratio (~70%) as compared to the uniform ~100% AB-stacked bilayer grown on Cu/Ni(111) foil. These results strongly indicate that single-crystalline Cu/Ni(111) foils favor the uniform AB-stacked bilayer graphene growth.

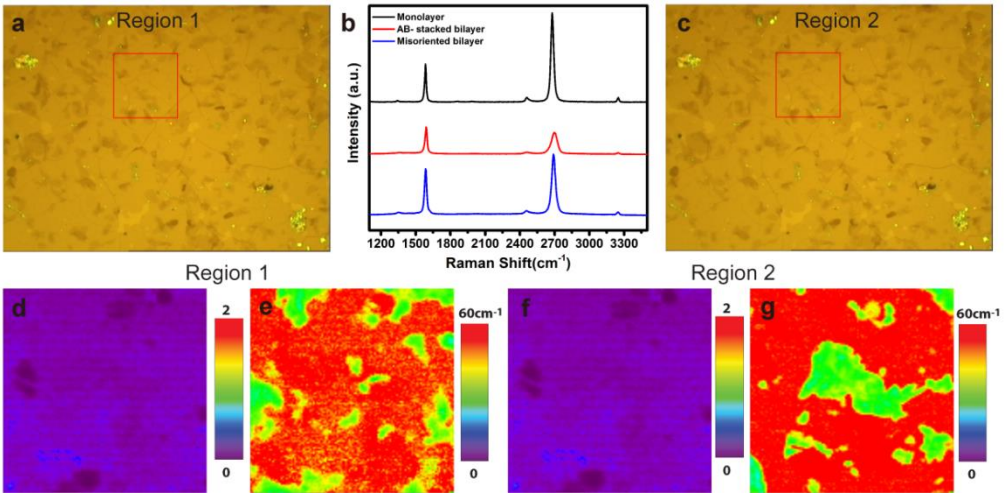

Figure 4.7. Raman mapping of bilayer graphene prepared from polycrystalline Cu/Ni alloy. (a, d, e) Optical image and Raman mapping of the bilayer graphene from region 1. (b) Typical Raman spectra of monolayer graphene, AB-stacked bilayer and misoriented bilayer graphene. (c, f, g) Optical image and Raman mapping of bilayer graphene from region 2.

Carbon solubility can be tuned by controlling the atomic fraction of Ni in Cu.[98] Recently reported works also indicate the significant effect of Ni concentration in polycrystalline Cu/Ni alloy foil on the synthesis of layer-tunable graphene films.[90] We prepared Cu/Ni(111) foils with different Ni concentrations and investigated graphene growth under the same growth conditions (1075 ℃ for 10 min; $Ar/H_2/CH_4$ (200 sccm/10 sccm/1 sccm; 40 Torr) on these substrates. **Figure 4.8** shows the optical microscopy (OM) images of as-grown graphene films transferred onto 300 nm SiO_2–on–Si substrates.

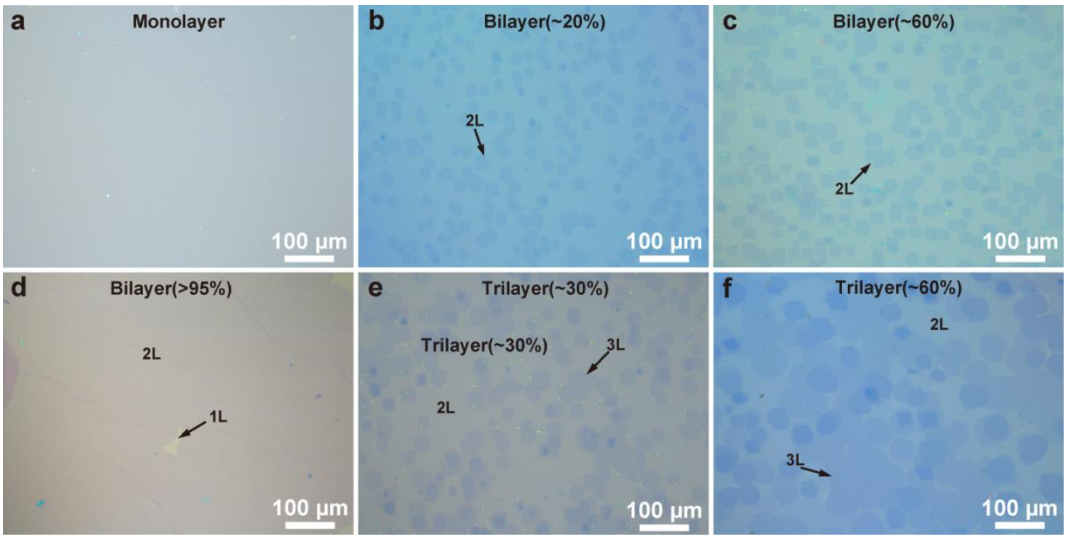

Figure 4.8. Optical images of graphene samples grown on the Cu/Ni(111) alloy with different Ni concentration: (a) 10.2 at.% Ni, (b) 12.9 at.% Ni, (c) 15.0 at.% Ni, (d) 16.6 at.% Ni, (e) 18.2 at.% Ni, and (f) 20.3 at.% Ni. The growth conditions were the same for these samples.

For the Cu/Ni(111) alloy foil with a Ni concentration of 10.2 at.%, the graphene film is monolayer (**Figure 4.8a**) and the graphene growth is mainly controlled by a surface-mediated mechanism, similar to the growth of graphene on pure Cu. This is consistent with the result from a recent study on graphene growth mechanism on polycrystalline Cu/Ni alloy foils with different Ni concentrations.[90] When the Ni concentration was increased to 12.9 at.%, bilayer graphene islands with coverage of 20% were observed (**Figure 4.8b**). A further increase of the coverage to ~60% was achieved when the Ni concentration was increased to 15.0 at.% (**Figure 4.8c**). Bilayer film with coverage of >95% was achieved with a Ni content of 16.6 at.%.

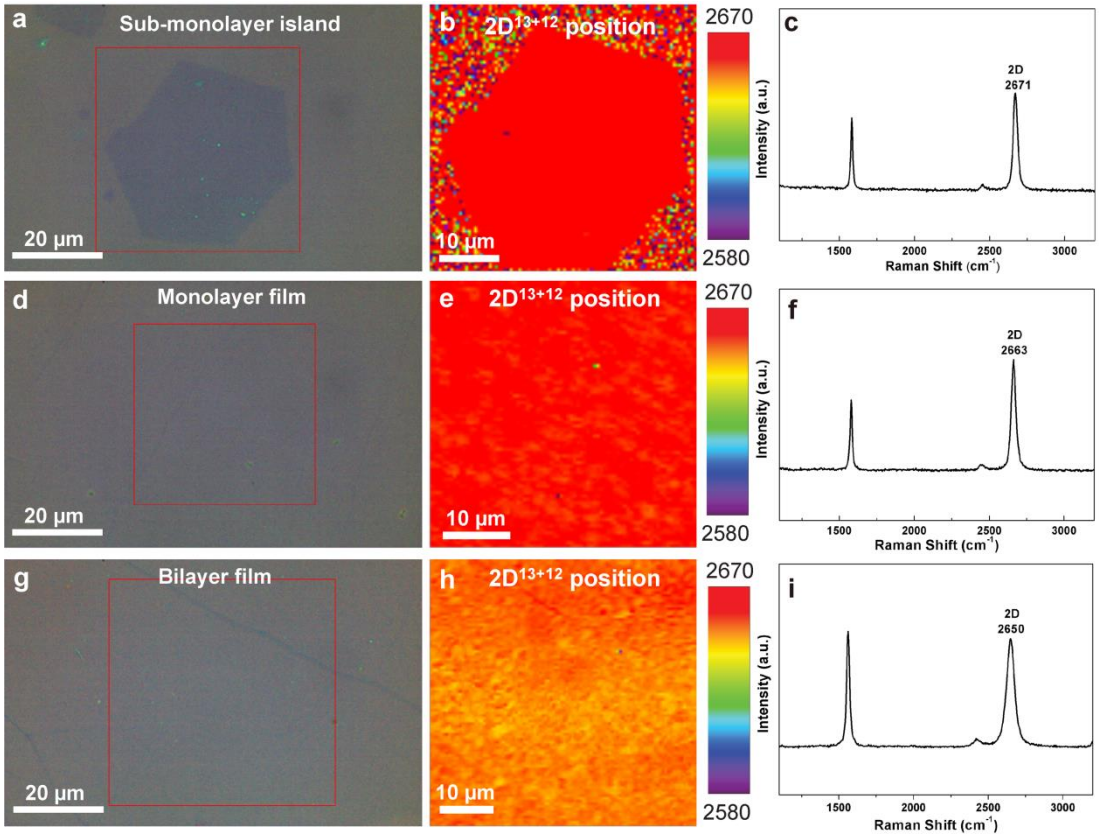

Figure 4.9. Raman mapping of $^{13}C/^{12}C$ labeled graphene (transferred onto 300-nm SiO_2-on-Si substrates) grown on Cu/Ni(111) foils (16.6 at.% Ni). (a–c), (d–f), and (g–i) are the optical images, Raman maps (2D peak position), and Raman spectra of graphene island, monolayer film, and bilayer film, respectively.

To further investigate the mechanism of growth of graphene on our Cu/Ni(111) foils, we used the carbon isotope labeling technique together with Raman spectroscopy. The isotope distribution (^{13}C and ^{12}C) can be mapped according to the different Raman mode frequencies of ^{13}C- and ^{12}C-labeled graphene.[129-130] A flow of $^{13}CH_4$ was first used at the early stage of growth after which, the gas was then switched to normal methane ($^{12}CH_4$) gasfor the further graphene growth.. After growth, the graphene was transferred onto a SiO_2-on-Si substrate and Raman mapping was done. We mapped the

2D peak position to distinguish the distribution of ^{13}C and ^{12}C species. For monolayer graphene, the 2D peak at 2580 cm^{-1} represents the signal from pure ^{13}C-labeled and that at 2680 cm^{-1} the signal from normal graphene, i.e., predominantly ^{12}C. For bilayer graphene, the 2D peak at 2590 cm^{-1} represents the signal from pure ^{13}C-labeled and that at 2690 cm^{-1} the signal from normal graphene, i.e., predominantly ^{12}C. **Figure 4.9a-f** show optical images, Raman maps of the 2D peak position, and Raman spectra of a sub-monolayer island, and a monolayer graphene film, respectively. The uniform contrast of the whole Raman map without distinguishable isotopic separation suggests that ^{13}C and ^{12}C are randomly distributed over the graphene without either locally segregated (no pure ^{13}C or pure ^{12}C region). Only one set of typical Raman peaks can be observed in both sub-monolayer island and monolayer film, which indicates the complete mixing of ^{13}C and ^{12}C atoms. These results would suggest that the graphene in the Cu/Ni(111) alloy (16.6 at.% Ni, optimized concentration for high coverage bilayer growth) was also formed through the segregation and/or precipitation mechanism. The Raman analysis of bilayer graphene film (**Figure 4.9g-i**) indeed, shows a uniform and complete mixing of ^{13}C and ^{12}C atoms, proving that the graphene present is formed by segregation/precipitation from C present in the interior of the foil, and not from 'surface-mediated' growth.

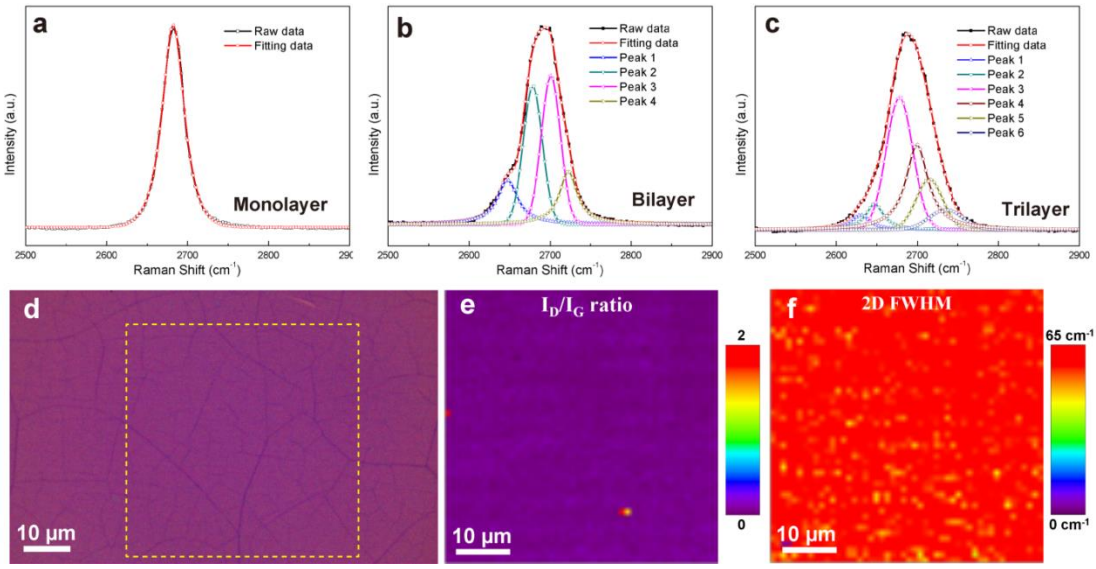

Figure 4.10. 2D Raman peaks of (a) monolayer, (b) bilayer, and (c) trilayer. The 2D peak of monolayer can be fitted by a single Lorentzian, while the bilayer and trilayer can be fitted by four and six Lorentzians, respectively. The fitting indicates that the bilayer and trilayer graphene are both AB-stacked. (d) Optical image of trilayer graphene. The region where Raman mapping was acquired is highlighted by yellow dashed line. (e, f) Raman mapping of trilayer graphene. Negligible D peaks and the uniform contrast indicates high quality, uniform ABA-stacking nature over the entire trilayer graphene region examined.

Trilayer graphene with 30% coverage was prepared when the Ni content was increased to 18.2 at.%. This is attributed to the higher amount of dissolved carbon segregated/precipitated out to the interface that forms the trilayer graphene islands. The trilayer coverage was further increased to around 60% when Ni concentration was increased to 20.3 at.% (**Figure 4.8f**). The stacking order of the trilayer graphene was analyzed by Raman peak fitting and mapping (**Figure 4.10**). The results agree well with previous Raman studies on both exfoliated ABA-stacked trilayer graphene flakes and CVD-grown trilayer graphene samples.[180-181] In some other runs with higher Ni percentage (23–28 at.% Ni), multilayer hexagonal graphene islands with 5 to 10 layers have also been achieved. **Figure 4.11** shows the corresponding optical images and Raman spectra. Identification of the layer numbers and stacking order of the graphene layers can be determined by the 2D peak position, G to 2D peak ratio, and the FWHM of the 2D peak.[40, 86, 180] The intensity of the G peak becomes more pronounced, while the FWHM of the 2D peak slightly broadens and its position is blue-shifted from that of monolayer graphene, indicating ABA-stacking of the as-prepared multilayer graphene islands.[182-183] The D band was not detected on these AB-stacked multilayer regions, demonstrating their high quality. This study shows that high coverage of high quality AB-stacked bilayer and ABA-stacked trilayer graphene can be achieved by the precise control of the Ni concentration in a single crystal Cu/Ni(111) alloy foil substrate.

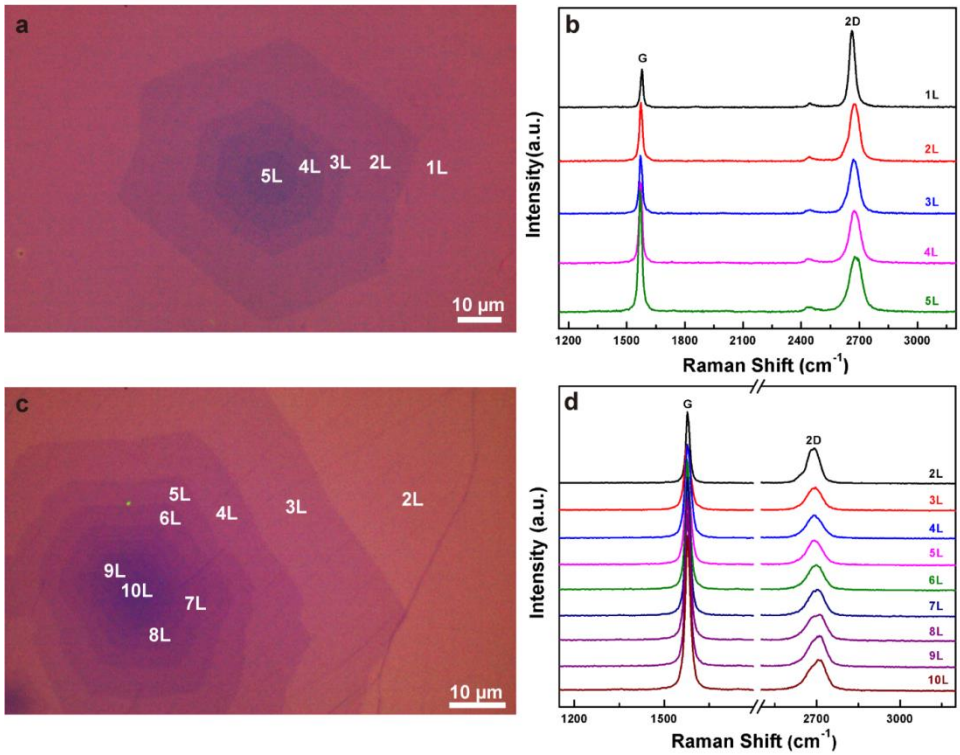

Figure 4.11. Characterization of hexagonal multilayer graphene islands. (a, b) Optical image and Raman spectra of graphene island with 5 layers. (c, d) Optical image and Raman spectra of graphene island with 10 layers.

Transmission electron microscopy (TEM) and selected area electron diffraction (SAED) measurements were carried out to examine the layer numbers and stacking order of the obtained graphene samples. **Figure 4.12a** shows the folded edge of the bilayer graphene film. The high-resolution TEM (HRTEM) images (**Figure 4.12b-c**) show no Moiré pattern with a clear lattice image, confirming AB stacking in the bilayer graphene sample. The SAED pattern (**Figure 4.12d**) exhibits only one set of hexagonal diffraction spots and the band intensity ratio (outermost to innermost) of approximately 2 (inset in **Figure 4.12d**) further suggests the formation of AB-stacked bilayer graphene. These results agree well with the features of Bernal bilayer graphene exfoliated from HOPG.[11, 86, 182] To investigate the spatial crystallographic orientation of graphene, SAED patterns were collected at different locations. The measured areas show a preferential crystal orientation for a highly uniform AB-stacked bilayer graphene. Low energy electron diffraction (LEED) was further used to characterize the crystal structures of the bilayer graphene film on Cu/Ni(111) foil (**Figure 4.13**). The consistent orientation of the LEED patterns acquired at different positions across the whole sample shows that the bilayer graphene film is not only AB-stacked in large scale, but also has a single crystalline orientation.

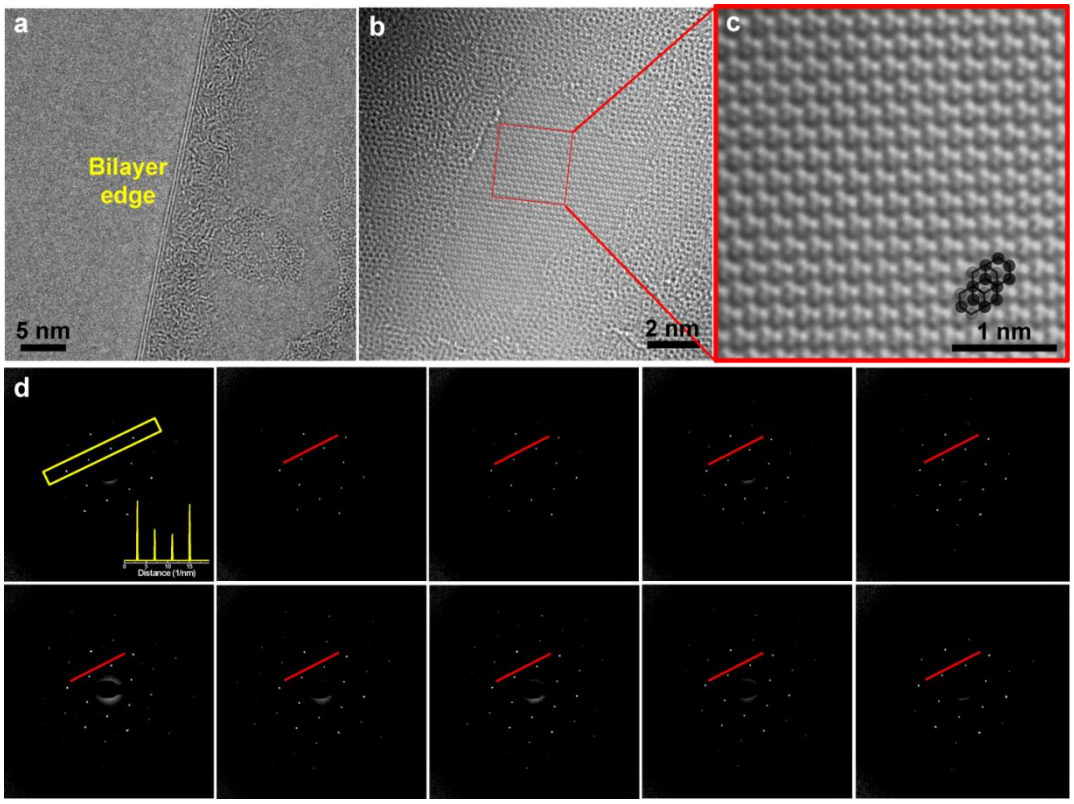

Figure 4.12. TEM analysis of the bilayer graphene film. (a) TEM image of the bilayer graphene edge that shows two layers. (b, c) HRTEM images of bilayer graphene. The AB-stacked configuration is highlighted in the magnified TEM image (c). (d) A series of SAED patterns were acquired from different regions across the 3 mm diameter TEM grid. The inset in (d) shows the intensity profile along the indicated diffraction spots.

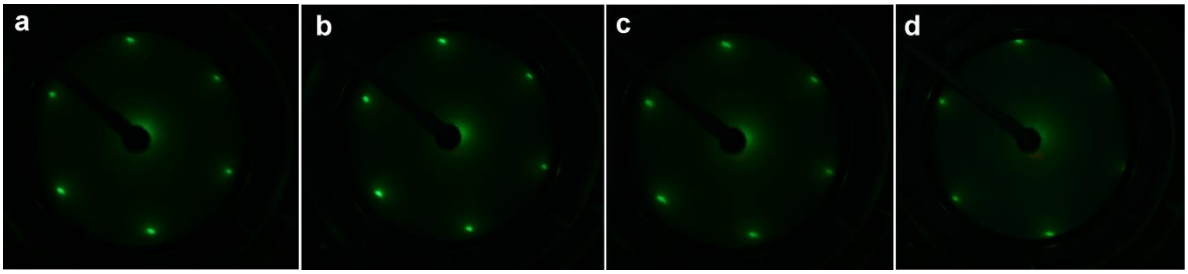

Figure 4.13. LEED measurements of the bilayer graphene coated Cu/Ni(111) foil. The LEED investigations at different positions across the whole sample prove the AB-stacked nature of bilayer graphene on a large scale.

The number of layers and uniformity of the graphene samples were further characterized by optical transmittance measurements after transferring onto glass substrates, as shown in **Figure 4.14**. The bilayer and trilayer graphene samples showed transmittances of, respectively, 95.6% and 93.2% at 550 nm wavelength, as compared to the transmittance of 97.9% for a monolayer graphene. This result is consistent with the theoretical absorption value of 2.3% and is also in agreement with values reported in a previous study.[40] The inset photograph shows the transferred graphene films on the glass substrate. The difference in the number of layers can be readily observed by the difference in the optical contrast among the three samples. In addition, there is no obvious difference in the contrast of the transferred graphene film on the whole glass substrate, further confirming the uniformity of the graphene samples.

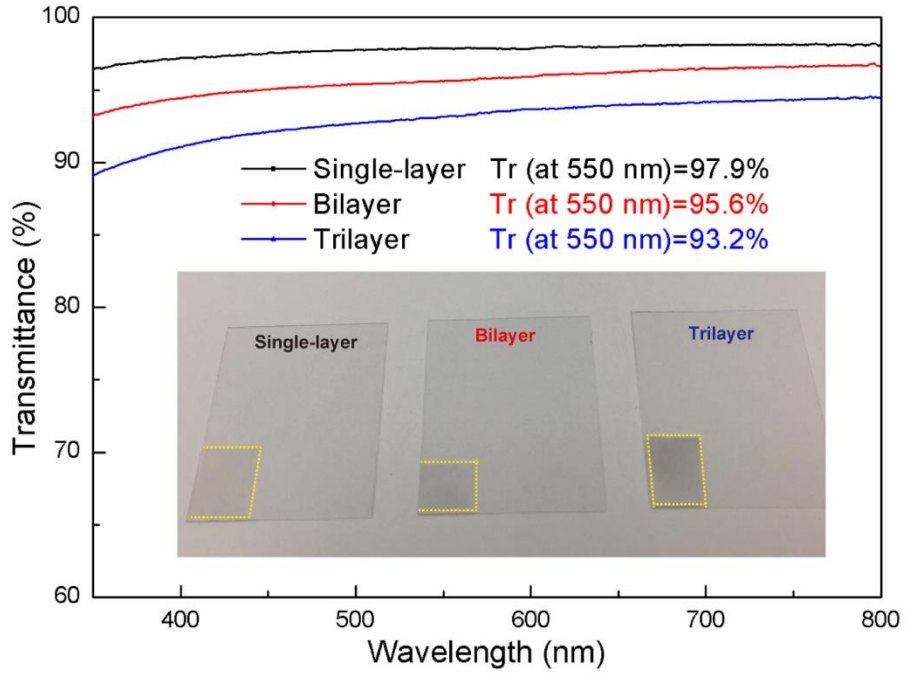

Figure 4.14. Transmittance of single-, bi- and tri-layer graphene films tested on glass. The inset shows the photographs of the graphene samples with different layer numbers.

4.4 Layer structure in bilayer/multilayer graphene grown on Cu/Ni(111) foil

Determining the structure of the adlayers relative to the first layer is key to understanding the growth mechanism. In our previous work, ToF-SIMS depth profiling and mapping were used to image the carbon distribution so as to assign the stacking sequence of the adlayer graphene.[184] This technique involves layer-by-layer removal of graphene layers and mapping of the C signal. Since the size of each layer is different, the stacking sequence can be determined by examining the change in size of the graphene layers after removing the top layer graphene with the Cs^+ ion beam.

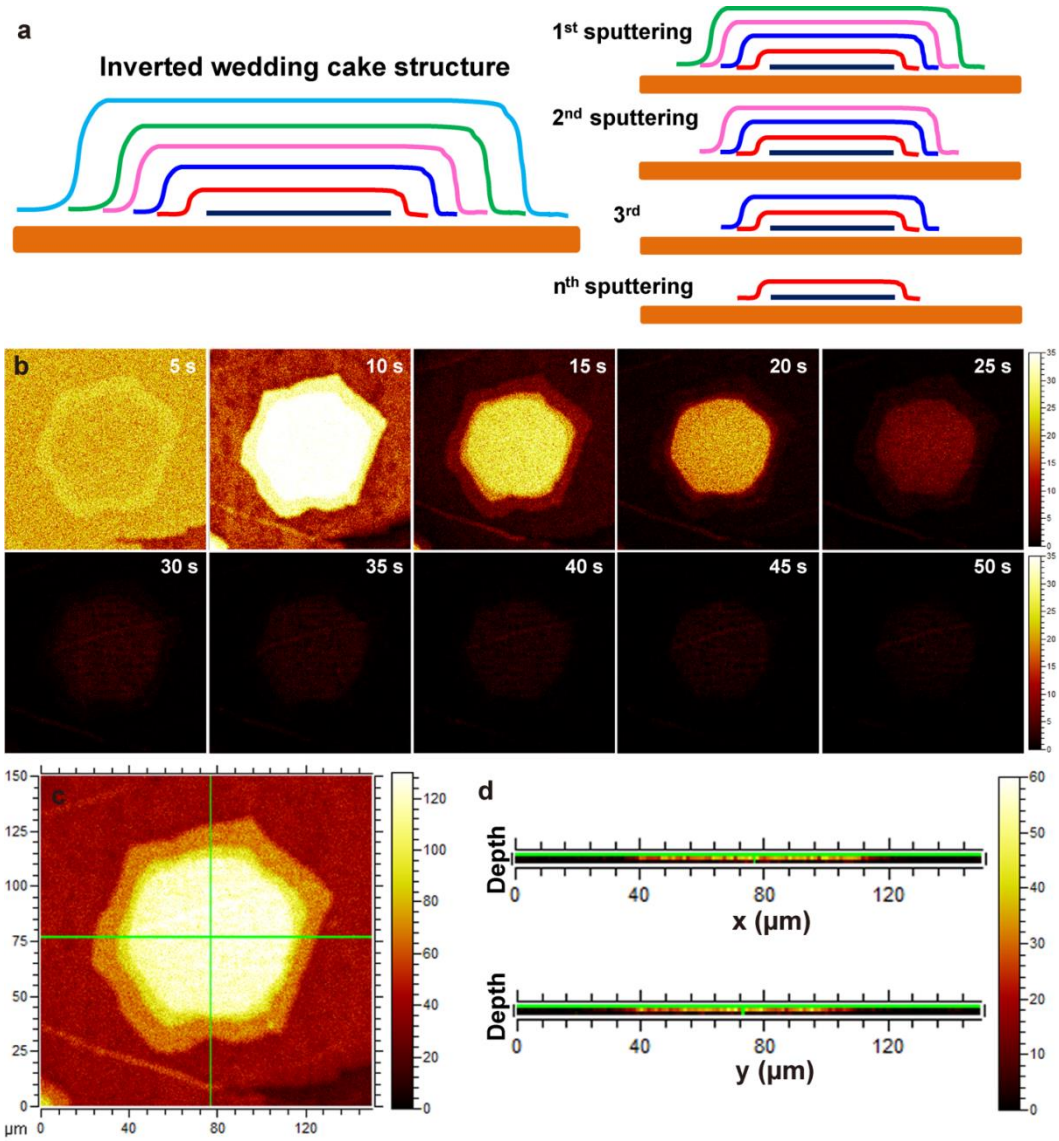

Figure 4.15. ToF-SIMS mapping (150 μm × 150 μm) of multilayer graphene islands on 300-nm SiO_2 on Si substrates. (a) The schematic shows the ToF-SIMS sputtering process of the multilayer graphene. (b) The carbon distribution images of graphene after 1 kV Cs^+ ion beam sputtering for different periods of time. (c) The overall overlapped image from 30 images. (d) Cross-sectional views of carbon intensity from the x-z and y-z directions as shown in (c).

Figure 4.15 shows the SIMS mapping of C after ion beam sputtering with different times, where the top-down maps clearly show that the graphene was removed approximately layer-by-layer. The observed C signal was very weak even after the first sputtering cycle, which may be due to the presence of adsorbed impurities on the sample surface during the transfer process and from exposure to air. Cs^+ sputtering during several seconds of was used to remove contaminants before the start of etching of the outermost graphene layer. After 18 s of Cs^+ sputtering, the first layer (outermost layer) became visible (higher secondary ion intensity). The outermost layer was removed after around 36 s sputtering, while the second layer (underneath the outermost layer) was removed after 54 s sputtering. As the outer layers were removed, the underlying adlayers were detected. A small hexagonal adlayer was not visible during the first 5 sputtering cycles (45 s), while it became visible after 81 s sputtering and was partially etched at the end of the sputtering process. This shows that the smaller adlayer was screened (protected) by the larger top layers, and that it was accessible to etching by the Cs^+ beam only after removing the top graphene layers. The overall sum image shows the edges from all the adlayers (**Figure 4.15b**). The cross-sectional image (**Figure 4.15c**) from the x-z and y-z directions clearly shows that the adlayers grow beneath the first continuous monolayer graphene, forming an "inverted wedding cake" (IWC) structure.

In situ environmental scanning electron microscopy (E-SEM) has been demonstrated as an effective tool for studying graphene growth kinetics and revealing adlayer structure when combined with hydrogen etching.[178, 185-186] Here we used this in situ E-SEM technique together with hydrogen etching to determine the structure of the adlayers of graphene grown on Cu/Ni(111) foils. The shape evolution of monolayer and bilayer graphene regions during hydrogen etching is shown in **Figure 4.16**. The designated areas (one monolayer region and three multilayer regions) in **Figure 4.16a-g** were extracted and replotted in **Figure 4.16h**. It is apparent that the bilayer does not etch until the etching front of the first layer (monolayer) approaches to the edge of the bilayer region (the distance is around 2.3 μm), indicating the presence of a buried layer (screening effect/protection of the top layer). This result is thus different from a study using a similar approach described in the literature, where simultaneous etching of the multilayer graphene that had been grown on Pt foil suggested a wedding cake (WC) structure for the stacked layers.[178] Hence in our work reported here, the smaller bilayer graphene grows underneath the larger continuous monolayer, demonstrating that the CVD growth of bilayer (multilayer) graphene on the Cu/Ni(111) foils here follows the IWC type stacking. The evolution of the perimeter and area of the graphene (monolayer region 4 and bilayer region 1 and 2) during etching are plotted in **Figure 4.17**. We found that the etching of the bilayer region 1 started approximately from 758.8 s and that of the bilayer region 2 started from 1084 s, both corresponding to a distance around 2.3 μm with regard to the etching front of the continuous monolayer. The perimeter and the area were linearly and quadratically fitted; this trend agrees well with a detachment-limited etching process following first-order kinetics.[187] The line slopes in **Figure 4.17a** correspond to the

averaged etching rates of the respective layers in **Figure 4.16a**. They are 15.5 nm s^{-1} (etched hole for the monolayer region) for the first layer (region 4, monolayer), -4.5 nm s^{-1} for the left second layer (bilayer region 1), and -3.1 nm s^{-1} for the right second layer (bilayer region 2). The difference in etching rate between the first and second layer further indicates the IWC-like stacking. Here we also found the etching rate for the left second layer is about 1.5 times of that of the right second layer, which is more or less consistent with the difference in the distance to the etching front of the first layer. This indicates that the 'out diffusion' of etching products from graphene edges (bilayer) is thus hindered by the presence of the top first layer, further demonstrating the IWC stacking sequence of the bilayer/multilayer graphene grown on the Cu/Ni(111) foil.

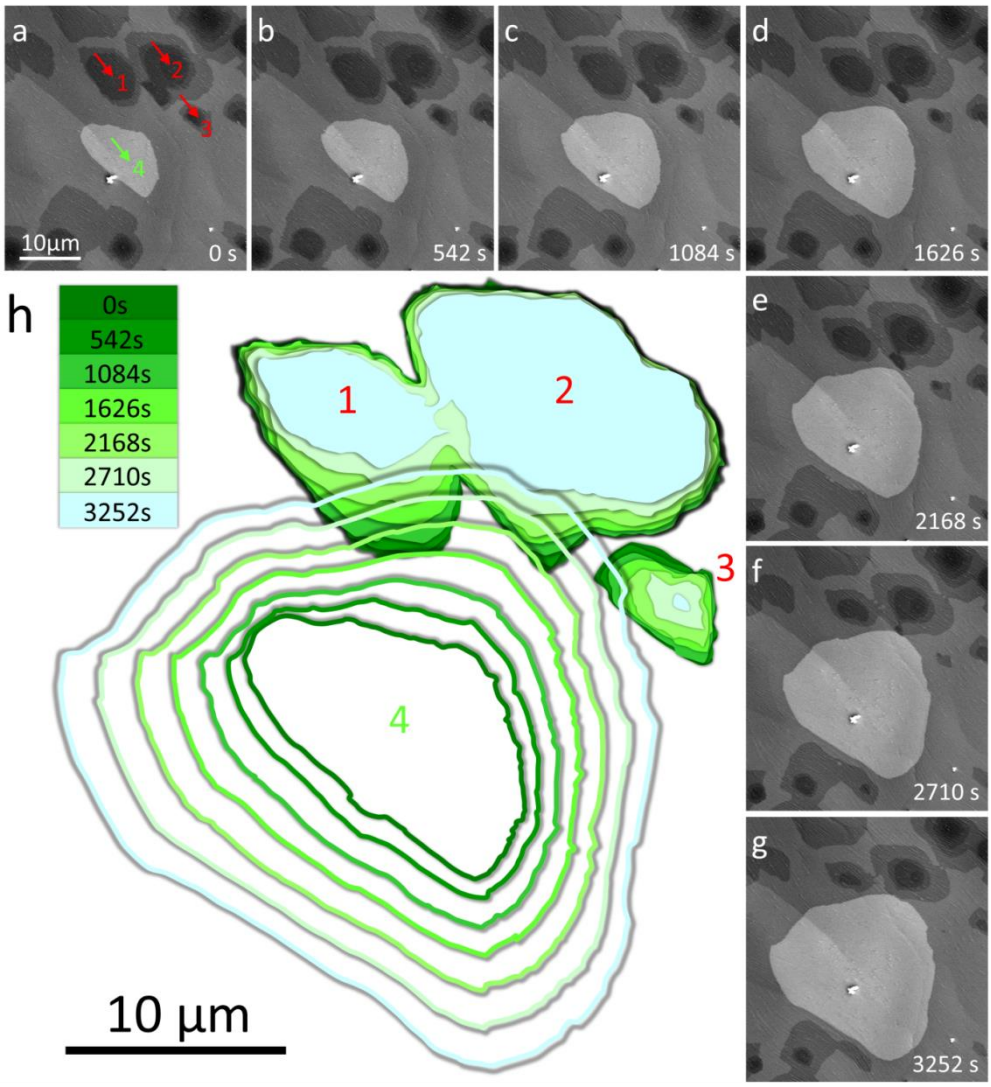

Figure 4.16. In situ scanning electron microscopy observation of graphene etching. (a–g) Time-lapse image series showing the etching of vacancy islands and the topmost layers in SLG and BLG. (h) Shape evolution of the respective layers during etching, reproduced as color-coded superposition of outlines that were extracted from images (a–g). Red arrows highlight second layer graphene events. The green arrow indicates etching of vacancy islands in SLG.

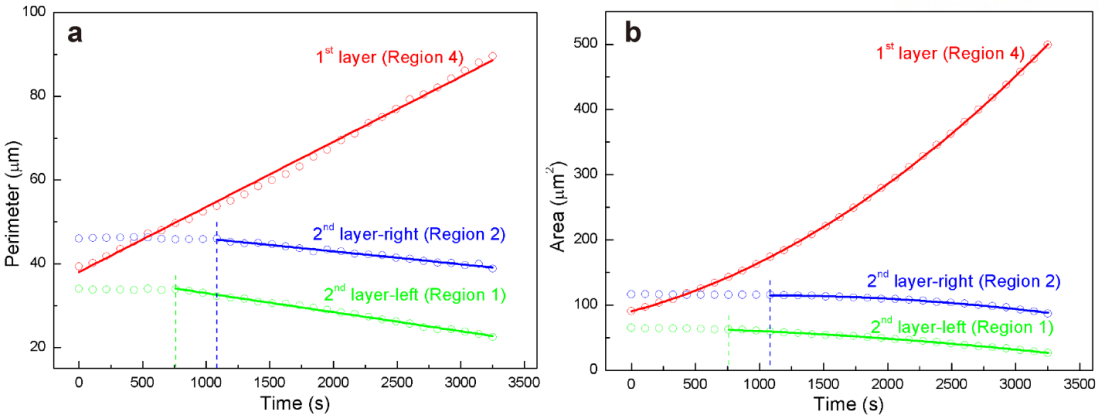

Figure 4.17. Changes in the graphene layers during H_2 etching. (a) Evolution of the perimeters of the first layer (region 4), right second layer (region 2), and left second layer (region 1) and linear fits. (b) Evolution of the areas of the first layer (region 4), right second layer (region 2), and left second layer (region 1) with corresponding quadratic fits.

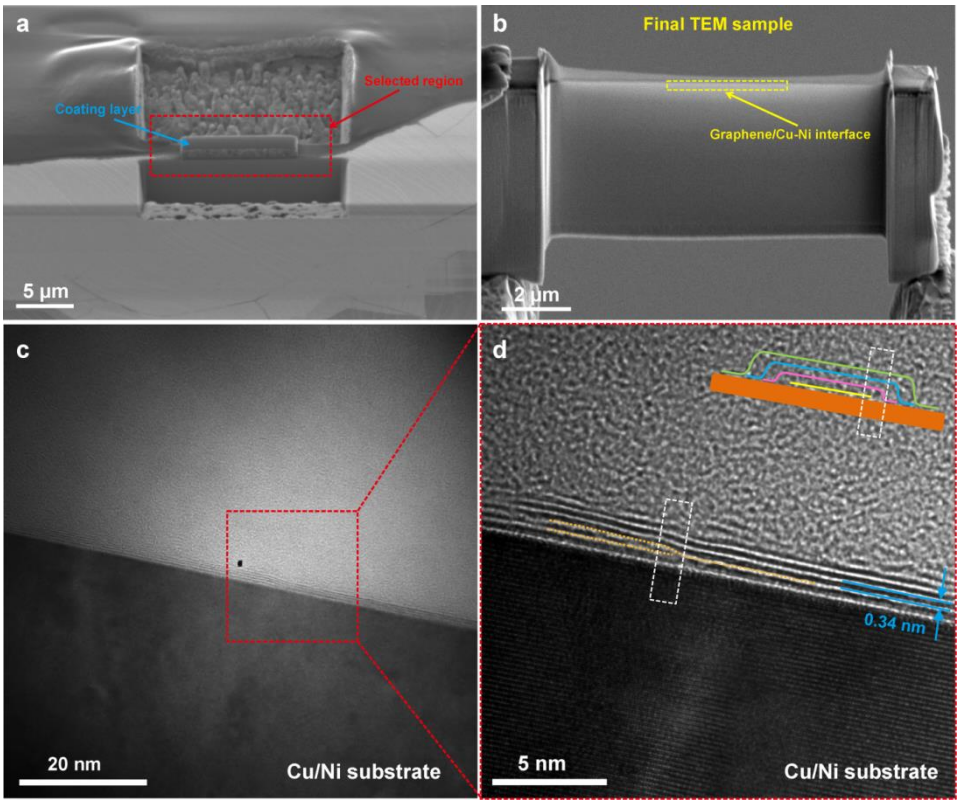

Figure 4.18. (a, b) SEM images of the different steps in the focused ion beam milling process used to fabricate the TEM sample. (c) Low-magnification TEM image of multilayer graphene islands (with a full coverage of monolayer graphene) on Cu/Ni(111) alloy. (d) HRTEM image of the region as marked in (c). The inset schematic shows the edge region of the bottom layer and the layer above it. It is observed that the bottom island is covered with a larger graphene sheet (layer above the bottom layer; the 'inverted wedding cake' structure).

Cross-sectional TEM was also used to study the stacking sequence of graphene layers through a 'side view' of the multilayer graphene/alloy interface. The sample was prepared by the focused ion beam milling process (**Figure 4.18a-b**). The final TEM sample with thickness less than 100 nm was obtained after gentle polishing. Low-magnification cross-sectional TEM image (**Figure 4.18c**) shows multilayer graphene sheets with 3–4 layers. The corresponding HRTEM image is shown in **Figure 4.18d**. The inset of the schematic shows the edge of the bottom layer and the layer above it. It is observed that the bottom island (smaller) is covered with a larger graphene sheet (layer above the bottom layer), indicating an IWC structure.

Table 4.1. Statistics of carrier mobility from the GFET devices for bilayer graphene.

Device number	Hole mobility ($cm^2 V^{-1} s^{-1}$)	Electron mobility ($cm^2 V^{-1} s^{-1}$)
1	2917	2567
2	1696	1672
3	3679	3163
4	2260	2147
5	3785	3933
6	3352	3560
7	3525	3551
8	3191	2772
9	3552	3150
10	4550	4788
11	3487	3910
12	4913	4549
13	5053	4870
14	5298	5090
15	5250	5410
16	5264	5029
17	5668	5540

Transport measurements were carried out using the back-gated graphene field effect transistors (GFETs) which were prepared by transferring the AB-stacked bilayer graphene onto a 300 nm thick SiO_2/Si substrate (**Figure 4.19a**). A typical gate-dependent conductance plot and the statistics of the carrier mobility are shown in **Figure 4.19b** and **Table 4.1**. The average room-temperature carrier mobilities extracted from measurements on over 17 devices were 3967 $cm^2 V^{-1} s^{-1}$ for holes and 3865 $cm^2 V^{-1} S^{-1}$ for electrons, which are comparable to values reported in the literature for the CVD-grown bilayer graphene and exfoliated bilayer graphene[1, 31-33].[161, 188-190] The

electrical transport measurements thus demonstrate the high quality of the as-synthesized AB-stacked graphene.

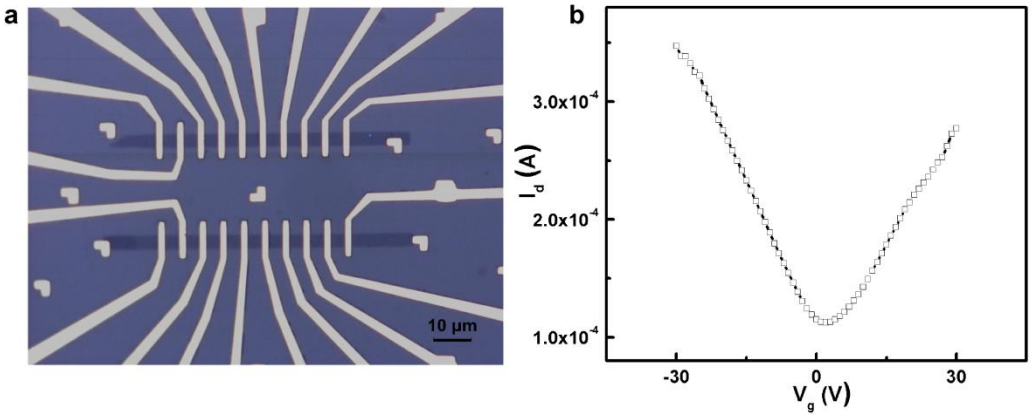

Figure 4.19. Electrical transport measurement on bilayer graphene. (a) Optical microscopy image of a FET device on a 300-nm SiO_2-on-Si substrate. (b) Transport property of the device measured at room temperature.

4.5 Conclusion

In summary, we have for the first time, prepared large-area single crystal Cu/Ni(111) alloy foils by heat-treating Ni-plated Cu(111) foils. By precisely controlling the Ni content in the alloy, large-area AB-stacked bilayer graphene with coverage of more than 95% and trilayer graphene with more than 60% coverage have been achieved. We have investigated the growth mechanism of graphene on Cu/Ni(111) by carbon isotope labeling (sequential dosing of $^{13}CH_4$ and normal CH_4 (predominantly ^{12}C) and Raman mapping. The data show that graphene grown on the Cu/Ni(111) alloy (optimized Ni concentration (16.6 at.% Ni) for high bilayer coverage) grows by segregation and/or precipitation. We further investigated layer stacking in bilayer/multilayer graphene using a combination of characterization techniques including ToF-SIMS mapping, hydrogen etching with *in situ* SEM imaging, and cross-sectional HRTEM imaging. We find that the adlayer regions of the bilayer, trilayer, and multilayer graphene regions grow beneath the top monolayer graphene film, i.e., the graphene layers are stacked in the form of an inverted wedding cake (IWC). This work introduces a method to synthesize large-area AB-stacked bilayer or trilayer graphene with high coverage. The characterization and findings in this study provide an in-depth understanding of graphene layer structure and the growth of bilayer and trilayer graphene on these new types of metal foils.

#Manuscript Preparation

Chapter 5 Conclusions and future research directions

5.1 Conclusions

In order to further improve the graphene quality and control the layer number, we have used single crystal Cu/Ni(111) foil as the substrates for the graphene growth. These single crystal Cu/Ni(111) foils were made through an electroplating method followed by an annealing process. The ability to tune the concentration of Ni in the Cu/Ni(111) foil enables the controllable growth of high quality graphene films with different layer numbers.

By controlling the bulk Ni concentration below 10.0 at.%, we have achieved fast-growth of single crystal monolayer graphene film in 5 min or less as compared to 60 min for a pure Cu(111) foil under identical growth conditions. We demonstrated a superstructure at the surface of these foils with stoichiometry of Cu_6Ni_1 for a range of compositions (1.3 to 7.8 bulk at.% Ni) in the Cu/Ni(111) foil (discovered by LEED). The as-prepared graphene in our work has been characterized by various techniques, such as OM, SEM, AFM, TEM, POM, Raman, indicating a very high quality and uniformity in large scale. In addition, we have observed and studied the graphene folds in continuous graphene and joined graphene islands with high magnification SEM and aberration-corrected high-resolution TEM as well as AFM, STM, and optical microscopy. The folds occur due to the buildup of interfacial compressive stress (and its release) during cooling of the foils from 1075 ℃ to room temperature. By using the electrochemical delamination method, the Cu/Ni(111) foils can be reused many times for the growth of equally high quality graphene without any apparent degradation of the foils.

Furthermore, we have achieved large-area, high quality bilayer and tri-layer graphene films by CVD; these films are almost entirely ‘AB-stacked’. The number of layers in the graphene films was controlled by finely tuning the Ni concentration in the alloy foil. ToF-SIMS mapping, hydrogen etching with *in situ* SEM, and cross-sectional HRTEM imaging all show that the second-layer (the ‘adlayer’; and thus also the 3rd layer and so on) grows underneath the first layer, forming an ‘inverted wedding cake’ structure.The graphene growth mechanism on the Cu/Ni(111) foils with high Ni concentration (16.6 at.% bulk Ni) are also presented and discussed.

5.2 Future research directions

1. Very high Ni content Cu/Ni(111) foils, and “Ni/Cu(111)” foils

Currently, we can prepare large area graphene with layers up to 3. However, we are aiming to prepare large area graphite films with layer numbers in the range 30–100 or more. In this case, we need to increase the Ni concentration by adding more Ni into the Cu(111) foil. Two ways to increase the Ni concentration can be considered, one is multiple Ni plating processes (Ni plating followed by annealing, repeating this process several times) onto a previously prepared Cu(111) foil; the other

could be Cu plating onto Ni(111) foil (our group has also successfully generated Ni(111) foils). In both cases, I will assess the 'quality' of the final alloy foil (crystallinity and surface roughness), which are both likely to be crucial for the subsequent graphene growth.

2. Large single-crystalline multilayer graphene growth on Cu/Ni(111) foil

As we have already achieved large area monolayer and relatively large area bilayer graphene film regions on Cu/Ni(111) foils, the next challenge is the growth of large size single crystalline multilayer graphene, which has not yet been reported. We can adjust the carbon solubility in our home-made Cu/Ni(111) alloy foil by precisely controlling the Ni concentration in the bulk Cu/Ni(111) foil. I think that a systematic investigation of multilayer growth as a function of Ni concentration is needed to try to tune the layer number and achieve large area n-layer single crystal regions. To achieve a large single-crystalline multilayer graphene with control of n from 3 to higher numbers, I need to decrease the nucleation density (by applying a shower configuration for local feeding of carbon precursor) and also decrease the growth rate for the first layer, which would then increase the grain size of the adlayer regions. This is because as long as the foil is not completely covered with the monolayer that is probably in the process of formation at the reaction temperature, more carbon diffusion into Cu/Ni(111) alloy can occur to enable adlayer growth; the adlayer can also grow during the cooling down of the foil, and this aspect should also be investigated in depth.

3. Ordered porous graphite (graphenic carbon surface coating) growth on porous Cu/Ni foil

To date, various templates have been employed to prepare porous graphene materials, but these porous graphene frameworks possess a disordered pore structure with pore sizes ranging from a few nanometers to several tens of micrometers, which will inevitably influence mass transport and thereby deteriorate device performance. The synthesis of 2D porous graphite thin films with well-defined porosity and precisely controlled smaller pore sizes (a few micrometers to hundreds of nanometers) has not yet been realized. Regarding our current study on the preparation of Cu/Ni(111) foils with tunable Ni content for high quality graphene films growth, I intend to explore the fabrication of porous Cu/Ni foils to enable porous graphite film growth. As an attempt to prepare promising ordered porous Cu/Ni foil for porous graphite growth, we propose a template-assisted electroplating process for porous Ni film deposition onto Cu(111) foil. After removing of the template, further alloying would transform the porous Ni film deposited Cu(111) foil into porous Cu/Ni foil. There are some top down patterning approaches that I can try as well, such as, lithography and electrochemical etching. This could leave an array of micron-scale or nanoscale "pores" depending on the technique used for etching (electrochemical etching attempts or wet chemical etching, or perhaps dry etching). How carbon "deposits" on these ordered porous Cu/Ni substrates (either from gas phase CVD or by precipitation from the bulk of the foil) might be very interesting.

References

1. Jo, S. B.; Park, J.; Lee, W. H.; Cho, K.; Hong, B. H., Large-area graphene synthesis and its application to interface-engineered field effect transistors. *Solid State Communications* **2012,** *152* (15), 1350-1358.

2. Batzill, M., The surface science of graphene: Metal interfaces, CVD synthesis, nanoribbons, chemical modifications, and defects. *Surface Science Reports* **2012,** *67* (3-4), 83-115.

3. Geim, A. K., Graphene: status and prospects. *science* **2009,** *324* (5934), 1530-1534.

4. Dreyer, D. R.; Ruoff, R. S.; Bielawski, C. W., From conception to realization: an historial account of graphene and some perspectives for its future. *Angewandte Chemie International Edition* **2010,** *49* (49), 9336-9344.

5. Liu, Y.; Weiss, N. O.; Duan, X.; Cheng, H.-C.; Huang, Y.; Duan, X., Van der Waals heterostructures and devices. *Nature Reviews Materials* **2016,** *1* (9), 16042.

6. Zhang, Y.; Tan, Y.-W.; Stormer, H. L.; Kim, P., Experimental observation of the quantum Hall effect and Berry's phase in graphene. *nature* **2005,** *438* (7065), 201.

7. Bolotin, K. I.; Sikes, K.; Jiang, Z.; Klima, M.; Fudenberg, G.; Hone, J.; Kim, P.; Stormer, H., Ultrahigh electron mobility in suspended graphene. *Solid State Communications* **2008,** *146* (9-10), 351-355.

8. Lee, C.; Wei, X.; Kysar, J. W.; Hone, J., Measurement of the elastic properties and intrinsic strength of monolayer graphene. *science* **2008,** *321* (5887), 385-388.

9. Stoller, M. D.; Park, S.; Zhu, Y.; An, J.; Ruoff, R. S., Graphene-based ultracapacitors. *Nano letters* **2008,** *8* (10), 3498-3502.

10. Balandin, A. A.; Ghosh, S.; Bao, W.; Calizo, I.; Teweldebrhan, D.; Miao, F.; Lau, C. N., Superior thermal conductivity of single-layer graphene. *Nano letters* **2008,** *8* (3), 902-907.

11. Nair, R. R.; Blake, P.; Grigorenko, A. N.; Novoselov, K. S.; Booth, T. J.; Stauber, T.; Peres, N. M.; Geim, A. K., Fine structure constant defines visual transparency of graphene. *science* **2008,** *320* (5881), 1308-1308.

12. Ghany, N. A. A.; Elsherif, S. A.; Handal, H. T., Revolution of Graphene for different applications: State-of-the-art. *Surfaces and Interfaces* **2017,** *9*, 93-106.

13. Lu, X.; Yu, M.; Huang, H.; Ruoff, R. S., Tailoring graphite with the goal of achieving single sheets. *Nanotechnology* **1999,** *10* (3), 269.

14. Lu, X.; Huang, H.; Nemchuk, N.; Ruoff, R. S., Patterning of highly oriented pyrolytic graphite by oxygen plasma etching. *Applied Physics Letters* **1999,** *75* (2), 193-195.

15. Novoselov, K. S.; Geim, A. K.; Morozov, S. V.; Jiang, D.; Zhang, Y.; Dubonos, S. V.; Grigorieva, I. V.; Firsov, A. A., Electric field effect in atomically thin carbon films. *science* **2004,** *306* (5696), 666-669.

16. Parvez, K.; Yang, S.; Feng, X.; Müllen, K., Exfoliation of graphene via wet chemical routes.

Synthetic Metals **2015,** *210*, 123-132.

17. Ciesielski, A.; Samorì, P., Graphene via sonication assisted liquid-phase exfoliation. *Chemical Society Reviews* **2014,** *43* (1), 381-398.

18. Hernandez, Y.; Nicolosi, V.; Lotya, M.; Blighe, F. M.; Sun, Z.; De, S.; McGovern, I.; Holland, B.; Byrne, M.; Gun'Ko, Y. K., High-yield production of graphene by liquid-phase exfoliation of graphite. *Nature nanotechnology* **2008,** *3* (9), 563.

19. Su, C.-Y.; Lu, A.-Y.; Xu, Y.; Chen, F.-R.; Khlobystov, A. N.; Li, L.-J., High-quality thin graphene films from fast electrochemical exfoliation. *ACS nano* **2011,** *5* (3), 2332-2339.

20. Wang, J.; Manga, K. K.; Bao, Q.; Loh, K. P., High-yield synthesis of few-layer graphene flakes through electrochemical expansion of graphite in propylene carbonate electrolyte. *Journal of the American Chemical Society* **2011,** *133* (23), 8888-8891.

21. Liu, J.; Poh, C. K.; Zhan, D.; Lai, L.; Lim, S. H.; Wang, L.; Liu, X.; Sahoo, N. G.; Li, C.; Shen, Z., Improved synthesis of graphene flakes from the multiple electrochemical exfoliation of graphite rod. *Nano Energy* **2013,** *2* (3), 377-386.

22. Parvez, K.; Li, R.; Puniredd, S. R.; Hernandez, Y.; Hinkel, F.; Wang, S.; Feng, X.; Müllen, K., Electrochemically exfoliated graphene as solution-processable, highly conductive electrodes for organic electronics. *ACS nano* **2013,** *7* (4), 3598-3606.

23. Yu, P.; Lowe, S. E.; Simon, G. P.; Zhong, Y. L., Electrochemical exfoliation of graphite and production of functional graphene. *Current Opinion in Colloid & Interface Science* **2015,** *20* (5-6), 329-338.

24. Bai, H.; Li, C.; Shi, G., Functional composite materials based on chemically converted graphene. *Advanced Materials* **2011,** *23* (9), 1089-1115.

25. Hummers Jr, W. S.; Offeman, R. E., Preparation of graphitic oxide. *Journal of the American Chemical Society* **1958,** *80* (6), 1339-1339.

26. Stankovich, S.; Dikin, D. A.; Piner, R. D.; Kohlhaas, K. A.; Kleinhammes, A.; Jia, Y.; Wu, Y.; Nguyen, S. T.; Ruoff, R. S., Synthesis of graphene-based nanosheets via chemical reduction of exfoliated graphite oxide. *carbon* **2007,** *45* (7), 1558-1565.

27. Li, D.; Müller, M. B.; Gilje, S.; Kaner, R. B.; Wallace, G. G., Processable aqueous dispersions of graphene nanosheets. *Nature nanotechnology* **2008,** *3* (2), 101.

28. Cassagneau, T.; Fendler, J. H., Preparation and layer-by-layer self-assembly of silver nanoparticles capped by graphite oxide nanosheets. *The Journal of Physical Chemistry B* **1999,** *103* (11), 1789-1793.

29. Fan, X.; Peng, W.; Li, Y.; Li, X.; Wang, S.; Zhang, G.; Zhang, F., Deoxygenation of exfoliated graphite oxide under alkaline conditions: a green route to graphene preparation. *Advanced Materials* **2008,** *20* (23), 4490-4493.

30. Chen, X.; Li, W.; Luo, D.; Huang, M.; Wu, X.; Huang, Y.; Lee, S. H.; Chen, X.; Ruoff, R. S.,

Controlling the thickness of thermally expanded films of graphene oxide. *ACS nano* **2016,** *11* (1), 665-674.

31. Badami, D., X-ray studies of graphite formed by decomposing silicon carbide. *carbon* **1965,** *3* (1), 53-57.

32. Van Bommel, A.; Crombeen, J.; Van Tooren, A., LEED and Auger electron observations of the SiC (0001) surface. *Surface Science* **1975,** *48* (2), 463-472.

33. Berger, C.; Song, Z.; Li, T.; Li, X.; Ogbazghi, A. Y.; Feng, R.; Dai, Z.; Marchenkov, A. N.; Conrad, E. H.; First, P. N., Ultrathin epitaxial graphite: 2D electron gas properties and a route toward graphene-based nanoelectronics. *The Journal of Physical Chemistry B* **2004,** *108* (52), 19912-19916.

34. Kusunoki, M.; Suzuki, T.; Hirayama, T.; Shibata, N.; Kaneko, K., A formation mechanism of carbon nanotube films on SiC (0001). *Applied Physics Letters* **2000,** *77* (4), 531-533.

35. Emtsev, K. V.; Bostwick, A.; Horn, K.; Jobst, J.; Kellogg, G. L.; Ley, L.; McChesney, J. L.; Ohta, T.; Reshanov, S. A.; Röhrl, J., Towards wafer-size graphene layers by atmospheric pressure graphitization of silicon carbide. *Nature materials* **2009,** *8* (3), 203.

36. Norimatsu, W.; Kusunoki, M., Epitaxial graphene on SiC {0001}: advances and perspectives. *Physical Chemistry Chemical Physics* **2014,** *16* (8), 3501-3511.

37. Robertson, S., Graphite formation from low temperature pyrolysis of methane over some transition metal surfaces. *nature* **1969,** *221* (5185), 1044.

38. Shelton, J.; Patil, H.; Blakely, J., Equilibrium segregation of carbon to a nickel (111) surface: A surface phase transition. *Surface Science* **1974,** *43* (2), 493-520.

39. Somani, P. R.; Somani, S. P.; Umeno, M., Planer nano-graphenes from camphor by CVD. *Chemical Physics Letters* **2006,** *430* (1-3), 56-59.

40. Reina, A.; Jia, X.; Ho, J.; Nezich, D.; Son, H.; Bulovic, V.; Dresselhaus, M. S.; Kong, J., Large area, few-layer graphene films on arbitrary substrates by chemical vapor deposition. *Nano letters* **2008,** *9* (1), 30-35.

41. Li, X.; Cai, W.; An, J.; Kim, S.; Nah, J.; Yang, D.; Piner, R.; Velamakanni, A.; Jung, I.; Tutuc, E., Large-area synthesis of high-quality and uniform graphene films on copper foils. *science* **2009,** *324* (5932), 1312-1314.

42. Banszerus, L.; Schmitz, M.; Engels, S.; Dauber, J.; Oellers, M.; Haupt, F.; Watanabe, K.; Taniguchi, T.; Beschoten, B.; Stampfer, C., Ultrahigh-mobility graphene devices from chemical vapor deposition on reusable copper. *Science advances* **2015,** *1* (6), e1500222.

43. Yu, H. K.; Balasubramanian, K.; Kim, K.; Lee, J.-L.; Maiti, M.; Ropers, C.; Krieg, J.; Kern, K.; Wodtke, A. M., Chemical vapor deposition of graphene on a "peeled-off" epitaxial cu (111) foil: A simple approach to improved properties. *ACS nano* **2014,** *8* (8), 8636-8643.

44. Miseikis, V.; Bianco, F.; David, J.; Gemmi, M.; Pellegrini, V.; Romagnoli, M.; Coletti, C., Deterministic patterned growth of high-mobility large-crystal graphene: a path towards wafer scale

integration. *2D Materials* **2017,** *4* (2), 021004.

45. Fang, W.; Hsu, A. L.; Song, Y.; Kong, J., A review of large-area bilayer graphene synthesis by chemical vapor deposition. *Nanoscale* **2015,** *7* (48), 20335-20351.

46. Sung, C.-M.; Tai, M.-F., Reactivities of transition metals with carbon: implications to the mechanism of diamond synthesis under high pressure. *International Journal of Refractory Metals and Hard Materials* **1997,** *15* (4), 237-256.

47. Yu, Q.; Lian, J.; Siriponglert, S.; Li, H.; Chen, Y. P.; Pei, S.-S., Graphene segregated on Ni surfaces and transferred to insulators. *Applied Physics Letters* **2008,** *93* (11), 113103.

48. Weatherup, R. S.; Dlubak, B.; Hofmann, S., Kinetic control of catalytic CVD for high-quality graphene at low temperatures. *ACS nano* **2012,** *6* (11), 9996-10003.

49. Addou, R.; Dahal, A.; Sutter, P.; Batzill, M., Monolayer graphene growth on Ni (111) by low temperature chemical vapor deposition. *Applied Physics Letters* **2012,** *100* (2), 021601.

50. Thiele, S.; Reina, A.; Healey, P.; Kedzierski, J.; Wyatt, P.; Hsu, P.-L.; Keast, C.; Schaefer, J.; Kong, J., Engineering polycrystalline Ni films to improve thickness uniformity of the chemical-vapor-deposition-grown graphene films. *Nanotechnology* **2009,** *21* (1), 015601.

51. Zhang, Y.; Gomez, L.; Ishikawa, F. N.; Madaria, A.; Ryu, K.; Wang, C.; Badmaev, A.; Zhou, C., Comparison of graphene growth on single-crystalline and polycrystalline Ni by chemical vapor deposition. *The Journal of Physical Chemistry Letters* **2010,** *1* (20), 3101-3107.

52. Wang, H.; Wang, G.; Bao, P.; Yang, S.; Zhu, W.; Xie, X.; Zhang, W.-J., Controllable synthesis of submillimeter single-crystal monolayer graphene domains on copper foils by suppressing nucleation. *Journal of the American Chemical Society* **2012,** *134* (8), 3627-3630.

53. Chen, S.; Ji, H.; Chou, H.; Li, Q.; Li, H.; Suk, J. W.; Piner, R.; Liao, L.; Cai, W.; Ruoff, R. S., Millimeter-size single-crystal graphene by suppressing evaporative loss of Cu during low pressure chemical vapor deposition. *Advanced Materials* **2013,** *25* (14), 2062-2065.

54. Wu, X.; Zhong, G.; D'arsié, L.; Sugime, H.; Esconjauregui, S.; Robertson, A. W.; Robertson, J., Growth of continuous monolayer graphene with millimeter-sized domains using industrially safe conditions. *Scientific reports* **2016,** *6*, 21152.

55. Hao, Y.; Bharathi, M.; Wang, L.; Liu, Y.; Chen, H.; Nie, S.; Wang, X.; Chou, H.; Tan, C.; Fallahazad, B., The role of surface oxygen in the growth of large single-crystal graphene on copper. *science* **2013**, 1243879.

56. Ago, H.; Ito, Y.; Mizuta, N.; Yoshida, K.; Hu, B.; Orofeo, C. M.; Tsuji, M.; Ikeda, K.-i.; Mizuno, S., Epitaxial chemical vapor deposition growth of single-layer graphene over cobalt film crystallized on sapphire. *ACS nano* **2010,** *4* (12), 7407-7414.

57. Wang, S.; Pei, Y.; Wang, X.; Wang, H.; Meng, Q.; Tian, H.; Zheng, X.; Zheng, W.; Liu, Y., Synthesis of graphene on a polycrystalline Co film by radio-frequency plasma-enhanced chemical vapour deposition. *Journal of Physics D: Applied Physics* **2010,** *43* (45), 455402.

58. Kim, E.; An, H.; Jang, H.; Cho, W. J.; Lee, N.; Lee, W. G.; Jung, J., Growth of Few-Layer Graphene on a Thin Cobalt Film on a Si/SiO2 Substrate. *Chemical Vapor Deposition* **2011,** *17* (1-3), 9-14.

59. Sutter, P. W.; Flege, J.-I.; Sutter, E. A., Epitaxial graphene on ruthenium. *Nature materials* **2008,** *7* (5), 406.

60. Sutter, P.; Albrecht, P.; Sutter, E. A., Graphene growth on epitaxial Ru thin films on sapphire. *Applied Physics Letters* **2010,** *97* (21), 213101.

61. Sutter, E.; Albrecht, P.; Sutter, P., Graphene growth on polycrystalline Ru thin films. *Applied Physics Letters* **2009,** *95* (13), 133109.

62. Jin, L.; Fu, Q.; Zhang, H.; Mu, R.; Zhang, Y.; Tan, D.; Bao, X., Tailoring the growth of graphene on Ru (0001) via engineering of the substrate surface. *The Journal of Physical Chemistry C* **2012,** *116* (4), 2988-2993.

63. Coraux, J.; N 'Diaye, A. T.; Busse, C.; Michely, T., Structural coherency of graphene on Ir (111). *Nano letters* **2008,** *8* (2), 565-570.

64. Coraux, J.; Engler, M.; Busse, C.; Wall, D.; Buckanie, N.; Zu Heringdorf, F.-J. M.; Van Gastel, R.; Poelsema, B.; Michely, T., Growth of graphene on Ir (111). *New Journal of Physics* **2009,** *11* (2), 023006.

65. Zeller, P.; Dänhardt, S.; Gsell, S.; Schreck, M.; Wintterlin, J., Scalable synthesis of graphene on single crystal Ir (111) films. *Surface Science* **2012,** *606* (19-20), 1475-1480.

66. Hattab, H.; N'Diaye, A.; Wall, D.; Jnawali, G.; Coraux, J.; Busse, C.; van Gastel, R.; Poelsema, B.; Michely, T.; Meyer zu Heringdorf, F.-J., Growth temperature dependent graphene alignment on Ir (111). *Applied Physics Letters* **2011,** *98* (14), 141903.

67. Kang, B. J.; Mun, J. H.; Hwang, C. Y.; Cho, B. J., Monolayer graphene growth on sputtered thin film platinum. *Journal of Applied Physics* **2009,** *106* (10), 104309.

68. Gao, M.; Pan, Y.; Huang, L.; Hu, H.; Zhang, L.; Guo, H.; Du, S.; Gao, H.-J., Epitaxial growth and structural property of graphene on Pt (111). *Applied Physics Letters* **2011,** *98* (3), 033101.

69. Gao, T.; Xie, S.; Gao, Y.; Liu, M.; Chen, Y.; Zhang, Y.; Liu, Z., Growth and atomic-scale characterizations of graphene on multifaceted textured Pt foils prepared by chemical vapor deposition. *ACS nano* **2011,** *5* (11), 9194-9201.

70. Choi, J.-K.; Kwak, J.; Park, S.-D.; Yun, H. D.; Kim, S.-Y.; Jung, M.; Kim, S. Y.; Park, K.; Kang, S.; Kim, S.-D., Growth of wrinkle-free graphene on texture-controlled platinum films and thermal-assisted transfer of large-scale patterned graphene. *ACS nano* **2014,** *9* (1), 679-686.

71. Gao, L.; Ren, W.; Xu, H.; Jin, L.; Wang, Z.; Ma, T.; Ma, L.-P.; Zhang, Z.; Fu, Q.; Peng, L.-M., Repeated growth and bubbling transfer of graphene with millimetre-size single-crystal grains using platinum. *Nature communications* **2012,** *3*, 699.

72. Sun, J.; Nam, Y.; Lindvall, N.; Cole, M. T.; Teo, K. B.; Woo Park, Y.; Yurgens, A., Growth

mechanism of graphene on platinum: Surface catalysis and carbon segregation. *Applied Physics Letters* **2014,** *104* (15), 152107.

73. Yasunishi, T.; Takabayashi, Y.; Kishimoto, S.; Kitaura, R.; Shinohara, H.; Ohno, Y., Origin of residual particles on transferred graphene grown by CVD. *Japanese Journal of Applied Physics* **2016,** *55* (8), 080305.

74. Wang, B.; Huang, M.; Tao, L.; Lee, S. H.; Jang, A.-R.; Li, B.-W.; Shin, H. S.; Akinwande, D.; Ruoff, R. S., Support-free transfer of ultrasmooth graphene films facilitated by self-assembled monolayers for electronic devices and patterns. *ACS nano* **2016,** *10* (1), 1404-1410.

75. Luo, D.; You, X.; Li, B.-W.; Chen, X.; Park, H. J.; Jung, M.; Ko, T. Y.; Wong, K.; Yousaf, M.; Chen, X., Role of graphene in water-assisted oxidation of copper in relation to dry transfer of graphene. *Chemistry of Materials* **2017,** *29* (10), 4546-4556.

76. Wang, Y.; Zheng, Y.; Xu, X.; Dubuisson, E.; Bao, Q.; Lu, J.; Loh, K. P., Electrochemical delamination of CVD-grown graphene film: toward the recyclable use of copper catalyst. *ACS nano* **2011,** *5* (12), 9927-9933.

77. Huang, Y.; Sutter, E.; Shi, N. N.; Zheng, J.; Yang, T.; Englund, D.; Gao, H.-J.; Sutter, P., Reliable exfoliation of large-area high-quality flakes of graphene and other two-dimensional materials. *ACS nano* **2015,** *9* (11), 10612-10620.

78. Jia, C.; Jiang, J.; Gan, L.; Guo, X., Direct optical characterization of graphene growth and domains on growth substrates. *Scientific reports* **2012,** *2*, 707.

79. Kholmanov, I. N.; Magnuson, C. W.; Aliev, A. E.; Li, H.; Zhang, B.; Suk, J. W.; Zhang, L. L.; Peng, E.; Mousavi, S. H.; Khanikaev, A. B., Improved electrical conductivity of graphene films integrated with metal nanowires. *Nano letters* **2012,** *12* (11), 5679-5683.

80. Man, K.; Altman, M., Low energy electron microscopy and photoemission electron microscopy investigation of graphene. *Journal of physics: Condensed matter* **2012,** *24* (31), 314209.

81. Ta, H. Q.; Perello, D. J.; Duong, D. L.; Han, G. H.; Gorantla, S.; Nguyen, V. L.; Bachmatiuk, A.; Rotkin, S. V.; Lee, Y. H.; Rümmeli, M. H., Stranski–Krastanov and Volmer–Weber CVD growth regimes to control the stacking order in bilayer graphene. *Nano letters* **2016,** *16* (10), 6403-6410.

82. Ferrari, A. C.; Basko, D. M., Raman spectroscopy as a versatile tool for studying the properties of graphene. *Nature nanotechnology* **2013,** *8* (4), 235.

83. Liu, Y.; Liu, Z.; Lew, W. S.; Wang, Q. J., Temperature dependence of the electrical transport properties in few-layer graphene interconnects. *Nanoscale research letters* **2013,** *8* (1), 335.

84. Malard, L.; Pimenta, M.; Dresselhaus, G.; Dresselhaus, M., Raman spectroscopy in graphene. *Physics Reports* **2009,** *473* (5-6), 51-87.

85. Emtsev, K.; Speck, F.; Seyller, T.; Ley, L.; Riley, J. D., Interaction, growth, and ordering of epitaxial graphene on SiC {0001} surfaces: A comparative photoelectron spectroscopy study. *Physical Review B* **2008,** *77* (15), 155303.

86. Bae, S.; Kim, H.; Lee, Y.; Xu, X.; Park, J.-S.; Zheng, Y.; Balakrishnan, J.; Lei, T.; Kim, H. R.; Song, Y. I., Roll-to-roll production of 30-inch graphene films for transparent electrodes. *Nature nanotechnology* **2010,** *5* (8), 574.

87. Liu, Y.; Yakobson, B. I., Cones, pringles, and grain boundary landscapes in graphene topology. *Nano letters* **2010,** *10* (6), 2178-2183.

88. Ma, T.; Ren, W.; Liu, Z.; Huang, L.; Ma, L.-P.; Ma, X.; Zhang, Z.; Peng, L.-M.; Cheng, H.-M., Repeated growth–etching–regrowth for large-area defect-free single-crystal graphene by chemical vapor deposition. *ACS nano* **2014,** *8* (12), 12806-12813.

89. Zhou, H.; Yu, W. J.; Liu, L.; Cheng, R.; Chen, Y.; Huang, X.; Liu, Y.; Wang, Y.; Huang, Y.; Duan, X., Chemical vapour deposition growth of large single crystals of monolayer and bilayer graphene. *Nature communications* **2013,** *4*, 2096.

90. Wu, T.; Zhang, X.; Yuan, Q.; Xue, J.; Lu, G.; Liu, Z.; Wang, H.; Wang, H.; Ding, F.; Yu, Q., Fast growth of inch-sized single-crystalline graphene from a controlled single nucleus on Cu–Ni alloys. *Nature materials* **2016,** *15* (1), 43.

91. Lee, J.-H.; Lee, E. K.; Joo, W.-J.; Jang, Y.; Kim, B.-S.; Lim, J. Y.; Choi, S.-H.; Ahn, S. J.; Ahn, J. R.; Park, M.-H., Wafer-scale growth of single-crystal monolayer graphene on reusable hydrogen-terminated germanium. *science* **2014,** *344* (6181), 286-289.

92. Xu, X.; Zhang, Z.; Dong, J.; Yi, D.; Niu, J.; Wu, M.; Lin, L.; Yin, R.; Li, M.; Zhou, J., Ultrafast epitaxial growth of metre-sized single-crystal graphene on industrial Cu foil. *Science Bulletin* **2017,** *62* (15), 1074-1080.

93. Mi, X.; Meunier, V.; Koratkar, N.; Shi, Y., Facet-insensitive graphene growth on copper. *Physical Review B* **2012,** *85* (15), 155436.

94. Nguyen, V. L.; Shin, B. G.; Duong, D. L.; Kim, S. T.; Perello, D.; Lim, Y. J.; Yuan, Q. H.; Ding, F.; Jeong, H. Y.; Shin, H. S., Seamless stitching of graphene domains on polished copper (111) foil. *Advanced Materials* **2015,** *27* (8), 1376-1382.

95. Bluhm, H.; Hävecker, M.; Knop-Gericke, A.; Kleimenov, E.; Schlögl, R.; Teschner, D.; Bukhtiyarov, V. I.; Ogletree, D. F.; Salmeron, M., Methanol oxidation on a copper catalyst investigated using in situ X-ray photoelectron spectroscopy. *The Journal of Physical Chemistry B* **2004,** *108* (38), 14340-14347.

96. Schedel-Niedrig, T.; Hävecker, M.; Knop-Gericke, A.; Schlögl, R., Partial methanol oxidation over copper: active sites observed by means of in situ X-ray absorption spectroscopy. *Physical Chemistry Chemical Physics* **2000,** *2* (15), 3473-3481.

97. Sushkevich, V. L.; Palagin, D.; Ranocchiari, M.; van Bokhoven, J. A., Selective anaerobic oxidation of methane enables direct synthesis of methanol. *science* **2017,** *356* (6337), 523-527.

98. Nicholson, M., The solubility of carbon in nickel-copper alloys at 1000 c. *FIZ TVERD TELA* **1962,** *224* (3), 533-535.

99. Chen, S.; Cai, W.; Piner, R. D.; Suk, J. W.; Wu, Y.; Ren, Y.; Kang, J.; Ruoff, R. S., Synthesis and characterization of large-area graphene and graphite films on commercial Cu–Ni alloy foils. *Nano letters* **2011,** *11* (9), 3519-3525.

100. Wu, Y.; Chou, H.; Ji, H.; Wu, Q.; Chen, S.; Jiang, W.; Hao, Y.; Kang, J.; Ren, Y.; Piner, R. D., Growth mechanism and controlled synthesis of AB-stacked bilayer graphene on Cu–Ni alloy foils. *ACS nano* **2012,** *6* (9), 7731-7738.

101. He, F.; Li, K.; Xie, G.; Wang, Y.; Jiao, M.; Tang, H.; Wu, Z., Theoretical insights on the influence of doped Ni in the early stage of graphene growth during the CH4 dissociation on Ni–Cu (1 1 1) surface. *Applied Catalysis A: General* **2015,** *506*, 1-7.

102. Madito, M.; Bello, A.; Dangbegnon, J. K.; Oliphant, C.; Jordaan, W.; Momodu, D. Y.; Masikhwa, T.; Barzegar, F.; Fabiane, M.; Manyala, N., A dilute Cu (Ni) alloy for synthesis of large-area Bernal stacked bilayer graphene using atmospheric pressure chemical vapour deposition. *Journal of Applied Physics* **2016,** *119* (1), 015306.

103. Bian, X.; Wang, Q.; Wang, X.; Wang, L.; Li, W.-q.; Chen, G.-h.; Zhu, H., Graphene layers on bimetallic Ni/Cu (111) surface and near surface alloys in controlled growth of graphene. *RSC Advances* **2016,** *6* (78), 74973-74981.

104. Tkatchenko, A.; Scheffler, M., Accurate molecular van der Waals interactions from ground-state electron density and free-atom reference data. *Physical review letters* **2009,** *102* (7), 073005.

105. Kresse, G.; Hafner, J., Ab initio molecular dynamics for open-shell transition metals. *Physical Review B* **1993,** *48* (17), 13115.

106. Kresse, G.; Furthmüller, J., Efficiency of ab-initio total energy calculations for metals and semiconductors using a plane-wave basis set. *Computational materials science* **1996,** *6* (1), 15-50.

107. Kresse, G.; Joubert, D., From ultrasoft pseudopotentials to the projector augmented-wave method. *Physical Review B* **1999,** *59* (3), 1758.

108. Perdew, J. P.; Burke, K.; Ernzerhof, M., Generalized gradient approximation made simple. *Physical review letters* **1996,** *77* (18), 3865.

109. Grimme, S., Semiempirical GGA-type density functional constructed with a long-range dispersion correction. *Journal of computational chemistry* **2006,** *27* (15), 1787-1799.

110. Monkhorst, H. J.; Pack, J. D., Special points for Brillouin-zone integrations. *Physical Review B* **1976,** *13* (12), 5188.

111. Henkelman, G.; Uberuaga, B. P.; Jónsson, H., A climbing image nudged elastic band method for finding saddle points and minimum energy paths. *The Journal of chemical physics* **2000,** *113* (22), 9901-9904.

112. Brown, L.; Lochocki, E. B.; Avila, J.; Kim, C.-J.; Ogawa, Y.; Havener, R. W.; Kim, D.-K.; Monkman, E. J.; Shai, D. E.; Wei, H. I., Polycrystalline graphene with single crystalline electronic structure. *Nano letters* **2014,** *14* (10), 5706-5711.

113. Wang, H.; Xu, X.; Li, J.; Lin, L.; Sun, L.; Sun, X.; Zhao, S.; Tan, C.; Chen, C.; Dang, W., Surface Monocrystallization of Copper Foil for Fast Growth of Large Single-Crystal Graphene under Free Molecular Flow. *Advanced Materials* **2016,** *28* (40), 8968-8974.

114. Sakurai, T.; Hashizume, T.; Jimbo, A.; Sakai, A.; Hyodo, S., New result in surface segregation of Ni-Cu binary alloys. *Physical review letters* **1985,** *55* (5), 514.

115. Madito, M.; Manyala, N.; Bello, A.; Dangbegnon, J. K.; Masikhwa, T.; Momodu, D. Y., A wafer-scale Bernal-stacked bilayer graphene film obtained on a dilute Cu (0.61 at% Ni) foil using atmospheric pressure chemical vapour deposition. *RSC Advances* **2016,** *6* (34), 28370-28378.

116. Sakurai, T.; Hashizume, T.; Kobayashi, A.; Sakai, A.; Hyodo, S.; Kuk, Y.; Pickering, H., Surface segregation of Ni-Cu binary alloys studied by an atom-probe. *Physical Review B* **1986,** *34* (12), 8379.

117. Wu, P.; Zhang, W.; Li, Z.; Yang, J.; Hou, J. G., Communication: Coalescence of carbon atoms on Cu (111) surface: Emergence of a stable bridging-metal structure motif. AIP: 2010.

118. Hayashi, K.; Sato, S.; Ikeda, M.; Kaneta, C.; Yokoyama, N., Selective graphene formation on copper twin crystals. *Journal of the American Chemical Society* **2012,** *134* (30), 12492-12498.

119. Mehdipour, H.; Ostrikov, K., Kinetics of low-pressure, low-temperature graphene growth: toward single-layer, single-crystalline structure. *ACS nano* **2012,** *6* (11), 10276-10286.

120. Wu, P.; Jiang, H.; Zhang, W.; Li, Z.; Hou, Z.; Yang, J., Lattice mismatch induced nonlinear growth of graphene. *Journal of the American Chemical Society* **2012,** *134* (13), 6045-6051.

121. Yuan, Q.; Ding, F., Formation of carbyne and graphyne on transition metal surfaces. *Nanoscale* **2014,** *6* (21), 12727-12731.

122. Shu, H.; Tao, X.-M.; Ding, F., What are the active carbon species during graphene chemical vapor deposition growth? *Nanoscale* **2015,** *7* (5), 1627-1634.

123. Xing, S.; Wu, W.; Wang, Y.; Bao, J.; Pei, S.-S., Kinetic study of graphene growth: Temperature perspective on growth rate and film thickness by chemical vapor deposition. *Chemical Physics Letters* **2013,** *580*, 62-66.

124. Hsieh, Y.-P.; Hofmann, M.; Kong, J., Promoter-assisted chemical vapor deposition of graphene. *carbon* **2014,** *67*, 417-423.

125. Celebi, K.; Cole, M. T.; Choi, J. W.; Wyczisk, F.; Legagneux, P.; Rupesinghe, N.; Robertson, J.; Teo, K. B.; Park, H. G., Evolutionary kinetics of graphene formation on copper. *Nano letters* **2013,** *13* (3), 967-974.

126. Vlassiouk, I.; Smirnov, S.; Regmi, M.; Surwade, S. P.; Srivastava, N.; Feenstra, R.; Eres, G.; Parish, C.; Lavrik, N.; Datskos, P., Graphene nucleation density on copper: fundamental role of background pressure. *The Journal of Physical Chemistry C* **2013,** *117* (37), 18919-18926.

127. Ago, H.; Ohta, Y.; Hibino, H.; Yoshimura, D.; Takizawa, R.; Uchida, Y.; Tsuji, M.; Okajima, T.; Mitani, H.; Mizuno, S., Growth dynamics of single-layer graphene on epitaxial Cu surfaces.

Chemistry of Materials **2015,** *27* (15), 5377-5385.

128. Wang, S.; Hibino, H.; Suzuki, S.; Yamamoto, H., Atmospheric pressure chemical vapor deposition growth of millimeter-scale single-crystalline graphene on the copper surface with a native oxide layer. *Chemistry of Materials* **2016,** *28* (14), 4893-4900.

129. Li, X.; Magnuson, C. W.; Venugopal, A.; An, J.; Suk, J. W.; Han, B.; Borysiak, M.; Cai, W.; Velamakanni, A.; Zhu, Y., Graphene films with large domain size by a two-step chemical vapor deposition process. *Nano letters* **2010,** *10* (11), 4328-4334.

130. Li, X.; Magnuson, C. W.; Venugopal, A.; Tromp, R. M.; Hannon, J. B.; Vogel, E. M.; Colombo, L.; Ruoff, R. S., Large-area graphene single crystals grown by low-pressure chemical vapor deposition of methane on copper. *Journal of the American Chemical Society* **2011,** *133* (9), 2816-2819.

131. Vlassiouk, I.; Regmi, M.; Fulvio, P.; Dai, S.; Datskos, P.; Eres, G.; Smirnov, S., Role of hydrogen in chemical vapor deposition growth of large single-crystal graphene. *ACS nano* **2011,** *5* (7), 6069-6076.

132. Chae, D.-H.; Krauss, B.; Von Klitzing, K.; Smet, J. H., Hot phonons in an electrically biased graphene constriction. *Nano letters* **2009,** *10* (2), 466-471.

133. Mohsin, A.; Liu, L.; Liu, P.; Deng, W.; Ivanov, I. N.; Li, G.; Dyck, O. E.; Duscher, G.; Dunlap, J. R.; Xiao, K., Synthesis of millimeter-size hexagon-shaped graphene single crystals on resolidified copper. *ACS nano* **2013,** *7* (10), 8924-8931.

134. Yu, Q.; Jauregui, L. A.; Wu, W.; Colby, R.; Tian, J.; Su, Z.; Cao, H.; Liu, Z.; Pandey, D.; Wei, D., Control and characterization of individual grains and grain boundaries in graphene grown by chemical vapour deposition. *Nature materials* **2011,** *10* (6), 443.

135. Zhang, Y.; Li, Z.; Kim, P.; Zhang, L.; Zhou, C., Anisotropic hydrogen etching of chemical vapor deposited graphene. *ACS nano* **2011,** *6* (1), 126-132.

136. Guo, W.; Wu, B.; Li, Y.; Wang, L.; Chen, J.; Chen, B.; Zhang, Z.; Peng, L.; Wang, S.; Liu, Y., Governing rule for dynamic formation of grain boundaries in grown graphene. *ACS nano* **2015,** *9* (6), 5792-5798.

137. Yang, W.; Chen, G.; Shi, Z.; Liu, C.-C.; Zhang, L.; Xie, G.; Cheng, M.; Wang, D.; Yang, R.; Shi, D., Epitaxial growth of single-domain graphene on hexagonal boron nitride. *Nature materials* **2013,** *12* (9), 792.

138. Yang, R.; Zhang, L.; Wang, Y.; Shi, Z.; Shi, D.; Gao, H.; Wang, E.; Zhang, G., An anisotropic etching effect in the graphene basal plane. *Advanced Materials* **2010,** *22* (36), 4014-4019.

139. Kim, D. W.; Kim, Y. H.; Jeong, H. S.; Jung, H.-T., Direct visualization of large-area graphene domains and boundaries by optical birefringency. *Nature nanotechnology* **2012,** *7* (1), 29.

140. Li, X.; Zhu, Y.; Cai, W.; Borysiak, M.; Han, B.; Chen, D.; Piner, R. D.; Colombo, L.; Ruoff, R. S., Transfer of large-area graphene films for high-performance transparent conductive electrodes. *Nano letters* **2009,** *9* (12), 4359-4363.

141. Gomez De Arco, L.; Zhang, Y.; Schlenker, C. W.; Ryu, K.; Thompson, M. E.; Zhou, C., Continuous, highly flexible, and transparent graphene films by chemical vapor deposition for organic photovoltaics. *ACS nano* **2010,** *4* (5), 2865-2873.

142. Lee, Y.; Bae, S.; Jang, H.; Jang, S.; Zhu, S.-E.; Sim, S. H.; Song, Y. I.; Hong, B. H.; Ahn, J.-H., Wafer-scale synthesis and transfer of graphene films. *Nano letters* **2010,** *10* (2), 490-493.

143. Zhang, Y.; Gao, T.; Gao, Y.; Xie, S.; Ji, Q.; Yan, K.; Peng, H.; Liu, Z., Defect-like structures of graphene on copper foils for strain relief investigated by high-resolution scanning tunneling microscopy. *ACS nano* **2011,** *5* (5), 4014-4022.

144. Kang, J. H.; Moon, J.; Kim, D. J.; Kim, Y.; Jo, I.; Jeon, C.; Lee, J.; Hong, B. H., Strain Relaxation of Graphene Layers by Cu Surface Roughening. *Nano letters* **2016,** *16* (10), 5993-5998.

145. Meyer, J. C.; Geim, A. K.; Katsnelson, M. I.; Novoselov, K. S.; Booth, T. J.; Roth, S., The structure of suspended graphene sheets. *nature* **2007,** *446* (7131), 60.

146. Brown, L.; Hovden, R.; Huang, P.; Wojcik, M.; Muller, D. A.; Park, J., Twinning and twisting of tri-and bilayer graphene. *Nano letters* **2012,** *12* (3), 1609-1615.

147. Lin, J.; Fang, W.; Zhou, W.; Lupini, A. R.; Idrobo, J. C.; Kong, J.; Pennycook, S. J.; Pantelides, S. T., AC/AB stacking boundaries in bilayer graphene. *Nano letters* **2013,** *13* (7), 3262-3268.

148. Robertson, A. W.; Bachmatiuk, A.; Wu, Y. A.; Schäffel, F.; Rellinghaus, B.; Büchner, B.; Rümmeli, M. H.; Warner, J. H., Atomic structure of interconnected few-layer graphene domains. *ACS nano* **2011,** *5* (8), 6610-6618.

149. Tsen, A. W.; Brown, L.; Levendorf, M. P.; Ghahari, F.; Huang, P. Y.; Havener, R. W.; Ruiz-Vargas, C. S.; Muller, D. A.; Kim, P.; Park, J., Tailoring electrical transport across grain boundaries in polycrystalline graphene. *science* **2012,** *336* (6085), 1143-1146.

150. Alden, J. S.; Tsen, A. W.; Huang, P. Y.; Hovden, R.; Brown, L.; Park, J.; Muller, D. A.; McEuen, P. L., Strain solitons and topological defects in bilayer graphene. *Proceedings of the National Academy of Sciences* **2013,** *110* (28), 11256-11260.

151. Butz, B.; Dolle, C.; Niekiel, F.; Weber, K.; Waldmann, D.; Weber, H. B.; Meyer, B.; Spiecker, E., Dislocations in bilayer graphene. *nature* **2014,** *505* (7484), 533.

152. Kim, K.; Lee, Z.; Malone, B. D.; Chan, K. T.; Alemán, B.; Regan, W.; Gannett, W.; Crommie, M.; Cohen, M. L.; Zettl, A., Multiply folded graphene. *Physical Review B* **2011,** *83* (24), 245433.

153. Clark, K. W.; Zhang, X.-G.; Vlassiouk, I. V.; He, G.; Feenstra, R. M.; Li, A.-P., Spatially resolved mapping of electrical conductivity across individual domain (grain) boundaries in graphene. *ACS nano* **2013,** *7* (9), 7956-7966.

154. Girit, Ç. Ö.; Meyer, J. C.; Erni, R.; Rossell, M. D.; Kisielowski, C.; Yang, L.; Park, C.-H.; Crommie, M.; Cohen, M. L.; Louie, S. G., Graphene at the edge: stability and dynamics. *science* **2009,** *323* (5922), 1705-1708.

155. Ramasse, Q. M.; Zan, R.; Bangert, U.; Boukhvalov, D. W.; Son, Y.-W.; Novoselov, K. S., Direct experimental evidence of metal-mediated etching of suspended graphene. *ACS nano* **2012,** *6* (5), 4063-4071.

156. Haigh, S.; Gholinia, A.; Jalil, R.; Romani, S.; Britnell, L.; Elias, D.; Novoselov, K.; Ponomarenko, L.; Geim, A.; Gorbachev, R., Cross-sectional imaging of individual layers and buried interfaces of graphene-based heterostructures and superlattices. *Nature materials* **2012,** *11* (9), 764.

157. Yuk, J. M.; Jeong, H. Y.; Kim, N. Y.; Park, H. J.; Kim, G.; Shin, H. S.; Ruoff, R. S.; Lee, J. Y.; Lee, Z., Superstructural defects and superlattice domains in stacked graphene. *carbon* **2014,** *80*, 755-761.

158. Hibino, H.; Kageshima, H.; Kotsugi, M.; Maeda, F.; Guo, F.-Z.; Watanabe, Y., Dependence of electronic properties of epitaxial few-layer graphene on the number of layers investigated by photoelectron emission microscopy. *Physical Review B* **2009,** *79* (12), 125437.

159. Malard, L.; Guimaraes, M.; Mafra, D.; Jorio, A., Group-theory analysis of electrons and phonons in N-layer graphene systems. *Physical Review B* **2009,** *79* (12), 125426.

160. Geim, A. K.; Novoselov, K. S., The rise of graphene. *Nature materials* **2007,** *6* (3), 183.

161. Zhang, Y.; Tang, T.-T.; Girit, C.; Hao, Z.; Martin, M. C.; Zettl, A.; Crommie, M. F.; Shen, Y. R.; Wang, F., Direct observation of a widely tunable bandgap in bilayer graphene. *nature* **2009,** *459* (7248), 820.

162. Mak, K. F.; Lui, C. H.; Shan, J.; Heinz, T. F., Observation of an electric-field-induced band gap in bilayer graphene by infrared spectroscopy. *Physical review letters* **2009,** *102* (25), 256405.

163. Mak, K. F.; Shan, J.; Heinz, T. F., Electronic structure of few-layer graphene: experimental demonstration of strong dependence on stacking sequence. *Physical review letters* **2010,** *104* (17), 176404.

164. Aoki, M.; Amawashi, H., Dependence of band structures on stacking and field in layered graphene. *Solid State Communications* **2007,** *142* (3), 123-127.

165. Koshino, M.; McCann, E., Gate-induced interlayer asymmetry in ABA-stacked trilayer graphene. *Physical Review B* **2009,** *79* (12), 125443.

166. Zhang, F.; Sahu, B.; Min, H.; MacDonald, A. H., Band structure of A B C-stacked graphene trilayers. *Physical Review B* **2010,** *82* (3), 035409.

167. Oostinga, J. B.; Heersche, H. B.; Liu, X.; Morpurgo, A. F.; Vandersypen, L. M., Gate-induced insulating state in bilayer graphene devices. *Nature materials* **2008,** *7* (2), 151.

168. Yan, K.; Peng, H.; Zhou, Y.; Li, H.; Liu, Z., Formation of bilayer bernal graphene: layer-by-layer epitaxy via chemical vapor deposition. *Nano letters* **2011,** *11* (3), 1106-1110.

169. Liu, L.; Zhou, H.; Cheng, R.; Yu, W. J.; Liu, Y.; Chen, Y.; Shaw, J.; Zhong, X.; Huang, Y.; Duan, X., High-yield chemical vapor deposition growth of high-quality large-area AB-stacked bilayer graphene. *ACS nano* **2012,** *6* (9), 8241-8249.

170. Sun, H.-B.; Wu, J.; Han, Y.; Wang, J.-Y.; Song, F.-Q.; Wan, J.-G., Nonisothermal synthesis of AB-stacked bilayer graphene on Cu foils by atmospheric pressure chemical vapor deposition. *The Journal of Physical Chemistry C* **2014,** *118* (26), 14655-14661.

171. Zhao, P.; Kim, S.; Chen, X.; Einarsson, E.; Wang, M.; Song, Y.; Wang, H.; Chiashi, S.; Xiang, R.; Maruyama, S., Equilibrium chemical vapor deposition growth of Bernal-stacked bilayer graphene. *ACS nano* **2014,** *8* (11), 11631-11638.

172. López, G.; Mittemeijer, E., The solubility of C in solid Cu. *Scripta Materialia* **2004,** *51* (1), 1-5.

173. Liu, X.; Fu, L.; Liu, N.; Gao, T.; Zhang, Y.; Liao, L.; Liu, Z., Segregation growth of graphene on Cu–Ni alloy for precise layer control. *The Journal of Physical Chemistry C* **2011,** *115* (24), 11976-11982.

174. Choi, H.; Lim, Y.; Park, M.; Lee, S.; Kang, Y.; Kim, M. S.; Kim, J.; Jeon, M., Precise control of chemical vapor deposition graphene layer thickness using Ni x Cu 1− x alloys. *Journal of Materials Chemistry C* **2015,** *3* (7), 1463-1467.

175. Kim, E.; Kim, Y. S.; Park, J.; Hussain, S.; Chun, S.-H.; Kim, S. J.; An, K.-S.; Lee, W.-J.; Lee, W.-G.; Jung, J., Graphene film growth on sputtered thin Cu–Ni alloy film by inductively coupled plasma chemical vapor deposition. *RSC Advances* **2014,** *4* (108), 63349-63353.

176. Takesaki, Y.; Kawahara, K.; Hibino, H.; Okada, S.; Tsuji, M.; Ago, H., Highly uniform bilayer graphene on epitaxial Cu–Ni (111) alloy. *Chemistry of Materials* **2016,** *28* (13), 4583-4592.

177. Giannuzzi, L. A.; Stevie, F. A., A review of focused ion beam milling techniques for TEM specimen preparation. *Micron* **1999,** *30* (3), 197-204.

178. Wang, Z.-J.; Dong, J.; Cui, Y.; Eres, G.; Timpe, O.; Fu, Q.; Ding, F.; Schlögl, R.; Willinger, M.-G., Stacking sequence and interlayer coupling in few-layer graphene revealed by in situ imaging. *Nature communications* **2016,** *7*, 13256.

179. Lee, S.; Lee, K.; Zhong, Z., Wafer scale homogeneous bilayer graphene films by chemical vapor deposition. *Nano letters* **2010,** *10* (11), 4702-4707.

180. Gupta, A.; Chen, G.; Joshi, P.; Tadigadapa, S.; Eklund, P., Raman scattering from high-frequency phonons in supported n-graphene layer films. *Nano letters* **2006,** *6* (12), 2667-2673.

181. Graf, D.; Molitor, F.; Ensslin, K.; Stampfer, C.; Jungen, A.; Hierold, C.; Wirtz, L., Spatially resolved Raman spectroscopy of single-and few-layer graphene. *Nano letters* **2007,** *7* (2), 238-242.

182. Sun, Z.; Raji, A.-R. O.; Zhu, Y.; Xiang, C.; Yan, Z.; Kittrell, C.; Samuel, E.; Tour, J. M., Large-area Bernal-stacked bi-, tri-, and tetralayer graphene. *ACS nano* **2012,** *6* (11), 9790-9796.

183. Zhao, Z.; Shan, Z.; Zhang, C.; Li, Q.; Tian, B.; Huang, Z.; Lin, W.; Chen, X.; Ji, H.; Zhang, W., Study on the diffusion mechanism of graphene grown on copper pockets. *Small* **2015,** *11* (12), 1418-1422.

184. Li, Q.; Chou, H.; Zhong, J.-H.; Liu, J.-Y.; Dolocan, A.; Zhang, J.; Zhou, Y.; Ruoff, R. S.;

Chen, S.; Cai, W., Growth of adlayer graphene on Cu studied by carbon isotope labeling. *Nano letters* **2013,** *13* (2), 486-490.

185. Wang, Z.-J.; Weinberg, G.; Zhang, Q.; Lunkenbein, T.; Klein-Hoffmann, A.; Kurnatowska, M.; Plodinec, M.; Li, Q.; Chi, L.; Schloegl, R., Direct observation of graphene growth and associated copper substrate dynamics by in situ scanning electron microscopy. *ACS nano* **2015,** *9* (2), 1506-1519.

186. Weatherup, R. S.; Shahani, A. J.; Wang, Z.-J.; Mingard, K.; Pollard, A. J.; Willinger, M.-G.; Schloegl, R.; Voorhees, P. W.; Hofmann, S., In situ graphene growth dynamics on polycrystalline catalyst foils. *Nano letters* **2016,** *16* (10), 6196-6206.

187. McLean, J. G.; Krishnamachari, B.; Peale, D.; Chason, E.; Sethna, J. P.; Cooper, B., Decay of isolated surface features driven by the Gibbs-Thomson effect in an analytic model and a simulation. *Physical Review B* **1997,** *55* (3), 1811.

188. Wang, G.; Zhang, M.; Liu, S.; Xie, X.; Ding, G.; Wang, Y.; Chu, P. K.; Gao, H.; Ren, W.; Yuan, Q., Synthesis of Layer-Tunable Graphene: A Combined Kinetic Implantation and Thermal Ejection Approach. *Advanced Functional Materials* **2015,** *25* (24), 3666-3675.

189. Liu, W.; Kraemer, S.; Sarkar, D.; Li, H.; Ajayan, P. M.; Banerjee, K., Controllable and rapid synthesis of high-quality and large-area Bernal stacked bilayer graphene using chemical vapor deposition. *Chemistry of Materials* **2013,** *26* (2), 907-915.

190. Zou, K.; Zhu, J., Transport in gapped bilayer graphene: The role of potential fluctuations. *Physical Review B* **2010,** *82* (8), 081407.

Acknowledgements

The completion of this thesis is attributed to all those who have helped and supported me during my PhD study in UNIST.

First and foremost, I would like to express my deepest gratitude to my supervisor, Prof. Rodney S. Ruoff, for giving me the chance and honor to work in his group and providing me an excellent atmosphere for doing research. Prof. Ruoff has devoted a considerable portion of his time to teach me how to explore the basic science in my research and offer me invaluable guidance on my pursuit of career and future goals. I'm very grateful for his excellent guidance, tremendous support and patience during all these years. I am also greatly indebted to UNIST for providing me "Nine Bridge & Star Fellowship" and also the finical support from our center, IBS CMCM.

Many thanks should go to Prof. Jong-Beom Baek, Prof. Zonghoon Lee, Prof. Hyung-Joon Shin, and Prof. Sang Ouk Kim for being my thesis defense committee members. I would also like to thank my Ph.D. qualifying exam committee member, Prof. Sukbin Lee, for his valuable time and suggestions. In addition, I would like to thank Prof. Zonghoon Lee for assistance with TEM experiment, Prof. Won Jong Yoo for GFET measurement, Prof. Yeliang Wang for STM characterization, Prof. Marc-Georg Willinger for *in-situ* SEM experiments, Prof. Feng Ding for theoretical calculation and Prof. Peter Thrower for manuscript revision and modification. Special thanks also go to Dr. Lili Zhang for her advice, encouragement and help when I feel upset or meet problems.

I thank Dr. Mandakini Biswal, a post-doc in our group that I got to work very closely with and learn much from. Mandakini helped me when I first arrived at UNIST and joined our center to become familiar with laboratory research and later we worked together on several projects. I also would like to thank all the group members and colleagues I have met and worked with, Dr. Sun Hwa Lee, Dr. Xu Zhang, Dr. Bin Wang, Dr. Sunghwan Jin, Dr. Da Luo, Dr. Xianjue (Sam) Chen, Dr. Yuan Huang, Dr. Wei Li, Dr. Pavel Bakharev, Dr. Manav Saxena, Dr. Won Kyung Seong, Dr. Yong Jin Kim, Dr. Chunhui Wang, Dr. Yi Jiang, Dr. Xiong Chen, Dr. Vijayakumar Modepalli, Dr. Baowen Li, Dr. Hanyang Zhang, Dr. Xiaozhong Wu, Youngwoo Kwon, Meihui Wang, Xuewei Zhang, Min Goo, Hyo Ju Park, Seokmo Hong, Lu Qiu, Deshun Qu, Xiaochi Liu, Zheng Yang, Zhili Zhu and Zhongliu Liu for their help and support during my Ph.D study.

Last but not least, I would like to express my sincere appreciation to my wife and my parents. Their inspiration and support motivate me to move on and make me want to be a better person.